MULTIDIMENSIONAL MODELING OF IGNITION AND COMBUSTION IN SPARK-IGNITON ENGINES BASED ON LEVEL-SET APPROACH

by

Guangfei Zhu

A Dissertation Submitted in Partial Fulfillment of
the Requirement for the Degree of

Doctor of Philosophy

(Mechanical Engineering)

at the
UNIVERSITY OF WISCONSIN-MADISON
2018

Data of final oral examination: 12/04/2018

The dissertation is approved by the following members of the Final Oral Committee:
Christopher J. Rutland, Professor, Mechanical Engineering
Jaal B. Ghandhi, Professor, Mechanical Engineering
Sage L. Kokjohn, Assistant Professor, Mechanical Engineering
David A. Rothamer, Associate Professor, Mechanical Engineering
Samuel N. Stechmann, Professor, Mathematics

MULTIDIMENSIONAL MODELING OF IGNITION AND COMBUSTION IN SPARK-IGNITON ENGINES BASED ON LEVEL-SET APPROACH

Guangfei Zhu

Under the Supervision of Professor Christopher J. Rutland

At the University of Wisconsin-Madison

An LES version ignition model, WSSIM, was developed by taking the effect of turbulence on wrinkling and stretching the flame surface into account. Next, this ignition model was combined with an innovative swept-volume algorithm based combustion model to simulate the cycle to cycle variations of ignition and combustion processes in premixed propane/air mixtures. The open source software OpenFOAM-5.0 helped to implement and validate the models.

First, in current study, the G Equation was used to track the flame surface during the combustion process where the flame front is set at $G = 0$. To understand the role of each term in G-Equation plays, three computational experiments were implemented. Following this, to calculate the species reaction rate and heat release rate more accurately, a new innovative swept-volume approach, as based on precise sub-volume calculations, was implemented. The basic idea behind the swept-volume algorithm is to find the intersection points between flame fronts and mesh cell edges to determine the burnt sub-volume, triangulated the burnt sub-volume, and finally to apply the Gaussian divergence theorem [1], with the aim of calculating the burnt sub-volume. The formation of thermodynamic equilibrium species mass fraction is calculated using the element potential method [2] by determining equilibrium, which is based on the minimization of Gibbs free energy.

Second, the reinitialization scheme was used for the reconstruction of the signed distance function in the context of G-Equation. In this research, the method put forward in [3] was improved

by extending to non-uniform and non-orthogonal for engine hexahedral mesh cases, and further extended to parallel computing by accurately determining the neighbor cells for a certain mesh cell. To make the reinitialization to be more universal to all mesh types, this research presented an efficient direct reinitialization. The reinitialization scheme developed in this work achieved validation by both serial computation and parallel computation.

Third, the ignition model, WSSIM, was developed by strategically using the effect of turbulence on wrinkling and stretching the resulting kernel surface into account. There are four sub-models in WSSIM, those being the electric circuit model, the plasma channel model, the kernel growth model, and the restrike model. The ignition model was applied to a constant volume charged with mixture of propane and air, and the predicted kernel size from simulations were compared with available experimental data [113].

Finally, the combination of ignition model and the swept-volume based combustion model was applied to the TCC3 engine with the goal of investigating the CCV phenomena. By investigating the relationship between mesh resolution and flame surface capture, the conclusion is that the mesh size should be less than the inverse curvature of the initial kernel size in order to capture the kernel front while time progresses. To investigate the CCV phenomena in engines, the TCC3 engine was chosen and 30 simulation cycles were implemented. The pressure traces, the current, and the voltage from simulations are compared with measured experimental data. Sensitivity tests were implemented by choosing three representative cases: high, medium, low according to their CA10 values. It was found that changing the velocity fields U had the most significant effect on combustion. In addition, the effect of transition radius was also investigated.

Acknowledgements

I would like to express my thanks and highest respect to my advisor, Professor Christopher J. Rutland, for his guidance and consulting during my research. He is wonderfully patient and has an erudite knowledge. From his encouragement and instruction, I now understand what the proper attitude is have as a researcher and how to grasp the key points of research. Moreover, I express my special appreciation for his support to help me pursue my dream of artificial intelligence in the tides of time. He is genuinely nice, caring, and considerate, and it is my great honor to meet and work with my advisor in my youthful days.

In addition, I must share my gratitude toward my parents, my sister, and brother-in-law for their love, concern, and understanding. They always respect my decisions and continue to give their financial support and moral encouragement to me. They forever try their best to provide me with the greatest things they can offer and never ask for anything in return. My family taught me the value and power of family affection and bonds.

Third, General Motors deserves great acknowledgement for the funding they contributed to this project. I would especially like to thank Tang-wei Kuo, Ronald Grover, Seunghwan Keum, and Xiaofeng Yang for their suggestions, support, and interest in the research.

Fourth, a special thanks to all difficulties and troubles that I encountered. They promoted me to be more optimistic, persistent, mature, confident, and stronger. They told me that the number of approaches are always more than that of difficulties, even while the number of excuses are always more than that of approaches.

Finally, I would like to take this opportunity to thank all my close friends. Their entrance in my life brought me a lot of beautiful memories that I will cherish until my final days. In addition, some of them have become the saviors in my destiny.

Table of Contents

Acknowledgements iii

Table of Contents iv

List of Figures ix

List of Tables xvii

Chapter 1 Introduction 1

1.1 Background and Motivation 1

1.2 Objective and Approach 4

1.3 Outline of the Thesis 5

Chapter 2 Literature Review 7

2.1 Ignition Models 7

2.1.1 Ignition Mechanisms 7

2.1.1.1 Breakdown Phase 7

2.1.1.2 Arc Phase 9

2.1.1.3 Glow Phase 11

2.1.2 Ignition Modeling 12

2.1.2.1 Energy Deposition Model 12

2.1.2.2 DPIK (Discrete Particle Ignition Kernel) Model 12

2.1.2.3 AKTIM (Arc and Kernel Tracking Ignition) Model 14

2.1.2.4 Spark-CIMM (Channel Ignition Monitoring Model) 16

2.2 Turbulent Premixed Combustion 17

2.2.1 Laminar Premixed Flame Structure 17

2.2.2 Premixed Turbulent Combustion Regimes 18

2.3 Turbulent Premixed Combustion Models 21

2.3.1 Turbulence Controlled Models 22

2.3.1.1 Eddy-Break-Up Model 22

2.3.1.2 Eddy-Dissipation-Model 23

2.3.1.3 Characteristic-Time Model 24

2.3.2 Flamelet Models 25

2.3.2.1 Bray-Moss-Libby Model 25

2.3.2.2 Coherent Flamelet Model 26

2.3.2.3 G-Equation Models 27

Chapter 3 Model Development and Implementation in OpenFOAM 29

3.1 G-Equation Implementation 29

3.1.1 G-Equation Description of Turbulent Flame Propagation 29

3.1.2 G-Equation for the Corrugated and Thin Reaction Flamelet Regimes 32

3.1.3 G-Equation for Both Regimes 33

3.1.4 RANS and LES Versions of G-Equation 34

3.1.2 G-Equation Tests 35

3.1.2.1 Circle Growth 35

3.1.2.2 Circle Moving 36

3.1.2.3 Circle disappearing 38

3.1.3 Laminar and Turbulent Flame Speed Correlations 39

3.1.4 Combustion Model 42

3.1.4.1 PDF (Probability Density Function) 43

3.1.4.2 Xiaofeng Model 44

3.1.4.3 Zhichao Model 45

3.1.4.4 Swept-volume Combustion Algorithm 46

3.1.5 Reinitialization Scheme 51

3.1.5.1 Reinitialization Scheme Implementation 52

3.1.5.2 Reinitialization Extension to Non-Hexahedra Mesh 56

3.2 Ignition Model Development 58

3.2.1 Electric Circuit Sub-Model 59

3.2.2 Kernel Growth Sub-Model 61

3.2.2.1 Kernel Growth Sub-Model: Phase (a) 63

3.2.2.2 Kernel Growth Sub-Model: Phase (b) 64

3.2.3 Plasma Channel Sub-Model 65

3.2.4 Restrike Sub-Model 67

3.2.5 Summary 68

Chapter 4 Model Validation 70

4.1 Swept-Volume Method Validation 70

4.1.1 3D Ellipsoid and Two Intersected Spheres 70

4.1.2 Constant Volume Vessel Validation 72

4.2 Reinitialization Validation 77

4.2.1 Reinitialization Validation for Hexahedral Mesh 77

4.2.2 Reinitialization Validation for Non-Hexahedral Mesh 81

4.3 Ignition Validation 85

4.4 RANS Validation for TCC3 Engine 93

Chapter 5 Engine Combustion Variability 102

5.1 Effect of Mesh Resolution on Flame Surface Capture 102

5.2 Stoichiometric Combustion 104

5.2.1 Combustion of Multiple Simulation Cycles 104

5.2.2 Sensitivity Tests 111

5.2.3 Effect of Transition Radius 123

5.2.4 Effect of Spark Kernel Convection 126

5.2.5 Effect of Fuel on Combustion 128

5.3 Lean Combustion 129

Chapter 6 Summary, Conclusion and Future Work 134

6.1 Summary and Conclusions 134

6.2 Recommendations for Future Work 138

Appendix A Chemical Equilibrium Solver Test 139

Appendix B Intersections between flame front and cell edges [1] 140

Appendix C Mapping Methods 142

References 145

List of Figures

Figure 2-1 DPIK model [46] 13

Figure 2-2 Schematic illustration of flame structure of premixed methane-air [51] 18

Figure 2-3 Regime diagram for premixed turbulent combustion [53] 19

Figure 2-4 Interaction between eddy with size lm and turbulent flame front [53] 21

Figure 3-1 G value definition for premixed turbulent flames [82] 30

Figure 3-2 *G* value determination in combustion domain 32

Figure 3-3 Growth of the calculated sphere (black circle represents $G = 0$) using Eqn. (3-23) ... 36

Figure 3-4 Moving of the calculated sphere (black circle represents $G = 0$) using Eqn. (3-24) ... 37

Figure 3-5 Moving of the calculated sphere (black circle represents $G = 0$) using Eqn. (3-25) ... 38

Figure 3-6 Comparison between experiments [88][89][90] and laminar burning velocity correlations (Propane, p = 1atm, T = 300 K) 40

Figure 3-7 Relationship between sT correlation and its related parameters 41

Figure 3-8 Probability density of finding the instantaneous flame front [25] 43

Figure 3-9 Schematic diagram showing the mean flame front [46] 45

Figure 3-10 Illustration of the inaccuracy of $sT\Delta tAF$ for the approximation of true volume swept by the flame 46

Figure 3-11 Basic cases for sub-volume calculation [95] 48

Figure 3-12 Sub-volume (volume enclosed by the red frame) calculation by reconstructing isosurface from nodal fields in mesh cells (v represents the vertex and e represents the edge) ... 49

Figure 3-13 isovalue lines at two different time ($u1 > u2$) 52

Figure 3-14 Signal propagation off the zero level set. The solid arrows represent the unit normal to the zero level set while the dashed arrows stands for the direction of the propagation of the signal [3]. 54

Figure 3-15 vertex ordering in OpenFOAM mesh 55

Figure 3-16 Illustration of the efficient direct reinitialization 56

Figure 3-17 Projection of random point xn to two triangular surfaces (bold lines) with line2 and line2 being the projection distance from xn to the triangular surfaces..... 57

Figure 3-18 Flow chart of WSSIM (Wrinkling and Stretch Spark Ignition Model) including the electric circuit model, the plasma channel model, the kernel growth model, and the restrike model 58

Figure 3-19 Schematic of primary and secondary circuits [24]..... 59

Figure 3-20 Spark length calculation in the electric circuit model. In (a), the spark length is represented by a set of Lagrangian particles. In (b), only one flame kernel is initialized, an equivalent spark length is calculated as the sum of L1 and L2 61

Figure 3-21 Flame speed sflame evolution during the ignition process (the WSSIM includes Phase (a) and Phase (b)) 62

Figure 3-22 Relationship between transition function value and rk (Δ is set to be 2.0) 65

Figure 4-1 Sub-volume algorithm verification for a 3D ellipsoid with a 30 degree between the axis *a* and the horizontal line (*a* = 40 mm, *b* = 30 mm and *c* = 20 mm in x, y and z directions where the axis c points inside the picture.)..... 71

Figure 4-2 Sub-volume algorithm verification for two-intersected spheres (*a* = 13 mm, *h* = 5 mm and *R* = 20 mm in the test case) 72

Figure 4-3 2D simulation domain for model validation 74

Figure 4-4 Flame radius comparison between simulation and experiments (phi = 0.9, u' = 2 m/s) 75

Figure 4-5 Comparison of laminar burning velocity correlations for methane ((a) phi = 1.0, p= 1 atm; (b) phi = 1.0, Tu = 300 K) 76

Figure 4-6 turbulent burning velocity Eqn. (4-1) comparison between simulation and experiments (phi = 1.0) 77

Figure 4-7 *G* value initialization for TCC3 engine mesh 78

Figure 4-8 *G* value on two extracted lines after reinitialization 78

Figure 4-9 *G* value on two extracted lines after reinitialization (parallel computation)..... 79

Figure 4-10 Reinitialization test [3]..... 80

Figure 4-11 Efficient direct reinitialization test on hexahedral mesh..... 81

Figure 4-12 Initial *G* value setting for hexahedral mesh: left picture (a); *G* value after efficient direct reinitialization scheme: right picture (b) (black solid line is the *G* value based on 1 CPU while the dot plot is the *G* value based on 8 CPUs)..... 82

Figure 4-13 Efficient direct reinitialization test on tetrahedral mesh 82

Figure 4-14 Initial *G* value setting for tetrahedral mesh: left picture (a); *G* value after efficient direct reinitialization scheme: right picture (b) (black solid line is the *G* value based on 1 CPU while the dot plot is the *G* value based on 8 CPUs)..... 83

Figure 4-15 Efficient direct reinitialization test on prism mesh 84

Figure 4-16 Initial *G* value setting for prism mesh: left picture (a); *G* value after efficient direct reinitialization scheme: right picture (b) (black solid line is the *G* value based on 1 CPU while the dot plot is the *G* value based on 8 CPUs) 84

Figure 4-17 Energy deposit rate for constant volume case (Table 4-4, Case 1, Case 2 and Case 3 with Cbd= 300, 150, and 120 $\mathrm{kV/J-mm0.5}$, respectively. All three cases are initialized with u' =2.36 m/s)..... 86

Figure 4-18 Comparison of flame kernel radius between experiment [113] and simulation for propane (Table 4-4 Case 1, Case2, and Case 3 with Cbd= 300, 150, and 120 $\mathrm{kV/J-mm0.5}$, respectively. All three cases are initialized with u' =2.36 m/s)..... 87

Figure 4-19 Energy deposit rate for constant volume case (Table 4-4, Case 4 and Case 5 with Cbd= 300 and 120 $\mathrm{kV/J-mm0.5}$, respectively. Both cases are initialized with u' =4.72 m/s)..... 87

Figure 4-20 Flame kernel radius comparison between experiment [113] and simulation for propane (Table 4-4, Case 4 and Case 5 with Cbd= 300 and 120 $\mathrm{kV/J-mm0.5}$, respectively. Both cases are initialized with u' =4.72 m/s)..... 88

Figure 4-21 Wrinkling factor Ξ comparison for different Cbd (Table 4-4 Case 1, Case2, and Case 3 with Cbd= 300, 150, and 120 $\mathrm{kV/J-mm0.5}$, respectively. All three cases are initialized with u' =2.36 m/s), the point where Ξ becomes constant indicates the transition from region (a) to region (b) in ignition model..... 90

Figure 4-22 Wrinkling factor Ξ comparison for different Cbd (Table 4-4, Case 4 and Case 5 with Cbd= 300 and 120 $\mathrm{kV/J-mm0.5}$, respectively. Both cases are initialized with u' =4.72 m/s), the point where Ξ becomes constant indicates the transition from region (a) to region (b) in ignition model..... 90

Figure 4-23 Transition function α for different Cbd values (Table 4-4: Case 1, Case2, and Case 3 with Cbd= 300, 150, and 120 $\mathrm{kV/J-mm0.5}$, respectively. All three cases are initialized with

u' =2.36 m/s). The point where the value of α rises above zero indicates the transition from region (a) to region (b) in the ignition model..... 91

Figure 4-24 Transition function α for different Cbd values (Table 4-4, Case 4 and Case 5 with Cbd= 300 and 120 $\mathrm{kV/J-mm0.5}$, respectively. Both cases are initialized with u' =4.72 m/s), the point where the value of α rises above zero indicates the transition from region (a) to region (b) in the ignition model 91

Figure 4-25 Comparison of radius among experiments, simulation based on swept-volume algorithm, and simulation without swept-volume algorithm (Table 4-4 Case 1, Case2, and Case 3. All three cases are initialized with u' =2.36 m/s) 92

Figure 4-26 Combustion chamber geometry of TCC3 gasoline engine 93

Figure 4-27 Comparison of predicted in-cylinder pressure and HRR with experimental and GT-POWER data for stoichiometric case ((a). comparison of predicted pressure trace and HRR from the swept-volume combustion model and GM model with experiments and GT-Power; (b). the predicted in-cylinder pressure trace from swept-volume model with experimental and GT-POWER data; (c). the predicted in-cylinder pressure trace from both models with experimental and GT-POWER data)..... 96

Figure 4-28 In-cylinder temperature and propane mass fraction contours at different crank angle of swept-volume model (Spark timing = - 18° ATDC). White surface indicates the flame front location..... 97

Figure 4-29 In-cylinder temperature and propane mass fraction contours at different crank angle of GM model (Spark timing = - 18° ATDC). White surface indicates the flame front location .. 98

Figure 4-30 Accumulated HRR comparison between swept-volume and GM models (Stoichiometric case: Table 4-6, Case 1) 99

Figure 4-31 Comparison of predicted in-cylinder pressure and HRR with experimental data ((a). pressure trace comparison between experiment and simulation; (b). accumulated HRR and fuel mass) 100

Figure 4-32 Comparison of pressure trace and heat release rate between experiment and simulations for stoichiometric propane air mixture 101

Figure 5-1 The $G = 0$ flame front (white surface) and propane distribution on the cut plane passing the axis at 4 ms after the start of ignition. ((a). results for the mesh size 1mm; (b) results for the mesh size 0.5 mm.) 103

Figure 5-2 Comparison of the pressure trace and heat release rate between experiment and simulations for the stoichiometric propane air mixture ((a) Pressure trace and HRR of experiments and simulations; (b) Averaged pressure trace comparison between experiment and simulation cycles) 105

Figure 5-3 Comparison of spark current between experiments and simulations ((a) current based on 300 cycles [108]; (b) current based on 30 simulation cycles) 106

Figure 5-4 Comparison of spark voltage between experiments and simulations ((a) voltage based on 300 cycles [108]; (b) voltage based on 30 simulation cycles) 106

Figure 5-5 The effective spark power and spark length from 30 simulation cycles ((a) effective spark power; (b) spark length) 107

Figure 5-6 alpha transition function used for the flame propagation transition from nearly laminar to fully turbulent propagation 108

Figure 5-7 Definition of alpha properties and relationship between those properties ((a) definition of $\alpha = 0.5$ and alpha duration; (b) relationship between alpha duration and $\alpha = 0.5$) 108

Figure 5-8 Relationship among CA10, CA50 and alpha duration ((a) relationship between CA10 and alpha duration for 30 simulation cycles; (b) relationship between CA50 and alpha duration for 30 simulation cycles) 109

Figure 5-9 Flame propagation speed and kernel radius for the 30 simulation cycles ((a) Plasma velocity sp and flame propagation velocity $sflame$; (b) kernel radius) 110

Figure 5-10 The ratio of the curvature inverse to mesh size for seven cycles 111

Figure 5-11 CA10, CA50, and CA90 for 30 simulation cycles ((a) CA10; (b) CA50; (c) CA90) 112

Figure 5-12 Peak pressures and corresponding crank angels for 30 cycles with high (sim05), medium (sim29), and low (sim09) being labeled 113

Figure 5-13 Sensitivity tests (Set the medium case sim29 as the base case and replace its $ksgs, T$ ϕ, and U from high case sim05 and low case sim09 113

Figure 5-14 CA10, CA50, and CA90 after replacing the $ksgs, T$ and ϕ of medium case sim29 from high case sim05 and low case sim09 ((a) CA10; (b) CA50; (c) CA90) 115

Figure 5-15 Subgrid kinetic energy $ksgs$ contours and $ksgs$ on the axis at -20 CA ATDC on the cut plane passing the spark ignition location ((a) $ksgs$ contours on the cut plane; (b) $ksgs$ on the line passing the ignition location (the black dot) as indicated by the white line in the figure to the left) 116

Figure 5-16 Wrinkling factor for high (sim05), medium (sim29) and low (sim09) cycles (the wrinkling factor stops working once it stop increasing at which the alpha transition function starts to work) 117

Figure 5-17 Temperature contours and temperature on the axis at -20 CA ATDC on the cut plane passing the spark ignition location ((a) temperature contours on the cut plane; (b) temperature on the line passing the ignition location (the black dot)) 118

Figure 5-18 Velocity fields and $G = 0$ flame front (red curve) of sim05, sim29, and sim09 at CA = 348 and CA = 354 ((a) sim05; (b) sim29; (c) sim09) 120

Figure 5-19 Comparison of averaged velocity field and burnt probability between experiment and simulation cycles at CA = 348 ((a) averaged fast cycles; (b) averaged slow cycles) 121

Figure 5-20 Comparison of averaged velocity field and burnt probability between experiment and simulation cycles at CA = 354 ((a) averaged fast cycles; (b) averaged slow cycles) 122

Figure 5-21 Effect of transition radius on combustion ((a) pressure trace and heat release rate; (b) alpha transition function; (c) turbulent burning velocity; (d) wrinkling factor) 124

Figure 5-22 CA10, CA50, and CA90 based on transition radius of 1 mm, 2 mm, and 3 mm ((a) CA10; (b) CA50; (c) CA90) 126

Figure 5-23 Effect of keeping kernel center unchanged on combustion ((a) pressure trace and HRR for sim13; (b) pressure trace and HRR for sim16; (c) spark length of sim13; (d) spark length of sim16) 127

Figure 5-24 Effect of fuel on energy deposition ((a) effective energy deposition to gas mixture for sim13; (b) effective energy deposition to gas mixture for sim16; (c) kernel radius of sim13; (d) kernel radius of sim16) 129

Figure 5-25 Pressure traces and HRR comparison between experiments and lean combustion (seven random cycles are chosen for simulations) 130

Figure 5-26 Wrinkling factors for high, medium, and low cycles (high: sim30; medium: sim27; low: sim09) 130

Figure 5-27 Velocity fields and $G = 0$ flame front (red curve) of sim05, sim29, and sim09 at CA = 348 and CA = 354 for lean combustion ((a) sim30; (b) sim27; (c) sim09) 132

List of Tables

Table 3-1 Constants for energy transfer efficiency calculations during arc and glow discharge phases [19] 67

Table 3-2 List of commonly used ignition models and related sub-models (the check symbol indicates that the sub-model is included in that ignition model) 68

Table 3-3 G-Equation and burning velocities formulas for RANS and LES 69

Table 4-1 Burnt volume calculations based on sub-volume algorithm and calculated error comparisons between theoretical and calculated results 72

Table 4-2 Initial condition for case tests 74

Table 4-3 Time consumption comparison for hexahedral, tetrahedral, and prism mesh based on the efficient direct reinitialization scheme 85

Table 4-4 Cases set up for constant volume vessel combustion 86

Table 4-5 Mesh details 93

Table 4-6 Specifications and operating conditions of gasoline TCC3 engine 94

Table 4-7 Accumulated HRR comparison between simulations and experiment (Stoichiometric case: Table 4-6, Case 1) 99

Table 4-8 Accumulated HRR comparison between swept-volume model and experiment (Lean case: Table 4-6, Case 2) 100

Table 5-1 Initial condition setting for constant volume vessel combustion 102

Table 5-2 Specifications and operating conditions of TCC3 engine 104

Table 5-3 Initial global averaged subgrid kinetic energy $ksgs$, temperature T, and equivalence ratio ϕ for high, medium, and low simulation cycles at IVC (-110 CA ATDC) 112

Chapter 1 Introduction

1.1 Background and Motivation

Internal combustion (IC) engines convert chemical energy stored in hydrocarbon fuels into mechanical powers through combustion, which have played a significant role over the past century. However, issues of environmental air pollutants such as nitrogen oxides (NOx), carbon monoxide (CO), carbon dioxide (CO_2), and soot accompany the combustion engines, and these pollutants motivate car manufacturers to reduce engine pollution emissions. The ignition and the following combustion processes are especially important since they affect the fuel economy and further emissions. A substantial number of researchers have been investigating ignition and combustion characteristics over the past several decades. Amid these studies, different ignition and combustion models were developed for various engine operating conditions based on different assumptions. However, even with the application of advanced combustion strategies, the pursuit for high efficiency remains limited by the cycle to cycle variability (CCV). Sources of CCV in combustion of spark ignition (SI) engines can come from many aspects such as variations in mixture motion [5][6][7], cylinder charge [7][8], spark discharge characteristics [8][9], and thermodynamic states at the ignition timing [6][10]. However, the relative importance of those factors is not yet firmly established since these phenomena are strongly coupled with and dependent on engine design and operating conditions. Thus, it can be difficult to predict the unstable nature of engine combustion during the engine design process.

Computational fluid dynamics (CFD) has been a versatile tool to investigate and analyze the performance of internal combustion engines for decades. By simulating the ignition and combustion processes, CFD can provide insights for engineers to improve fuel economy and

reduce emissions. The RANS (Reynolds-averaged Navier-Stokes) approach has been applied to engine cases to study spray, combustion, knocking, and emissions [11][12]. However, RANS suffers from several inherent limitations. First, it is not capable of capturing CCV phenomena in engines due to its ensemble-averaged nature. Second, RANS is not able to mimic turbulent eddy structures since eddies of all sizes are modeled. On the other hand, LES (Large Eddy Simulation) is based on spatial filtering instead of temporal averaging and thus is transient in nature and able to capture the CCV. More details of flow and flame structure can be captured with LES as flow and turbulence are resolved to the grid scale, while eddies smaller than the grid scale are modeled by a sub-grid model. Because of the importance of ignition and combustion on fuel efficiency and cycle-to-cycle variabilities, LES modeling of these two processes has been extensively studied over the years with the purpose of clarifying the relevant parameters to guide numerical model development [13][14][15].

The ignition process plays a significant role in flame kernel development and the subsequent flame propagation process. It was reported that the early stages of combustion are especially susceptible to the CCV of local flow properties around the spark plug, affecting the ignition delay and further successive combustion events [16][17][18]. It was observed by Maly [19] that higher energy deposition tends to create a larger initial flame kernel radius and faster reaction rates, which indicates cycles with higher energy input lead to faster initial flame growth and advanced combustion phasing. The early stage of ignition wields important effects such as ignition delay, kernel growth, and flame propagation on the following combustion process; thus, a model is needed to simulate the ignition process by including more details. Many ignition models have been developed and validated against experiments over the pass decades [20][21][22][23]. In general, a

comprehensive ignition model should include several suitable sub-models to handle the following phenomena [24]:

- Energy transfer from the electric circuit to the gas mixture
- The thermal expansion process after spark kernel formation
- Transition from thermal expansion to flame propagation
- Local flow effects on energy transfer

For most engine cases, combustion can be divided into premixed turbulent combustion, non-premixed turbulent combustion, and partially premixed turbulent combustion. Premixed combustion requires that the oxidizer and fuel be completely mixed before combustion occurs, e.g. spark-ignition (SI) engines. The mixture is ignited by a spark forming a laminar flame kernel. The kernel develops into a rapidly turbulent flame due to the low mean velocity in the cylinder and grows nearly spherically [25]. After the transition from ignition to combustion, the most important quantity needed to be calculated in premixed combustion is the laminar burning velocity, at which flame propagates normal to itself and relative to the flow into the unburnt mixture. This velocity primarily depends on the equivalence ratio, the unburnt mixture temperature, and the pressure. Laminar burning velocity varies based on fuel properties and it has been measured for various fuels over a wide range of the three parameters above [26]. Another important quantity that needs to be modeled is the turbulent burning velocity, which depends on turbulence and the laminar burning velocity.

For non-premixed turbulent combustion or diffusive combustion, fuel and air enter separately into the combustion chamber. The mixture fraction is the most important variable to describe non-premixed combustion, which can help determine the flame surface. The scalar dissipation rate describing the departure from chemical equilibrium is another crucial quantity for non-premixed

combustion [27]. The influence of scalar dissipation rate on the flame structure has been systematically discussed by Peters [28]. In general, if the stoichiometric scalar dissipation rate χ_{st} exceeds the critical value χ_q, the flame will quench. However, it has been demonstrated from both experiments [29] and numerical simulations [30] that instantaneous values of χ_{st} can far exceed χ_q without quenching the flame and that it is possible for the mean scalar dissipation rate below χ_q to extinguish the flame when its fluctuating scalar dissipation rate is above the limit.

In real engine cases, the optimum condition is often achieved between premixed and non-premixed combustion, as seen in stratified combustion featuring better fuel economy and emission. This result is somewhat due to the partially premixed combustion profiting from advantageous features of both while avoiding their adverse effects. In this report, the task is to focus on the development of the ignition model and implementation of G-Equation combustion model for premixed combustion, which could be further extended to partially premixed combustion conditions.

1.2 Objective and Approach

One goal of this work is to develop a comprehensive LES version ignition model WSSIM (Wrinkling and Stretch Spark Ignition Model) by accounting for the effect of turbulence on the flame surface. The WSSIM includes the energy transfer from the electric circuit to the gas mixture, the thermal and chemical effects, the sensitivity to local flow fields and the air/fuel ratio, and the coupling between the Lagrangian and Eulerian phases. In the Lagrangian phase, a kernel is initialized after which a wrinkling factor is calculated to account for the effect of turbulence on wrinkling and stretching the kernel surface. In the Eulerian phase, a transition function is applied when the kernel size exceeds a certain value, which can smoothly transfer the kernel propagation speed from a nearly laminar flame speed to a fully turbulent flame propagation speed.

The second goal of this study is to improve the G-Equation combustion model by implementing a more accurate swept-volume algorithm that can calculate the species reaction rate and heat release rate. First, the G-Equation was implemented in OpenFOAM. Its convection term and propagation term were tested in a combustion bomb, that also had available the measurements of flame isosurface. By comparing the simulated location of G = 0 isosurface with experimental flame surfaces, this validated the G-Equation implementations. In addition, a reinitialization scheme to keep G as a distance function during the whole simulation was implemented and optimized in OpenFOAM. Following this was the development of an innovative swept-volume algorithm used for calculating species reaction rate and coupled with G-Equation model. Finally, the WSSIM was coupled with the G-Equation combustion model to predict the ignition and combustion processes. Model implementations and developments are based on the open source CFD code OpenFOAM [31].

The third goal of current work is to apply the coupled models to both a constant volume bomb and premixed spark ignition transparent combustion chamber (TCC3) engine. In constant volume bomb, the kernel growth was validated against experimental data. In the TCC3 engine, the combustion process, and the causes for CCV phenomenon were analyzed. CCV phenomenon is generally not important to stoichiometric combustion but important to lean combustion due to better fuel efficiency in lean combustion. The capability of the combustion model to handle premixed combustion was thus demonstrated in these applications.

1.3 Outline of the Thesis

The thesis of this project is organized in the following contents of this section:

In Chapter 2, a literature review is provided, which covers the recent development of ignition and combustion models for spark ignition engines. The review also focuses on the characteristics of premixed combustion and on the existing approaches to model the combustion regimes.

In Chapter 3, a combustion model G-Equation, as based on the level set approach, is outlined and its method of implementation into OpenFOAM is described. Following this, the chapter illustrates an innovative swept-volume algorithm to calculate the species reaction rate and an improved reinitialization scheme to keep G as a distance function. Then, what is explained is the development of the ignition model WSSIM composed of four sub-models. Finally, the section ends with a presentation of the combination of the WSSIM and the G-Equation combustion model.

Chapter 4 covers how the experimental data from a constant volume vessel and a TCC3 engine was used to validate the ignition model and the combustion model. The models were validated by comparing the measured and computed kernel radius growth, pressure traces, and heat release. In addition, the swept-volume algorithm and the improved reinitialization scheme were validated by establishing and comparing with several theoretically calculated cases.

In Chapter 5, the coupled model was used to investigate the CCV phenomenon in the TCC3 engine. The coupled model was applied to both stoichiometric combustion and lean combustion. The potential causes for CCV are analyzed along with testing of the sensitivity of related variables.

Chapter 6 offers a summary of the work and postulates some recommendations for the future work in relation to this project.

Chapter 2 Literature Review

This chapter first presents a brief review of ignition models. Next emphasis is given to review the turbulent premixed combustion including the related governing equations, laminar flame structure, related length and time scales, and combustion regimes. Finally, the chapter describes the two types of combustion models applied in spark ignition engines, the turbulence-controlled models, and flamelet models.

2.1 Ignition Models

The ignition process plays a significant role in kernel development and the following flame propagation process. The early flame development has been investigated extensively for decades, and these investigations seek to determine the governing parameters to guide the numerical model development. In the next two subsections, what follows is a description of the spark event and then details of some popular and feasible ignition models.

2.1.1 Ignition Mechanisms

The ignition process involves the conversion of the starting gas from a non-conductive state to a conductive state. Basically, the ignition process can be divided into three phases: breakdown phase, arc phase, and glow discharge phase [8].

2.1.1.1 Breakdown Phase

The first important stage of interest in the ignition is the breakdown phase, which is created by the breakdown of the intervening mixture occurs. The breakdown depends on the overvoltage; the overvoltage is defined as the magnitude difference between applied voltage and threshold [32]. The number of ionizations produced by the electron collision is extremely sensitive to the electron field. Small variations in electron field could result in large variations of electron collisions, hence

the formative time lag with a magnitude around 10^{-8} to 10^{-7} s. Essentially, there are two types of processes in the creation of charges. One are the gaseous processes and the other are the cathode processes [33]. The charges in the gaseous processes are created from the gas molecules itself, while the charges in the cathode processes are created from the solid structure of the negatively charged cathode. In general, there are two kinds of breakdown mechanisms that occur during this breakdown period: the Townsend mechanism and the streamer formation [32]. The Townsend mechanism, a well-studied classic mechanism, is related to the gaseous processes and is a successive development of electron avalanches between the electrodes. One or successive avalanches are produced until the channel conductivity is high enough to create the theoretically infinite and practically limited current by the external circuit [32]. From experimental observations, the time lag is of the order of 10^{-8} s if the voltages are well above the applied breakdown threshold. This short time can be considered to be stationary, and thus the positive and negative ions are not allowed to move even under a pressure of 10 kPa [34]. However, the difficulty in justifying the Townsend mechanism depends on the interpretation of the spark formation mechanism under high pressure situations where the spark channel is recorded to be both zig-zagged and branched [35]. The streamer formation, which also develops in very short time intervals of the order of 10^{-8} s in practical systems, correlates with the cathode processes. In spark ignition engines, streamer discharges can form when the gas mixture is exposed to a large potential difference created by the electric field. This in turn accelerates the electrons to collide with the gas mixture molecules with enough energy to ionize them, knocking an electron off the atom [36]. Significant collisions include elastic collisions, excitations, impact ionizations, and attachments [36]. At the breakdown field, what maintains is a balance between the new electrons caused by the impact ionization and the electrons loss from the attachment. Above the breakdown field, the

number of electrons grows at an exponential speed, leading to the formation of an electron avalanche. Essentially, most of the ionizing processes are composed of the avalanche, including the streamer phenomena. However, the Townsend mechanism disregards the space charge effect that helps build up locally high fields to distort the applied static field [32]. The total resultant field ahead of an avalanche tip will increase while the field behind it will fall [34]. With the field of an avalanche reaching a certain proportion of the applied field, an unstable condition will be established and these will both work together to lead to the spark breakdown [35].

Once the electrode gas has been bridged, the gap impendence drops drastically, the voltage across it collapses, and a high current is formed in a short time to the order of 10 to 20 ns [34]. The peak value of voltage can reach about 10 kV and the resultant peak value of current is about 200 A. Under such a condition, a cylindrical channel with a diameter about 40 μm develops along with a pressure of up to 20 MPa and a rapid temperature rise of up to 60,000 K [37]. The high pressure causes the emission of a pressure wave to make the kernel to expand with very high speeds [38]. Since the temperate could be up to 60,000 K between the spark plug electrodes, the energy transfer efficiency to the gas mixture could be up to 100% and phase duration is about 1 to 10 ns [39].

2.1.1.2 Arc Phase

The driving force during the arc phase is the resistive heating of the plasma by the electric current [37]. The arc phase is characterized by different electron emission mechanisms at the cathode surface. The electrons are emitted from a relatively small cathode spot by the thermos-field emission during the arc phase [40]. To make the electrons get out of the cathode metal, the electrons have to be lifted from the conduction band to the potential of the vacuum, gas, or plasma in front of the cathode because most electrons are at a potential with some volts lower than the potential outside [41]. To achieve this, cathode processes need to assist electrons. Thus, self-

organization is needed for cathode to fulfill just this task, otherwise neither the vacuum discharges nor the self-sustained gas discharges are possible. Once the plasma hits the surface, the potential energy from the combination and the kinetic energy of ions work together to knock out electrons with some finite probability, which is also called the secondary electron emission [41]. A higher ion energy leads to a higher cathode potential drop, which in turn sustains the plasma and generates enough electrons.

The arc fraction of the discharge increases with the increase of pressure due to the compression of the plasma column and the higher current density in the region of cathode spot [40]. Meanwhile, as the plasma column is compressed, the hot high-pressure gas transitions from a cylindrical to a spherical configuration. This process is dominated by the blast wave and violently expanding plasma while the contribution from the chemical reactions can be negligible [34]. The thermal front propagates at a much slower speed than the wave front regardless of the expansion enhancement from the outwards velocities. As the propagation continues, the kernel starts to cool down considerably and the energy stored in the ions and disassociated atoms begins to convert into thermal energy to sustain the expansion process. At the location where a quasi-steady state level of 5,500 to 6,500 K is maintained, a concrete core is established by a continuous supply of the electrical energy.

The heat conduction and diffusion are the main forces that expand the kernel in the arc phase, causing the kernel shape to be more or less spherical. The contributions from the chemical reactions starts to become apparent at this stage. However, the energy transfer efficient is no longer near 100% but reduced to about 50%, primarily due to the heat loss to the electrodes. Besides this aspect of the process, the ionization becomes overwhelmed by the thermal dissociation of the gas.

The maximum current through an arc only limited by the external circuit instead of the arc itself. Usually, the arc phase duration is between 1 to 100 μs.

2.1.1.3 Glow Phase

The phase follows the arc phase is the glow discharge phase. For a normal glow phase, the current density is connected with the possible voltage drop in front of the cathode, which enables the generation processes of electrons [41]. The electron sources can extend over the whole cathode surface if the current is higher. After this interval, the current density must be increased in order to get any further enhancement of the current which in turn needs an increased drop in the cathode potential. For abnormal phase phases, the cathode surface is covered with a steady and calm glow, which contributes to the efficiency of current transfer from the electrode to the discharge plasma. As a result, the active cathode surface becomes exceedingly small, especially under extremely low pressures conditions. The abnormal phase discharge causes the cathode root to be enormously contracted to that cathode spot [41]. For formation of glow discharge, the mean free path of the electrons must be reasonably long but shorter than the distance between the electrodes. Thus, glow discharges do not readily occur under both too low and too high gas pressures [42].

The temperature during the glow phase starts to cool towards the adiabatic flame temperature and the flame kernel evolves into an ellipsoid shape. There are some poles near the electrode surface due to the quenching effect of the relatively colder electrode and the energy loss during this phase is near 70 % [34].

Even the kernel size during the glow phase is still small and the influence of turbulence on the kernel surface is not significant, turbulence already starts to wrinkle the flame surface and the time and length scales come to control the process. The magnitudes of the time and length scales depend on the lifetime of kernel and kernel size, respectively [43].

2.1.2 Ignition Modeling

Although the early stage of ignition produces important effects on the following combustion process, it is not practical to resolve all these processes. Thus, a relatively simple model is needed to simulate the ignition process. Many ignition models have been developed and validated against experiments over passed decades, which are described in the following sub-sections below.

2.1.2.1 Energy Deposition Model

In the energy deposition model, the energy is added to the gas mixture within a prescribed spherical volume and solves the full Navier-Stokes equations for a chemical reactions [20][44]. Overall, the spherical volume is initialized with a radius of the order of 1 mm at the spark gap. Afterwards, the kernel is exposed to be convected with the local mean flow. Then the flame propagates spherically at a constant speed [20] based on mass conservation or fully turbulent burning velocity [44]. Once the kernel displacement exceeds a certain limit, a restrike event occurs.

However, even the combination of massively parallelized CFD computations and the usage of advanced technologies, such as Adaptive Mesh Refinement (AMR), makes feasible the simulation of Eulerian ignition model, the spark energy deposition model is still highly mesh resolution dependent, e.g., the mesh resolution for a spark ignition direct injection (SIDI) engine is required to be about 0.125 mm near the spark ignition region [34]. Besides, the effect of turbulence on the flame surface is not considered.

2.1.2.2 DPIK (Discrete Particle Ignition Kernel) Model

The DPIK is an attempt to apply a Lagrangian method to predict the initial flame propagation developed by Fan et al. [45]. As the spark energy deposition model, the DPIK also assumes the ignition kernel shape to be spherical during the initial ignition process. A set of particles is marked

to indicate the location of ignition kernel and move outwards in radial direction from the spark plug electrodes, as shown in Figure 2-1.

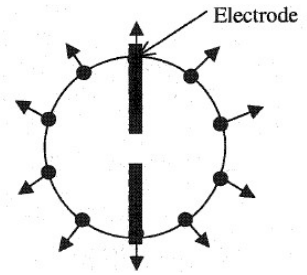

Figure 2-1 DPIK model [46]

Factors influencing the kernel growth rate include the flow turbulence level and the air-fuel mixture stoichiometry. Each particle moves at different speed due to the difference in the local flow turbulent intensity and air-fuel stoichiometry, indicating the shape of the ignition kernel is not guaranteed to be spherical. The kernel growth speed is given as below, as based on the assumption that the pressure increase is negligible due to the combustion and the temperature inside the ignition kernel is uniform and equal to the adiabatic flame temperature [46]:

$$\frac{dr_k}{dt} = \frac{\rho_u}{\rho_k}\left(s_t + s_{plasma}\right) \tag{2-1}$$

where ρ_u and ρ_k are unburnt density and gas density, respectively, and s_t is the turbulent burning velocity. The plasma velocity s_{plasma} can be calculated from the energy balance equation as follows [46].

$$s_{plasma} = \frac{\dot{Q}_{total}\eta_{eff}}{4\pi r_k^2\left[\rho_u(U_k - h_u) + p\frac{\rho_u}{\rho_k}\right]} \tag{2-2}$$

where $\dot{Q}_{total}$ is the total heat transfer rate to the kernel, η_{eff} is the transfer efficiency, U_k is the specific internal energy, and h_u is the unburnt enthalpy. The plasma velocity is inversely proportional to r_k^2 indicating that it decreases rapidly with the increase of kernel radius.

The turbulence integral length scale is usually much larger than the kernel size during the ignition kernel formation process, indicating that only the high frequency fraction of turbulence spectrum could affect the kernel. Based on this, the turbulent burning velocity is given by Herweg et al. [19].

$$\frac{s_t}{s_l} = I_0 + I_0^{1/2}\left(\frac{u'}{u'+s_l}\right)^{1/2}\left(1 - exp\left(-\frac{r_k}{l}\right)\right)^{1/2}\left(1 - exp(-t/T_{0G})\right)^{1/2}\left(\frac{u'}{s_l}\right)^{5/6} \quad (2\text{-}3)$$

where u' is the turbulence intensity, s_l is the laminar burning velocity, and l is the integral length scale. T_{0G} is the characteristic time scale defined as:

$$T_{0G} = \frac{l}{u' + s_l} \quad (2\text{-}4)$$

DPIK model will be joined with combustion models once the kernel radius becomes the order of the integral length scale. In general, the DPIK model is relatively simple and provides some encouraging results to the ignition modeling. However, it does not consider the electrical circuit, the restrike event, and the effects of the local flow fields and local air ratios. Also, the initial kernel radius is empirically selected.

2.1.2.3 AKTIM (Arc and Kernel Tracking Ignition) Model

The AKTIM was developed by Colin et al. [47]. In this approach, Lagrangian marker particles are used to model the evolution of spark channels. Compared with spark energy deposition model and DPIK model, the electric circuitry is also modeled, to which the plasma channel length information is given to model the voltage increases. It also models restrike based on a threshold voltage while ignoring the energy transfer from electric circuit to gas. In sum, the model is composed of four sub-models: the electric circuit model, the spark model, the flame kernel model, and spark the plug model. In the electric circuit model, the energy from the breakdown and arc phases is simulated as a breakdown of energy E_{bd} [47]:

$$E_{bd} = \frac{V_{bd}^2}{C_{bd}^2 d_{ie}} \tag{2-5}$$

where C_{bd} is a constant and d_{ie} is the inter-electrode distance.

The energy deposition process is given as:

$$\frac{dE_s(t)}{dt} = -R_s i_s^2(t) - V_{ie} i_s(t) \tag{2-6}$$

with R_s being the resistance, and V_{ie} being the voltage between the electrodes calculated as the sum of cathode voltage fall, anode voltage fall, and voltage in the gas column along the spark path. i_s is the current:

$$i_s = \sqrt{\frac{2E_s}{L_s}} \tag{2-7}$$

Another important variable needed to calculate is the spark length, which is closely related to the voltage V_{ie}. In the AKTIM, the particles representing the spark length are used to mark the location and further calculate the spark length. Since those particles could be convected by the local flow, the spark length may be as long as many times of the gap between the electrodes. The glow discharge continues if the energy E_s is greater than zero.

Two more ignition models, AKTIMeuler and ISSIM (Imposed Stretch Spark Ignition Model), were extended based on the ATKIM. Compared with AKTIM, the AKTIMeuler model uses an Eulerian progress variable instead of Lagrangian tracers to track the initial kernel [48]. The progress variable is fixed with the CFM (Coherent Flamelet Model) to model the flame propagation and curvature. Further, the wrinkling factor is considered to control the flame brush thickness. Yet, the ISSIM model was optimized based on the AKTIMeuler model in which the flame kernel growth is based on the flame surface density equation [49]. The ISSIM model uses the same electric circuit model as AKTIM and the same flame kernel initialization as AKTIMeuler. The ISSIM makes the multi-ignition description without any ad-hoc adaptation possible by

applying the flame surface density function. Also, it accounts for the effect of stretch of turbulence on the flame kernel growth.

2.1.2.4 Spark-CIMM (Channel Ignition Monitoring Model)

Similar to the AKTIM model, the Spark-CIMM has been developed to predict combustion in stratified-charge, direct injection engines [17][18][23]. The model divides the turbulent flame front propagation into three stages. The first stage is the spark energy deposition, and this stage establishes the spark channel convected and corrugated by the local flow. The Lagrangian marker particles are applied to simulate the spark channel due to its thin thickness and the motion of the spark channel is modeled by a convection equation. Flame kernels are initialized along the spark channel which allows the mixture conditions such as the mixture composition, energy deposition rate, and scalar dissipation rate. Then, the resulting quasi-spherical flame kernels merge together to form a non-spherical and non-symmetric flame front based on the G-Equation model [23]. The flame fronts under this situation remain tracked by the Lagrangian marker particles. Third, the transition from early non-spherical flame into a fully-developed turbulent flame is also computed by the G-Equation model as soon as the flame kernel shape can be resolved by the computational grid, after which the Lagrangian marker particles are removed from the flow field. The Spark-CIMM has combined a detailed spray/evaporation model and a fully developed turbulent flame propagation model to simulate the spray combustion process [17].

Another point of progress the Spark-CIMM facilitates is the monitoring of the gaseous mixture during the spark duration at each of the tracked channel particle locations. These locations are where the formation of local ignition spot is feasible. These formations are controlled by the autoignition processes and triggered by the spark energy deposition rate, thus indicating they are independent from the ability to support the flame front propagation.

However, the energy transfer from the electric circuit to the flame kernel growth is treated in a simplified way, because 60% of the breakdown energy is deposited into the gas mixture and the ignition occurs when the critical energy is reached.

2.2 Turbulent Premixed Combustion

Simulation of premixed combustion is challenging since combustion is accompanied by high temperatures, high chemical reaction rates, and interaction with turbulence. For premixed combustion mode, the fuel and oxidizer are mixed completely before the combustion takes place. Many chemical reactions occur primarily in a thin interfacial region separating the burned and unburned gases to sustain the combustion process. The premixed flame front propagates through the gases until all the mixtures are depleted. The premixed flame speed depends on the balance between convection and diffusion reactions within the inner chemical structure of the flame. The laminar flame structure and the turbulent combustion regimes are discussed in the following sub-sections.

2.2.1 Laminar Premixed Flame Structure

Usually the flame is divided into three zones: a preheat zone, an inner layer, and an oxidation layer, as shown in Figure 2-2. In the preheat zone, the unburnt mixture is first preheated and a little heat is released in this region. Behind the preheat zone is the inner layer, and this is where the fuel is consumed and the chemical reactions mainly occur. The thickness of inner layer is of the order of δ times thinner than the preheated zone. The inner layer temperature T^0 is the crossover temperature between chain-branching and chain-breaking chemical reaction steps [50]. Behind the inner layer is the oxidation zone, and this is where CO and H2 are oxidized to form CO2 and H2O.

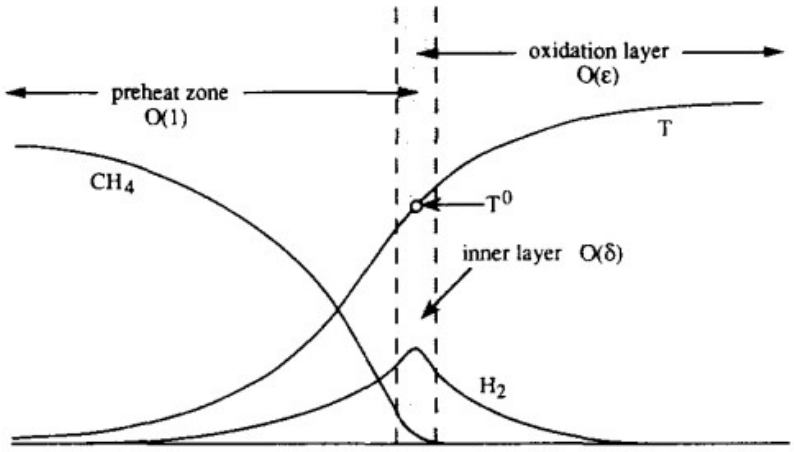

Figure 2-2 Schematic illustration of flame structure of premixed methane-air [51]

The laminar flame thickness is an important length scale in turbulent combustion, which is defined as:

$$l_F = \frac{(\lambda/c_p)_0}{(\rho s_l^0)_u} \tag{2-8}$$

where λ is the heat conductivity and c_p is heat capacity, which are evaluated at the inner layer temperature T^0. ρ and s_l^0 are the density and laminar burning velocity in the unburnt gas. The thickness of the laminar flame is usually of the order of 10^{-5} m [52].

2.2.2 Premixed Turbulent Combustion Regimes

The flame is categorized based on two ratios: (1) the velocity ratio u'/s_L, where u' is the RMS (Root Mean Square) velocity fluctuation and s_L is the laminar burning velocity; (2) the length ratio l/l_F, where l is the integral length scale of the turbulence and l_F is the laminar flame thickness defined as Eqn. (2-8). One can subdivide the domain into several regimes according to these ratios. In general, premixed turbulent combustion can be classified into four regimes: wrinkled flamelet, corrugated flamelet, thin reaction zones, and broken reaction zones, as displayed in Figure 2-3 [53]. One speaks of the wrinkled flame regime at the value of $u'/s_L < 1$. With the increase of turbulence

intensity, flame comes into the corrugated flame regime. The corrugated flame regime exists as turbulence intensity increases until the Karlovitz number reaches unity, as [54]defined by the ratio of the flame to the Kolmogorov time scales below.

$$Ka = \frac{t_F}{t_\eta} = \frac{l_F^2}{\eta^2} \tag{2-9}$$

where $t_F = l_F/s_L$ is the chemical time scale and $t_\eta = (\nu/\varepsilon)^{1/4}$ is the Kolmogorov time scale. The Kolmogorov length scale, the smallest hydrodynamic scale, is defined as $\eta = (\nu^3/\varepsilon)^{1/4}$ with ν the viscosity and ε the dissipation rate per unit mass. This is shown in Eqn. (2-9), unity Ka value implies unity ratio $l_F/\eta = 1$ and is the boundary between the corrugated flamelet regime and the thin reaction zones.

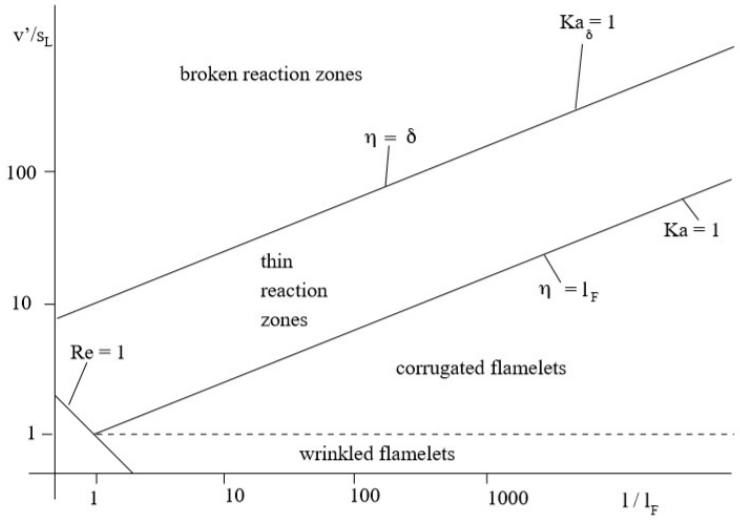

Figure 2-3 Regime diagram for premixed turbulent combustion [53]

One can also define the Karlovitz number in terms of the reaction zone thickness, which is advantageous if the large activation energy asymptotic is taken into account [55]. Under this condition, the flame structure for a one-step chemical mechanism includes a reaction zone and a chemically inert preheat zone, in which the reaction zone thickness is typically one order smaller

than that of the preheat zone. This gives rise to the definition of a reaction zone thickness based Karlovitz number, as seen below.

$$Ka_\delta = \frac{\delta^2}{\eta^2} = Ka\frac{\delta^2}{l_F^2} \tag{2-10}$$

Based on the assumption of unity Schmidt number $S_c = 1$, one can derive the relations between the turbulence intensity u'/s_L and the length scale ratio l/l_F.

$$u'/s_L = Re\left(\frac{l}{l_F}\right)^{-1} = Ka^{2/3}\left(\frac{l}{l_F}\right)^{1/3} \tag{2-11}$$

The line where $Ka_\delta = 1$ or when $\eta = \delta$ depicts the separation between the thin reaction zone and the broken reaction zone. In the thin reaction zone, where the Kolmogorov scale is less than the flame thickness but greater than the reaction zone thickness, the characteristic length scale for this regime is defined as a function of the eddy size in the inertial range with the turnover time t_m being equal to the flame time t_{Flame} [53].

$$l_m = (\varepsilon t_{Flame}^3)^{1/2} \tag{2-12}$$

where $t_{Flame} = l_F^2/D$, with D being the diffusion coefficient.

The interaction between the eddy size and the turbulent flame front can be interpreted as shown in Figure 2-4. In the wrinkled and corrugated flamelet regimes, the flame thickness is even smaller than the smallest eddies with a Kolmogorov scale size. In the wrinkled flamelet regime, the turnover velocity of eddies is smaller than the laminar burning velocity; thus, the eddies cannot wrinkle the flame front. In the corrugated flamelet regime, the turnover velocity of eddies is larger than the laminar burning velocity; thus, the flame front can be corrugated. However, the chemical and transport processes within the flame thickness cannot be perturbed by turbulent eddies of all sizes in these two regimes.

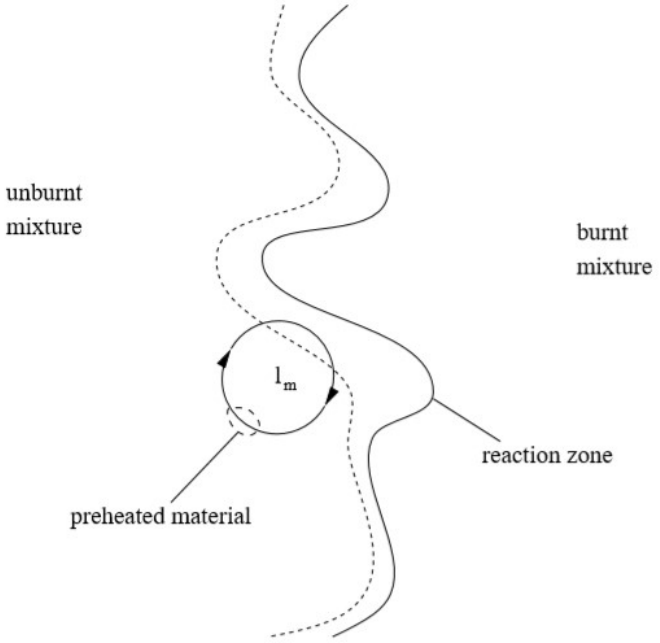

Figure 2-4 Interaction between eddy with size l_m and turbulent flame front [53]

In the reaction zone regime, the smallest eddies can penetrate through preheat zone, which increases the chemical species mixing and heat transfer rates. However, the smallest eddies could not penetrate the inner layer. Therefore, the chemical reactions are not affected.

If the smallest eddies can enter the inner layer, the chemical reaction rates decrease due to the heat and radical species losses, and the flame becomes extinguished locally.

The combustion in spark ignition engines usually falls into the wrinkled flamelet, the corrugated flamelet, and the thin reaction zone regimes [56].

2.3 Turbulent Premixed Combustion Models

Many different premixed turbulent combustion models have been developed. Approaches to turbulent premixed combustion can be classified into two types: turbulence controlled models such as the EBU (Eddy-Break-Up) model [57], and flamelet models such as the level set flamelet model [58].

2.3.1 Turbulence Controlled Models

The idea behind the concept discussed above is that turbulent mixing controls the reaction rate as long as turbulent mixing, rather than chemical reactions, is the rate determining mechanism. Representatives of this kind of model include the Eddy-Break-Up model, the Eddy-Dissipation-Model, and the Characteristic-time model.

2.3.1.1 Eddy-Break-Up Model

For the Eddy-Break-Up (EBU) model, it is based on the idea of Spalding [59]. The rate of fuel consumption is a function of local flow properties and is given as

$$\omega_{fuel} = -C_{EBU}\rho\frac{\varepsilon}{k}Y_{F,rms} \tag{2-13}$$

where C_{EBU} is a model constant, ρ is the density, ε is the turbulent dissipation rate, k is the turbulent kinetic energy, and $Y_{F,rms}$ is the root mean square fuel mass fraction fluctuation. Magnussen and Hjertager applied this model in 1976 with conform experimental results with predictions supported EBU [60]. Nevertheless, the mean reaction rate does not include any effects of chemical kinetics and the EBU model is sometimes linked to the Arrhenius laws to limit the mean reaction rate in commercial software [61]. Dinler and Yucel [62] applied the EBU model to homogeneous charged spark-ignition (SI) engines to investigate the effect of valve angle on the fluid flow and combustion. It was found that for smaller valve angles, the in-cylinder velocities, tumble strength, and flame propagation rates increased. In addition, Jalalifer et.al [63] studied the effect of combustion processes on NOx by applying appropriate constants for the EBU model, the probability density function (PDF), and the coherent flamelet model (CFM). Results showed that the EBU model gave a better NOx prediction than the other two models.

2.3.1.2 Eddy-Dissipation-Model

Magnussen and Hjertager proposed and created the Eddy-Dissipation-Model (EDM) based on the modification of Eddy-Break-Up model [60]. In this model, the turbulence mixes the code reactants and hot products slowly into the reaction zone where rapid reaction occurs. It is said that the combustion under this condition is that the mixing-limited and the unknown chemical kinetics can be safely neglected. Combustion occurs in the location of turbulence existing in the flow and the chemical reaction is controlled by the large eddy mixing time scales. In this model, it takes a minimum of three different rates based on the mean oxidizer mass fraction, mean fuel mass fraction, and mean product mass fraction, respectively, to calculate the chemical reaction rate which is given below.

$$\omega_{fuel} = -\rho \frac{\varepsilon}{k} min\left(AY_F, A\frac{Y_{O2}}{r}, AB\frac{Y_P}{1+r}\right) \tag{2-14}$$

where Y_F, Y_{O2}, Y_P are the mass fraction of fuel, oxygen and products, respectively, A and B are models constants and r is the stoichiometric mass ratio of oxygen to fuel. Zhang and Frankel [64] investigated the natural gas combustion in a Caterpillar G3400 and G3500 fuel-lean-burn natural gas engines. Their outcomes displayed that an optimum initial swirl ratio existed for the central bowl, the central spark plug geometry. However, no ignition models are needed to initiate the combustion in the EDM model and the reactant is assumed to burn the moment it enters the model. This is also the shortcoming of the EDM since the reactant needs some time to rise to the suitable temperature to combust in practice.

One extension of the EDM is the EDC (eddy dissipation concept) which includes detailed mechanisms at an affordable computational cost in turbulence flows. The EDC model attempts to make more accurate combustion predictions by incorporating the significance of structures in a turbulent reaction flow [65]. It assumes that the reaction occurs in those small fine turbulent

structures, which are called fine scales. Compared with the EDM, the EDC has been proven to be more efficient for a vast range of both premixed and diffusion combustion problems without changing the model constants. Though, the typical mechanisms are usually invariably stiff and computationally costly. Thus, the model should be used only when the assumption of fast chemistry is not valid, such as a slow CO burnout modeling [66].

2.3.1.3 Characteristic-Time Model

The Characteristic-Time model (CTC) is also an extension of the EDM and this model assumes that all species densities come to their local thermodynamic equilibrium values after a characteristic conversion time τ_c, which is a sum of a turbulent mixing time τ_t and chemical conversion time, τ_l [56]. The chemical reaction rate is defined by:

$$\frac{d\rho_i}{dt} = -\frac{\rho_i - \rho_i^*}{\tau_c} = -\frac{\rho_i - \rho_i^*}{\tau_t + \tau_l} \tag{2-15}$$

where ρ_i^* is the local equilibrium density for species i. Yet, the reaction rate calculation might be wrong if there is no suitable wall function imposed at the boundaries. The CTC model was widely used in SI engines. It was joined with the discrete particle ignition kernel (DPIK) model by Fan and Reitz [67]. The ignition model and combustion mode were applied to a homogeneous charge Caterpillar SI engine with four different spark-timings. Results demonstrated that with a more sophisticated ignition model, the multidimensional model predictions of spark-ignition engine combustion can be improved significantly. In addition, Reitz et.al [68] applied the CTC to a converted Caterpillar SI engine to simulate the propagation of the regular flame and to predict the occurrence of knock. The in-cylinder temperature distributions for the knocking case showed that auto-ignition indeed occurred in the end gas.

While the CTC model has been confirmed to be capable of predicting global heat release rates and cylinder pressure traces accurately, the major disadvantage of the CTC model is that the model

constants are case sensitive [69]. Besides, it cannot be applied to make assessments of local flame structures. The flame thickness tends to increase during the combustion process due to the diffusion term in the species conservation equations, which is unphysical in experiments of homogenous combustion. In addition, the models seems not to predict reasonable reaction rates near the wall due to the calculation of τ_t and τ_l being inaccurate [34].

2.3.2 Flamelet Models

The flamelet model assumes that chemistry is fast in comparison to the characteristic timescales of turbulence, so that combustion tends to occur in thin layers that are called flamelets. Under the concept of flamelets, the turbulent flame can be treated as an ensemble of one dimensional structural thin flamelets [70]. Representatives of flamelet models are the Bray-Moss-Libby model, the coherent flamelet model, and the level set approach model.

2.3.2.1 Bray-Moss-Libby Model

This model was proposed by Bray and Moss in 1977 [21]. The BML model is developed while assuming large Reynolds and Damkohler numbers [61]. Besides, the flame is expected to be infinitely thin. The BML also expects that there are no intermediate values between unburnt temperature and burnt temperature. To achieve this approximation, a progress variable $\tilde{c}$ is introduced by setting $\tilde{c} = 0$ in the unburnt mixture and $\tilde{c} = 1$ in the burnt mixture. The progress variable is dimensionless and is usually defined as a function of temperature:

$$\tilde{c} = \frac{T - T_u}{T_b - T_u} \tag{2-16}$$

where T_u and T_b are unburnt and burnt temperature, respectively. Also, the progress variable can be defined based on the product mass fraction. One could interpret progress variable as a step function that separates unburned mixture and burned mixture in a given flow field. Thus, it is

related to the flame front structure and statistics, instead of a reacting scalar such as the reactants or products [71]. Based on the progress variable, the mean reaction rate is given as

$$\varpi_c = \rho_u s_l^0 I_0 g \frac{\tilde{c}(1-\tilde{c})}{L_y} \tag{2-17}$$

where I_0 is the stretch factor, s_l^0 is laminar burning velocity of an upstretched flame, L_y is the crossing length scale and g is a model constant. The BML model has been the source of many improvements. For instance, combining a statistical approach using PDF and a physical analysis, the BML model has evidenced some special features, such as counter gradient turbulent transport and flame turbulent generation [61]. By quantifying the quenching rates near the solid boundaries, the BML model was united to simulate the premixed combustion and near wall flame quenching, which was conducted by Malasekera and Ranasinghe [72]. Abu and Cant [73] combined the BML second moment model with the laminar flamelet concept to develop an innovative turbulent reaction rate model in SI engines. The new model displayed no tendency to produce excessive reaction rates in the presence of solid walls as compared with the standard EBU and basic flamelet models.

2.3.2.2 Coherent Flamelet Model

The coherent flamelet model (CFM) considers local regions of the turbulent flame front as interfaces, called flamelets, that separate fuel and oxidizer, at least in the case of a diffusion flame. These flamelets are accounted for by solving a transport equation for the flame surface density. The chemical source term is determined by calculating the local consumption rate of the reactants in the flamelets. This consumption rate is evaluated from analytical formulas or numerical fits to the results of laminar flamelet calculations. CFM has already been applied to diesel engine combustion [74]. The mean reaction rate is calculated as:

$$\varpi_c = \rho_u s_l^0 I_0 \Sigma \tag{2-18}$$

where I_0 is the stretch factor, s_l^0 is laminar burning velocity of an upstretched flame, and Σ is the flame surface density. In the SI engine research field, the CFM model was coupled with the rich flame propagation model to estimate the flame propagation behavior, which was facilitated by Gurupatham and Teraji [75]. Furthermore, Tsuda et.al [76] improved the CFM model by considering flame growth in terms of both the turbulent flame kernel and the laminar flame kernel. The improved model was combined with the knocking prediction model to evaluate the autoignition in SI engines. In addition, the combination of CFM and AKTIM delivered improved predictions for flame acceleration in a rectangular shock tube [77].

One variant of CFM is called the Extended Coherent Flamelet Model (ECFM), a more refined premixed combustion model than the C-Equation, but it requires greater computational effort to converge. The model adopts that the Kolmogorov eddies are larger than the laminar flame thickness, thus indicating that the effect of turbulence is to wrinkle the flame front. In spark ignition engines, the ECFM has been applied in combination with the Lagrangian model to describe the first stage of the flame front propagation process [78]. The range of application of ECFM is the wrinkled flamelet regime where the Damkohler numbers are less than 1 [79].

2.3.2.3 G-Equation Models

In comparison with the models described above, the level set flamelet model, as developed by Peters [25], is based on the premise that the instantaneous turbulent flame is a thin reaction-diffusion layer embedded in an otherwise inert turbulent flow field. By setting the level set variable $G = 0$ on the flame surface, $G > 0$ in the burnt region and $G < 0$ in the unburnt region. It is relatively easier to find the flame front by tracking the $G = 0$ contour line or surface. Furthermore, G is a non-reacting scalar, therefore a source term does not exist in its transport equation, which could further simplify the calculation. The G-Equation model has been extensively used in SI engines.

For instance, Tan and Reitz [58] employed the G-Equation and DPIK models to simulate the ignition and combustion in SI engines. In addition, the G-Equation was incorporated with detailed chemical kinetics to model knock in SI engines by Liang et.al [80].

The G-Equation model was adopted in the present work. The details about G-Equation model are presented in Chapter 3.

Chapter 3 Model Development and Implementation in OpenFOAM

In this chapter, the G-Equation model first is described, then followed by a swept-volume algorithm designed for the G-Equation that can calculate the chemical reaction rate in the governing equations. Secondly, the chapter presents both an improved reinitialization scheme for hexahedra mesh and its extension to non-hexahedra mesh. Then, this chapter explains the development of an LES version ignition model including four sub-models to involve more physical ignition details. Finally, the chapter ends by describing the combination of the ignition model and the G-Equation combustion model.

3.1 G-Equation Implementation

In this section, first the *G* transport equation is introduced. Following this, the numerical implementation was verified by means of a variety of simplified test cases. Then, an advanced algorithm used to calculate the species reaction rate is presented. Finally, a potential problem related to the G-Equation model is explained along with the solution to the problem.

3.1.1 G-Equation Description of Turbulent Flame Propagation

Level set methods have generally been used for capturing interface evolution, especially when the interface undergoes extreme topological changes such as merging or pinching off [81]. The *G* Equation is a level set approach that can be used to track the flame surface during the combustion process where the flame front is at $G = G_0$ as shown in Figure 3-1. Thus, an implicit representation of the instantaneous flame surface could be given as:

$$G(\vec{x}, t) - G_0 = 0 \tag{3-1}$$

Here, $\vec{x}$ is the vector of space coordinates and *t* is the time. Differentiating Eqn. (3-1) with respect $\vec{x}$ and *t*, one obtains:

$$\frac{\partial G}{\partial t} + \frac{d\vec{x}_f}{dt} \cdot \nabla G = 0 \tag{3-2}$$

where $\vec{x}_f$ is the location of the flame front. If the flame thickness is locally smaller than the curvature radius of the instantaneous flame front, then the flame is in the corrugated regime and the propagation speed is given by:

$$\frac{d\vec{x}_f}{dt} = \vec{u} + s_{L0}\vec{n} \tag{3-3}$$

Here, $\vec{u}$ is the local flow velocity, s_{L0} is the laminar flame speed, and $\vec{n}$ is the flame surface normal directed into the unburnt mixture which can be expressed as:

$$\vec{n} = -\frac{\nabla G}{|\nabla G|} \tag{3-4}$$

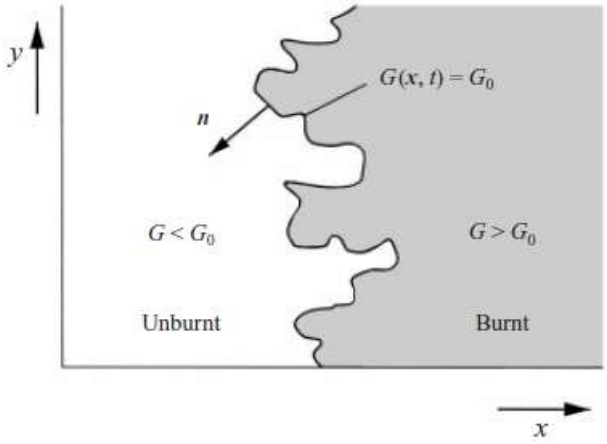

Figure 3-1 G value definition for premixed turbulent flames [82]

Combing Eqn. (3-2), Eqn. (3-3), and Eqn. (3-4) yields the instantaneous G-Equation:

$$\frac{\partial G}{\partial t} + \vec{u} \cdot \nabla G = s_L |\nabla G| \tag{3-5}$$

Based on the investigation of [83], the laminar flame speed s_{L0} can be reformulated as:

$$s_{L0} = s_L^0 - s_L^0 L\kappa - LS \tag{3-6}$$

where s_L^0 is the burning velocity of the unstretched planar flame and κ is the flame curvature defined as:

$$\kappa = \nabla \cdot \vec{n} = \nabla \cdot \left(-\frac{\nabla G}{|\nabla G|} \right) \tag{3-7}$$

The term L is the Markstein length, which describes the effect of curvature and strain on the flame front. S is the strain rate on the flame imposed by the velocity gradient and is expressed as:

$$S = -\vec{n} \cdot \nabla \vec{u} \cdot \vec{n} \tag{3-8}$$

Therefore, the final G-Equation for the laminar flame based on the above equations is given as:

$$\frac{\partial G}{\partial t} + \vec{u} \cdot \nabla G = s_L^0 |\nabla G| - s_L^0 L \kappa |\nabla G| - LS|\nabla G| \tag{3-9}$$

G is usually defined as a distance function by convention. In general, the G value is set to be greater than 0 in the burnt domain, less than 0 in the unburnt domain, and equal to 0 at the flame front, as shown in Figure 3-1. Indeed, the location of $G = 0$ can be defined to be anywhere in the flame, for instance at a given temperature isosurface [84]. Assuming the $G = 0$ flame surface is initialized (for example by an ignition model), the remaining G values need to be initialized as a distance function before its transport equation (listed above) is calculated. The magnitude of the G value at a certain location is equal to its smallest distance to the $G = 0$ isosurface, as displayed in Figure 3-2.

In Figure 3-2, the red line represents the flame surface where $G = 0$. On the left side of $G = 0$ isovalue line is the burnt region and on the right side is the unburnt region. In OpenFOAM, the G value is stored at each cell center. Thus, to initialize the G value at each cell center, one needs to calculate the smallest distance from that certain cell center to the $G = 0$ isosurface. For instance, the G value at cell 1 is equal to the magnitude of green line (Line 1) perpendicular to the green line (Line 2), which is tangent to the $G = 0$ red line. Since cell 1 is in the burnt region, its G value is given a positive sign. For cell 2, the same approach is applied except that a negative sign is assigned

to its G value at the cell center, due to it being in the unburnt region. This is also the so-called initialization process after which the G field becomes a distance function satisfying $|\nabla G| = 1$.

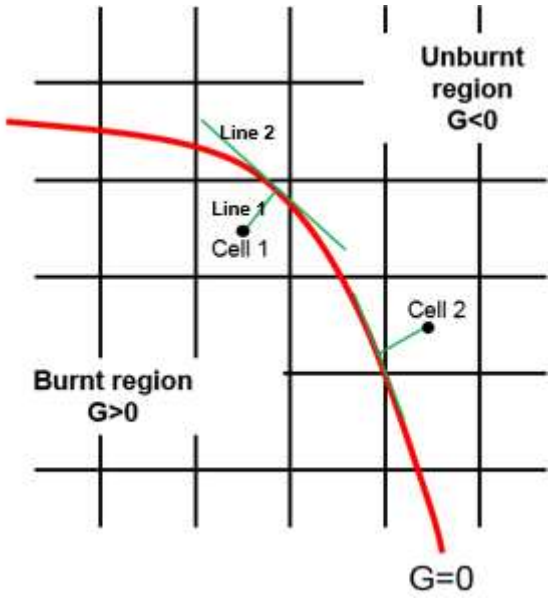

Figure 3-2 G value determination in combustion domain

3.1.2 G-Equation for the Corrugated and Thin Reaction Flamelet Regimes

In the corrugated flamelet regime, the flame structure is not disturbed by the turbulence eddies. Thus, the G-Equation of Eqn. (3-9) describing the laminar flame propagation still holds here. When compared with the unstretched laminar propagation term $s_L^0|\nabla G|$, the curvature term $s_L^0 L\kappa|\nabla G|$ and the strain term $LS|\nabla G|$ are smaller [25]. These can be neglected, which leads to a reduced G-Equation formatted, as given below:

$$\frac{\partial G}{\partial t} + \vec{u} \cdot \nabla G = s_L^0 |\nabla G| \tag{3-10}$$

In the thin reaction zone regime, the smallest eddies, Kolmogorov eddies, can penetrate the preheat zone and cause unsteady perturbations of the flame. Under this situation, where the laminar burning velocity is not well defined, Eqn. (3-9) could not be used directly. However, the inner layer remains laminar since it is not penetrated by the turbulence. Hence, the flame front where G

= 0 coincides with the iso-temperature surface in the inner layer, leading to another format of G-Equation [25]:

$$\frac{\partial G}{\partial t} + \vec{u} \cdot \nabla G = (s_n + s_r)|\nabla G| - D\kappa|\nabla G| \tag{3-11}$$

Here, s_n is the displacement speed due to normal diffusion and s_r is the displacement speed due to chemical reaction. D is the thermal diffusivity and κ is the curvature defined in Eqn. (3-7). s_n and s_r are defined as:

$$s_n = \frac{\vec{n} \cdot \nabla(\rho D \vec{n} \cdot \nabla T)}{\rho|\nabla T|} \tag{3-12}$$

$$s_r = \frac{\dot{q}_T}{\rho|\nabla T|} \tag{3-13}$$

where ρ is density, T is temperature, and $\dot{q}_T$ is the heat release through chemical reactions.

Although the analysis showed that the displacement speed composed of s_n and s_r is one order of magnitude smaller than the curvature term, the sum of s_n and s_r is still of the same order magnitude as the laminar burning velocity, as confirmed by the DNS (Direct Numerical Simulation) data evaluation [85]. Besides, it was also found that the mean values of s_n and s_r slightly depends on curvature, thus leading to the modification of diffusion coefficient by accounting for the Markstein effects, However, this modification is suggested to be ignored and the Eqn. (3-11) is retained [25] for thin reaction flamelet regime.

3.1.3 G-Equation for Both Regimes

Eqn. (3-10) and Eqn. (3-11) are valid for corrugated flamelet regime and thin reaction zone regime, respectively. For convenience, a common G-Equation for both regimes is written as:

$$\frac{\partial G}{\partial t} + \vec{u} \cdot \nabla G = s_L^0|\nabla G| - D\kappa|\nabla G| \tag{3-14}$$

To be consistent with other field equations, which is used as a starting stage for turbulence modeling, the density ρ is multiplied on both sides of Eqn. (3-14), the G-Equation becomes [25]:

$$\rho\frac{\partial G}{\partial t}+\rho\vec{u}\cdot\nabla G=(\rho s_L^0)|\nabla G|-(\rho D)\kappa|\nabla G| \tag{3-15}$$

where the product ρs_L^0 is the mass flow rate through an unstretched planar flame that is constant due to mass conservation, $\vec{u}$ is the flow velocity at the flame front, D is the thermal diffusion coefficient, and κ is the curvature.

3.1.4 RANS and LES Versions of G-Equation

One can split G and flow velocity $\vec{u}$ into two terms: Favre mean and fluctuation, which are listed below:

$$G=\tilde{G}+G'' \tag{3-16}$$

$$\vec{u}=\tilde{\vec{u}}+\vec{u}'' \tag{3-17}$$

The location where Favre mean variable $\tilde{G}=0$ represents the mean flame front, which can be calculated from $\tilde{G}=\overline{\rho G}/\bar{\rho}$. Putting Eqn. (3-16) and Eqn. (3-17) into Eqn. (3-15), one obtains:

$$\bar{\rho}\frac{\partial\tilde{G}}{\partial t}+\bar{\rho}\tilde{\vec{u}}\cdot\nabla\tilde{G}=(\rho s_L^0)\left|\nabla\tilde{G}\right|-\nabla\cdot\left(\bar{\rho}\widetilde{\vec{u}''G''}\right) \tag{3-18}$$

where the term ρs_L^0 is not averaged because this term is constant due to mass conservation. Thus, the mass flow rate through the flame maintains the relationship $\bar{\rho}\tilde{\vec{u}}=\rho s_L^0=\bar{\rho}s_T$, with s_T being the turbulent burning velocity, and is assumed to depend only on local mean quantities [46].

Based on the gradient assumption, the last term in Eqn. (3-40) can be rewritten as:

$$\nabla\cdot\left(\bar{\rho}\widetilde{\vec{u}''G''}\right)=\bar{\rho}D_t\tilde{\kappa}\left|\nabla\tilde{G}\right| \tag{3-19}$$

where D_t is the turbulent diffusivity and $\tilde{\kappa}=\nabla\cdot\tilde{\vec{n}}=\nabla\cdot\left(-\frac{\nabla\tilde{G}}{|\nabla\tilde{G}|}\right)$is the curvature. Then the G-Equation is reduced to be:

$$\bar{\rho}\frac{\partial\tilde{G}}{\partial t}+\bar{\rho}\tilde{\vec{u}}\cdot\nabla\tilde{G}=\bar{\rho}s_T\left|\nabla\tilde{G}\right|-\bar{\rho}D_t\tilde{\kappa}\left|\nabla\tilde{G}\right| \tag{3-20}$$

If s_T is estimated at the unburnt gas conditions, the RANS transport equation of G is given below.

$$\frac{\partial \tilde{G}}{\partial t} + \vec{u} \cdot \nabla \tilde{G} = \frac{\overline{\rho_u}}{\bar{\rho}} \cdot s_T \left|\nabla \tilde{G}\right| - D_t \tilde{\kappa} \left|\nabla \tilde{G}\right| \quad (3\text{-}21)$$

where $\frac{\overline{\rho_u}}{\bar{\rho}}$ is the ratio of unburnt density to flame cell density. There are four terms in the *G* transport equation: a time term, a convection term, a propagation term, and a curvature term, as listed from left to right. Since *G* is a non-reacting scalar, there is no need to add a source term in its transport equation, which further simplifies the calculation and reduces the computational expense.

One of the goals of current study is to combine the WSSIM with G-Equation, in order to investigate the cause for CCV phenomena. Therefore, an LES version of *G* transport equation is needed, which is formulated below [84]:

$$\frac{\partial \tilde{G}}{\partial t} + \vec{u} \cdot \nabla \tilde{G} = \frac{\overline{\rho_u}}{\bar{\rho}} \cdot s_{flame} \left|\nabla \tilde{G}\right| \quad (3\text{-}22)$$

where $\overline{\rho_u}$ is the unburnt gas density and $\bar{\rho}$ is the flame containing cell density. The variable s_{flame} will be described in the ignition model section.

When compared with RANS version of G-Equation, the LES version of G-Equation does not show the curvature term. The reason for this difference is that the curvature term is incorporated in the term s_{flame} as described by [84].

3.1.2 G-Equation Tests

Three computational experiments were used to test the G-Equation. The first one is referred to as "circle growth," the second is referred to as "circle moving," and third is called "circle disappearing."

3.1.2.1 Circle Growth

In the "circle growth" test, the turbulent burning velocity s_T is set to 0.2 m/s while the convection term and curvature term are set to zero. The circle radius is initialized as 10 mm. Thus,

the reduced *G* transport equation is displayed as Eqn. (3-23). The physical meaning is a circle with an initial radius of 10 mm grows radially at a prescribed speed of $s_T = 0.2$ m/s. The results of circle growth are shown in Figure 3-3.

$$\frac{\partial \tilde{G}}{\partial t} = s_T \left| \nabla \tilde{G} \right| \tag{3-23}$$

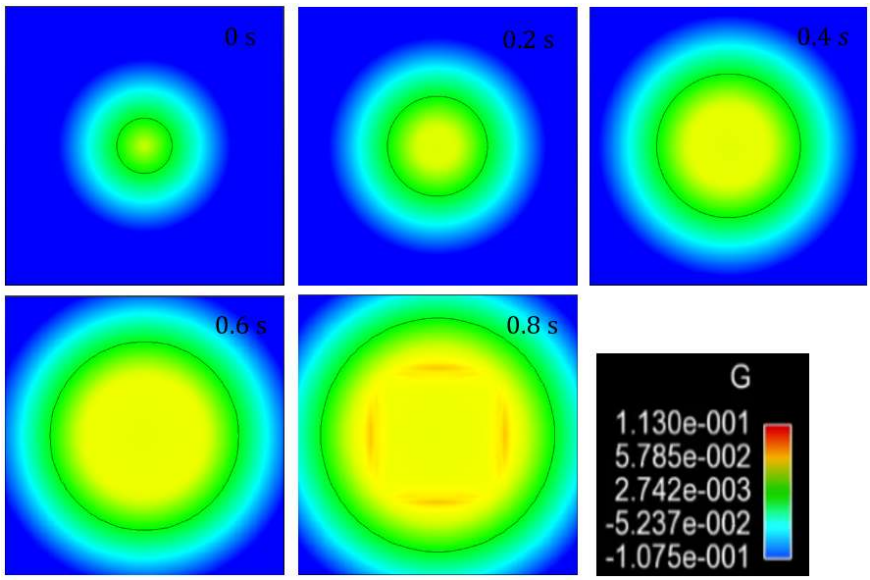

Figure 3-3 Growth of the calculated sphere (black circle represents $G = 0$) using Eqn. (3-23)

Figure 3-3 shows the computed growth of the calculated circle at five separate times. The circle radius at time 0 s is 10 mm. It can be seen that the circle remains a circle without changing its shape perceptibly. The circle radius growth velocity calculated from the test is 0.2 m/s, which is the same as the prescribed flame velocity of 0.2 m/s.

3.1.2.2 Circle Moving

In the "circle moving" test, the velocity $\vec{u}$ in the convection term is set to (0.3, 0, 0) m/s while the propagation term and curvature term are set to zero. The circle radius is initialized as 10 mm. Thus, the reduced *G* transport equation is displayed as Eqn. (3-24). The physical meaning is a circle with an initial radius of 10 mm that moves in the x direction at a prescribed speed of $\vec{u} =$ (0.3, 0, 0) m/s. The results of circle moving is shown in Figure 3-4.

$$\frac{\partial \tilde{G}}{\partial t} + \vec{u} \cdot \nabla \tilde{G} = 0 \tag{3-24}$$

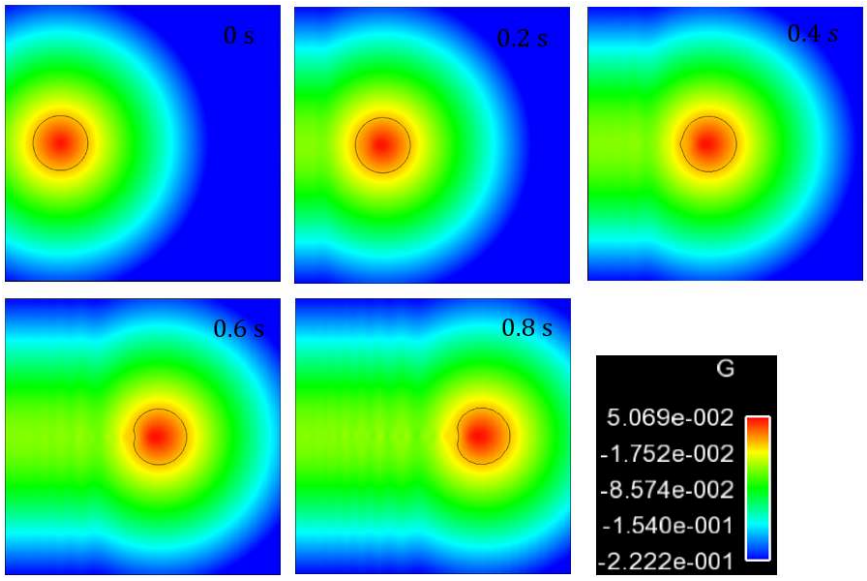

Figure 3-4 Moving of the calculated sphere (black circle represents $G = 0$) using Eqn. (3-24)

Figure 3-4 shows the computed location of the calculated circle at five diverse times. The circle radius at time 0 s is 10 mm. One can observe that the circle moves at a certain speed as time progresses. The moving velocity calculated from the test was 0.3002 m/s, which is remarkably close to the prescribed velocity 0.3 m/s.

Please note, it is obvious that the G field does not keep as its original shape while moving forward and that there are some oscillations following the $G = 0$ circle. One cause for these results is the boundary condition of the G field, which is set to be zero gradient, namely $\left|\nabla \tilde{G}\right| = 0$, in this test case. However, since G is a distance function that requires $\left|\nabla \tilde{G}\right| = 1$, the above boundary condition setting is one of factors leads to oscillations in the test case. Another reason for the oscillations is because the Eqn. (3-24) is purely hyperbolic with no damping under the CFL (Courant-Friedrichs-Lewy) number, that being 0.4. One of the solutions to this problem is to apply a reinitialization scheme to reset the G field as a distance function during the calculation, which is described in the later sections.

3.1.2.3 Circle disappearing

In the "circle disappearing" test, the velocity $\vec{u}$ in the convection term is set to (0.3, 0, 0) m/s, the coefficient D_t is set to 0.02 m^2/s, and the propagation term is set to zero. The circle radius is initialized as 10 mm. Thus, the reduced G transport equation is displayed as Eqn. (3-25). The physical meaning is a circle with an initial radius of 10 mm moves in the x direction at a prescribed speed of $\vec{u} = (0.3, 0, 0)$ m/s. Meanwhile, the circle dissipates during the circle moving process. The results of moving and dissipating circle are shown in Figure 3-5.

$$\frac{\partial \tilde{G}}{\partial t} + \vec{u} \cdot \nabla \tilde{G} = -D_t \tilde{\kappa} \left| \nabla \tilde{G} \right| \tag{3-25}$$

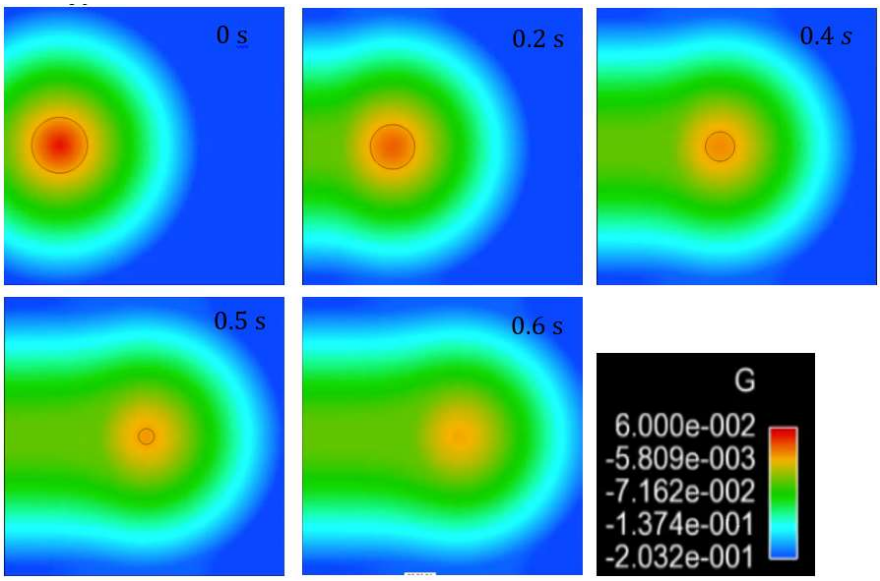

Figure 3-5 Moving of the calculated sphere (black circle represents $G = 0$) using Eqn. (3-25)

Figure 3-5 shows the computed location of the calculated circle at five different times. The circle moves at a certain speed as time progresses. Meantime, the circle becomes smaller and smaller. The circle disappears at time = 0.6 s.

3.1.3 Laminar and Turbulent Flame Speed Correlations

In premixed combustion, the laminar flame speed is defined as an unstretched laminar flame propagating through a quiescent mixture of unburnt reactants that depends upon three properties of the mixture: temperature, thermal diffusivity, and reaction rate. During the past several decades, two main methods have been crafted to calculate the laminar burning velocity and flame structures. The first approach is to solve the ordinary differential equations of heat conduction, diffusion, and species continuity where the flame speed is calculated as the eigenvalue of the two-point boundary value problem [86]. The second method applies finite difference methods to solve the continuity and time-dependent energy conservation equations [87].

However, for many applications, including engines, the laminar burning velocity is obtained from correlations of experimental data. For the laminar burning velocity s_L, there are three popular correlations: Müller [88], Gülder [89], and Metghalchi [90], which are listed below. To give an enhanced comparison of these three correlations, the comparison chosen was propane and air mixture with an initial temperature of 300 K and pressure of 1 atm.

$$s_L = Fexp\left(-\frac{G_1}{T^0}\right) Y_{F,u}^m \frac{T_u}{T^0}\left(\frac{T_b - T^0}{T_b - T_u}\right)^n \tag{3-26}$$

$$s_L = s_{uo}(\phi)\left(\frac{T_u}{T_0}\right)^{\alpha}\left(\frac{p}{p_0}\right)^{\beta}(1.0 - f \cdot F) \tag{3-27}$$

$$s_L = s_{uo}(\phi)\left(\frac{T_u}{T_0}\right)^{\alpha}\left(\frac{p}{p_0}\right)^{\beta}(1.0 - 2.1f) \tag{3-28}$$

Figure 3-6 shows the comparison between experiments and the three laminar burning velocity correlations. The series titled as “Experiment 1” and “Experiment 2” are experimental data that are extracted from [89] and [90], respectively. As can be seen in the figure, the results from the Metagalchi correlation under-predict the experimental findings, while the results from Müller correlation generally over-predict the experimental findings. As a comparison, the results from

Gülder correlation are in the strongest agreement with the experimental data. Based on this, the Gülder correlation is used in the swept-volume combustion model developed through this study.

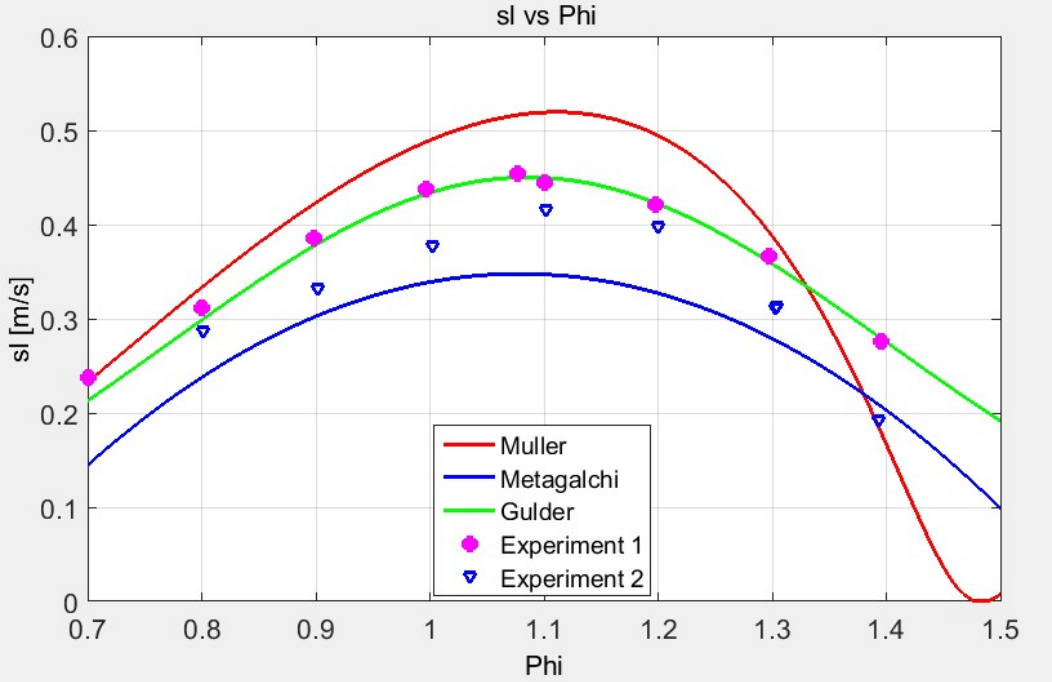

Figure 3-6 Comparison between experiments [88][89][90] and laminar burning velocity correlations (Propane, p = 1atm, T = 300 K)

In the G transport equation, the propagation term is related to the turbulent burning velocity s_T. The turbulent burning velocity s_T is the key term that establishes the link between the G-Equation model and the combustion model. Typically, there are two versions of s_T: RANS and LES. The RANS version of s_T can be evaluated from [25].

$$\frac{s_T}{s_L} = 1 + \left\{ -\frac{a_4 b_3^2}{2b_1} Da + \left[\left(\frac{a_4 b_3^2}{2b_1} Da \right)^2 + a_4 b_3^2 Da \right]^{1/2} \right\} \frac{u'}{s_L} \tag{3-29}$$

In which, s_L refers to the laminar burning velocity, u' is the turbulent intensity, and Da is the Damkohler number defined as $Da = s_L l / u' l_F$. The constant b_1 is case dependent, a_4 and b_3 are 0.78 and 1.0, respectively. Moreover, l_F is the laminar flame thickness, l is the integral length scale, and in k-epsilon turbulence model l is evaluated as:

$$l = 0.1643 \frac{k^{1.5}}{\varepsilon} \tag{3-30}$$

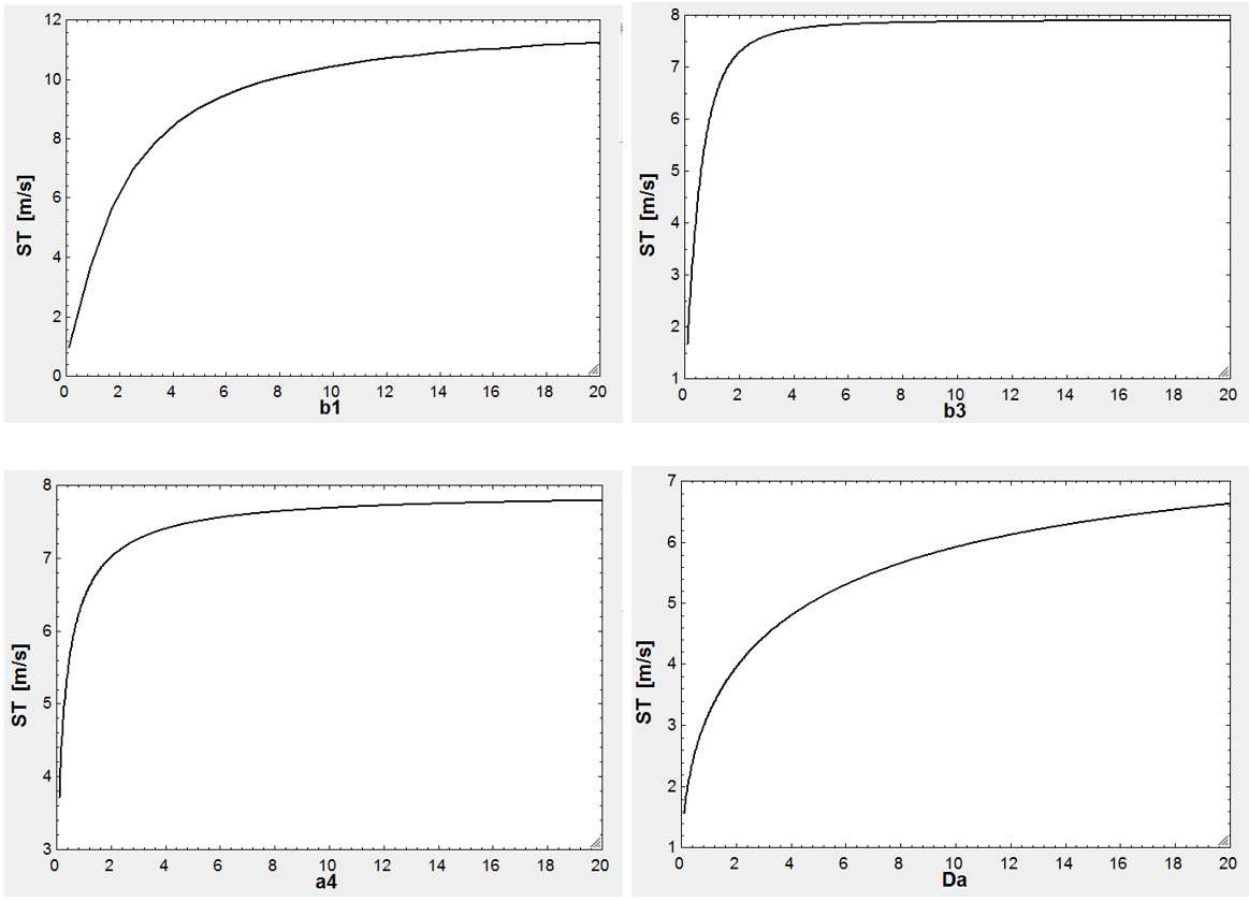

Figure 3-7 Relationship between s_T correlation and its related parameters

($k = 20 \frac{\mathrm{m}^2}{\mathrm{s}^2}$, *epsilon* = $7340 \frac{\mathrm{m}^2}{\mathrm{s}^3}$)

To evaluate the role that each parameter plays, it is worth displaying the value of s_T as a function of related parameters. Furthermore as Figure 3-7 shows, the relationship between the turbulent burning velocity s_T and its related parameters are based on the given *k* and *epsilon*. The given *k* and *epsilon* correspond to an integral length scale of about 2 mm, which is common in engine cases. One can see that increasing b_1, b_3, a_4 and *Da* lead to higher s_T values. Even though

the parameters b_1, b_3 and a_4 are case dependent [44], researchers usually adjust b_1 to change the turbulent flame speed because b_1 usually has the strongest effect [12].

Compared with RANS, models developed based on LES can capture the CCV and flow structures in engines, so the LES version of s_T is evaluated from [84]:

$$\frac{s_T - s_L}{s_L} = -\frac{b_3^2 C_v}{2b_1 Sc_{t,G}}\frac{\Delta}{l_F} + \left[\left(\frac{b_3^2 C_v}{2b_1 Sc_{t,G}}\frac{\Delta}{l_F}\right)^2 + \frac{b_3^2 D_t}{s_L l_F}\right]^{\frac{1}{2}} \tag{3-31}$$

where $b_3 = 1, C_v = 1, Sc_{t,G} = 0.5$, Δ stands for the filter size, l_F is the laminar flame thickness, s_L is the laminar burning velocity, and b_1 is a user defined parameter. D_t would generally be called eddy diffusivity and is formulated as:

$$D_t = \frac{C_v \Delta u_{sgs}}{Sc_{t,G}} \tag{3-32}$$

In this model,

$$u_{sgs} = \frac{\nu_t}{0.12\Delta} \tag{3-33}$$

$$\nu_t = 0.094\Delta\sqrt{k_{sgs}} \tag{3-34}$$

The sub-grid kinetic energy is calculated though the dynamic structure turbulence model whose transport equation is given below [91]:

$$\frac{\partial \bar{\rho} k_{sgs}}{\partial t} + \frac{\partial \bar{\rho}\widetilde{u_j} k_{sgs}}{\partial x_j} = -\bar{\rho}\Gamma_{ij}\widetilde{S_{ij}} - C_e\frac{k_{sgs}}{\Delta} + \frac{\partial}{\partial x_j}\left(\bar{\rho}\nu_{sgs}\frac{\partial k_{sgs}}{\partial x_j}\right) \tag{3-35}$$

where $C_e = 0.3$ and Δ is calculated as the mesh resolution.

3.1.4 Combustion Model

There are three classic types of *G*-based reaction rate calculations for combustion models. The following subsections introduce these three types of reaction rate calculations and their related drawbacks. Next, what is introduced is an innovative combustion model.

3.1.4.1 PDF (Probability Density Function)

The probability density function of flame front fluctuation is measured to be similar to the Gaussian distribution, being slightly skewed to the unburnt gas side due to the nonsymmetrical influence of laminar burning velocity on the flame front [25]. The PDF model is developed based on this discovery.

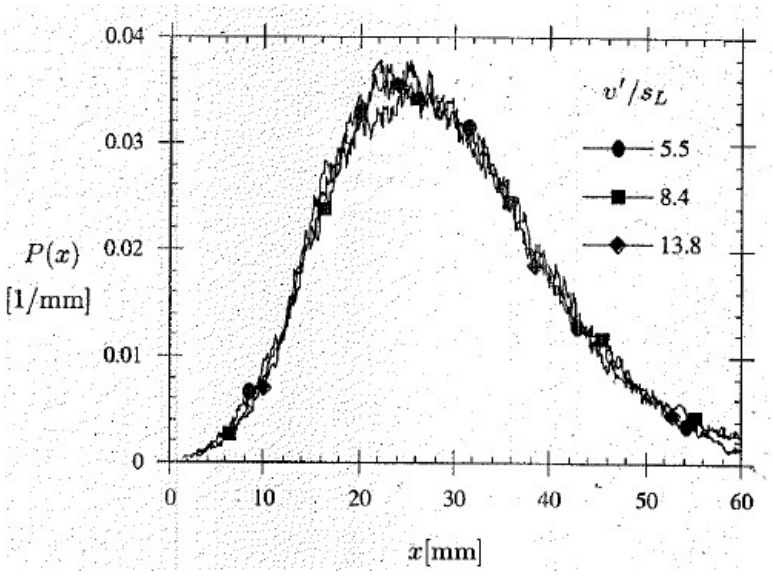

Figure 3-8 Probability density of finding the instantaneous flame front [25]

In the PDF model, the probability of finding the instantaneous flame front is assumed to be the Gaussian distribution as shown in Figure 3-8. Species mass fraction in the computational cells located within the flame brush is expressed as [70][92]:

$$\overline{Y}_i = f\overline{Y}_{i,b} + (1-f)\overline{Y}_{i,u} \tag{3-36}$$

where $\overline{Y}_{i,b}$, $\overline{Y}_{i,u}$ are the burnt and unburnt species mass fraction for species i. Besides, f is the probability of finding burnt gas which can be modeled as:

$$f(G>0) = \int_0^{\infty} \frac{1}{\sqrt{2\pi\left(\widetilde{G''^2}\right)_0}} exp\left(-\frac{\left(G-\tilde{G}\right)^2}{2\left(\widetilde{G''^2}\right)_0}\right) \tag{3-37}$$

where G''^2 is the variance of the G field and can be obtained by either by solving a G''^2 transport equation [25] as Eqn. (3-38) where $\nabla_{//}$ is tangential gradient operator or through the turbulence integral length scale [70] as Eqn. (3-39).

$$\bar{\rho}\frac{\partial\widetilde{G''^2}}{\partial t} + \bar{\rho}\,\bar{v}\cdot\nabla\widetilde{G''^2} = \nabla_{//}\cdot\left(\bar{\rho}D_t\nabla_{//}\widetilde{G''^2}\right) + 2\bar{\rho}D_t\left(\nabla\tilde{G}\right)^2 - c_s\bar{\rho}\frac{\tilde{\varepsilon}}{\tilde{k}}\widetilde{G''^2} \tag{3-38}$$

$$l_{F,t} = \left.\frac{\left(\widetilde{G''^2}\right)^{1/2}}{\left|\nabla\tilde{G}\right|}\right|_{\tilde{G}=0} = 1.78l \tag{3-39}$$

However, it was shown that these implementations were too computationally expensive and usually the turbulent flame structure cannot be resolved in engine cases [46].

3.1.4.2 Xiaofeng Model

This model was developed by Xiaofeng Yang [44] which is employed in spark ignition engine simulations. This model is a type of flamelet models and is valid only for a one-step reaction. It assumes that reactants after the flame are completely converted into products. The implementation is simple, and computation is less expensive compared with reaction rate calculation based on PDF model. The reaction rate treatment at the flame front is given as:

$$\omega = \delta\frac{s_T\Delta t A_F}{V_c}AT_c^n exp\left(-\frac{E}{RT_c}\right) \tag{3-40}$$

where δ is a smoothing function, s_T the turbulent burning velocity, A_F flame area and V_c cell volume. To be consistent with ref. [44], the Müller correlation [88] for laminar burning velocity is applied.

However, this combustion model is only valid for a one-step reaction and the model is difficult to extend to detailed chemistry. On the other hand, the smoothing function δ is given as a function of G and the flame thickness where the flame thickness is usually empirically set instead of based on calculation for reaction rate controls. For instance, the flame thickness l_F is usually set as a constant value of two mesh cell size and is thus mesh dependent. Based on this setting, the value

of δ changes from 0 to 1 in these two mesh cell regions with other regions being zero. However, this setting, being a crude approximation, leads to an increase of uncertainties during simulation.

$$\delta = 0.50\left(sin\left(\frac{\pi G}{l_F}\right) + 1.0\right) \tag{3-41}$$

3.1.4.3 Zhichao Model

This is a G-equation model in which the reaction rate is calculated based on a swept-volume algorithm and was developed by Zhichao Tan in 2003 [46]. Reaction rates are calculated in the cells containing the mean flame front, as shown in Figure 3-9, and specifically, in the volume swept by the flame during the time interval [22][46][58] as shown in Eqn. (3-42).

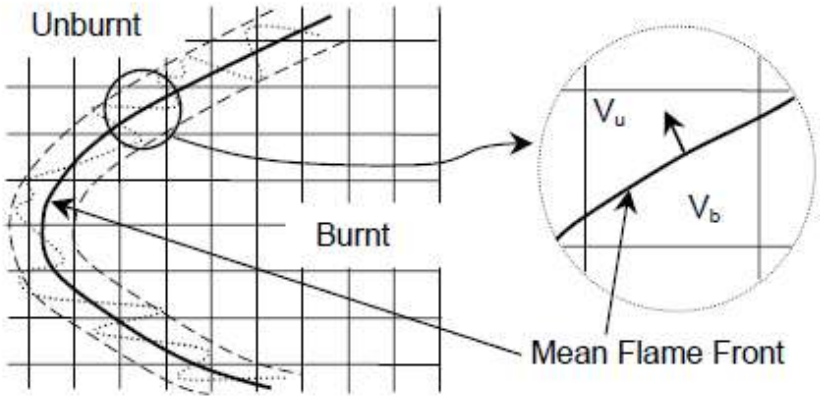

Figure 3-9 Schematic diagram showing the mean flame front [46]

$$\omega_i = \frac{d\rho_i}{dt} = \rho\left(Y_i^u - Y_i^b\right)\frac{s_T A_F}{V_{cell}} \tag{3-42}$$

where Y_i^u and Y_i^b are mass fractions of species, i, in the unburnt and burnt regions, respectively. A_F is the mean flame surface area contained in the cell and V_{cell} is the cell volume with the flame front. Though, the flame swept volume is approximated by the product $s_T A_F$ in this model, which is not accurate and will be explained in the next sub-section.

3.1.4.4 Swept-volume Combustion Algorithm

A new innovative swept-volume approach based on precise sub-volume calculations was developed and is introduced in this sub-section. The sub-volume will be described first, after which the swept-volume combustion model will be presented.

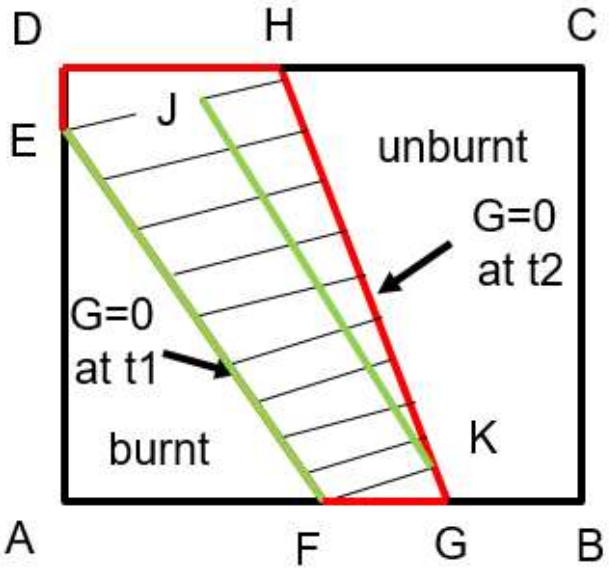

Figure 3-10 Illustration of the inaccuracy of $s_T \Delta t A_F$ for the approximation of true volume swept by the flame

Figure 3-10 shows a 2D cell containing a flame front ($G = 0$ isosurface). In the figure, $G = 0$ isosurface (red line) moves from one location at *t1* to another location at *t2*. Then the cell can be divided into three parts: the burnt region, the swept volume region near the flame, and the unburnt region. Usually the reaction is assumed to occur only in the region swept near the flame and thus usually researchers used $s_T \Delta t A_F$ as an approximation for the swept volume [44][93]. However, this approximation may not be fully accurate under some circumstances. In Figure 3-10, the flame front is represented by line *EF* and *HG* at time *t1* and *t2*, respectively. The volume calculated from $s_T A_F \Delta t$ is the rectangular area *EFKJ*, while the true area by the flame front during this time interval is the area enclosed by *EFGHD*. The reason for this inconsistency is due to the

approximation $s_T A_F \Delta t$ which assumes that s_T and A_F stay constant within one-time step. Thus, in the present work, a more accurate and innovative algorithm is developed to calculate the domain swept by the flame front more accurately. This combustion model is optimized based on the sub-volume calculation, which is a look-up table method for reconstructing isosurface from nodal fields in mesh cells. This approach was developed by Perini [1] and the approach used here is based on his work. Some researchers previously calculated the sub-volume based on intersection points between cell edges and $G = 0$ isosurface. But, they only considered several intersection cases [69][94]. Thus, an algorithm considering all possible intersection cases between the $G = 0$ isosurface and the cell edges is developed in this section.

To easily understand and carry out the algorithm of sub-volume, all mesh cells are assumed to be hexahedrons. The sub-volume calculation in this section is based on [95], which is a look-up table method for reconstructing isosurface from nodal fields in hexahedrons. Other useful links about sub-volume calculation can be found from [1][96][97]. Only the key steps to calculate the sub-volume are listed below.

Step 1: In OpenFOAM, *G* values are stored at cell centers. Thus, one needs to get the value of *G* on each vertex of a cell using interpolation to determine whether the vertex is in the burnt region or the unburnt region. Set the vertex as 0 if it is in the unburnt domain and otherwise as 1. For a hexahedron cell with 8 vertices, each vertex might be in the burnt or unburnt domain. Therefore, $2^8 = 256$ different cases are possible in total of which 23 basic cases are unique and are shown in Figure 3-11. In Figure 3-11, the black dot indicates the *G* value on that vertex is greater than 0 (burnt domain) and the non-black dot indicates the *G* value on the vertex is smaller than 0 (unburnt domain). For a hexahedron with 8 vertices, the binary 0000 0000 to 1111 1111 corresponds to

unique indices from 0 to 255. Of these 256 configurations, 233 cases include rotation, symmetries, and combination of the 23 basic cases.

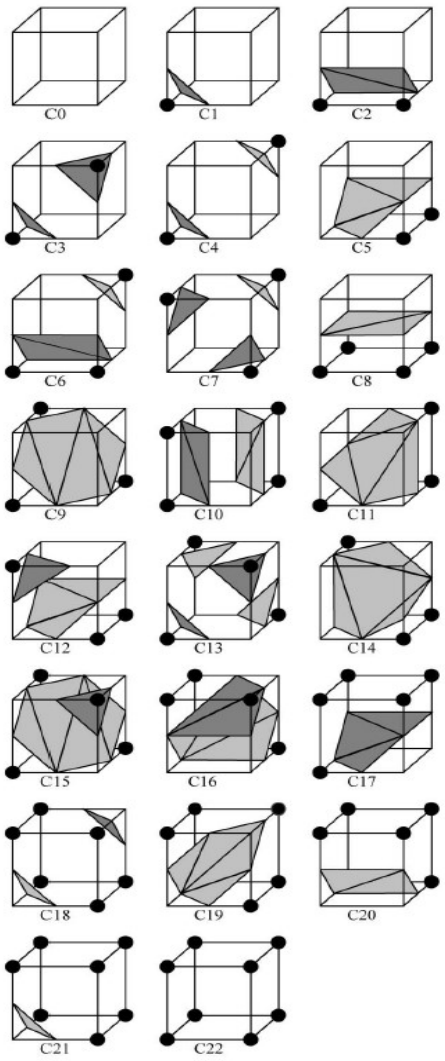

Figure 3-11 Basic cases for sub-volume calculation [95]

The goal is to get the volume swept near the flame ($G = 0$ isosurface) during the Δt ($t2$ - $t1$) period. The burnt sub-volume can be calculated at times $t1$ and $t2$, then the swept volume will be equal to the difference of burnt sub-volume during this time interval. Thus, the key point is to get the burnt sub-volume at each time step.

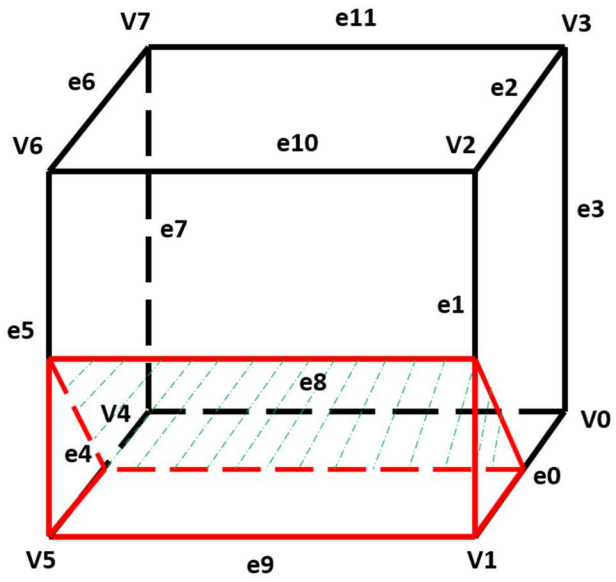

Figure 3-12 Sub-volume (volume enclosed by the red frame) calculation by reconstructing isosurface from nodal fields in mesh cells (v represents the vertex and e represents the edge)

Step 2: When accessing the look-up table according to the cell indices ranging from 0 to 255, triangulate the $G = 0$ isosurface based on the intersection points between $G = 0$ isosurface and cell edges, and reorder those isosurface triangles in order to get the expected normal vectors. In all cases, the normal of an isosurface is set to point towards the $G < 0$ region (unburnt region). This step is to triangulate all the surface enclosing the burnt sub-volume. In Figure 3-12, the right surface of the burnt sub-volume (composed by vertex V1, intersection points on e0 and e1) is already a triangle and triangulation is not required for this surface. On the other hand, the front face of burnt sub-volume is a rectangle, so it needs to be divided into two triangles. After all the burnt sub-volume surfaces are triangulated, the surface normal vector of each triangle surface is set to direct towards the unburnt region ($G < 0$) by renumbering the intersection points based on the right-hand rule.

Step 3: Computing the volume of high value region ($G > 0$) using the Gaussian divergence theorem [1], which can be calculated as:

$$V = \int_{\Omega} dV \tag{3-43}$$

Then the position function $f(x, y, z) = [x\ y\ z]^T$ can be used to calculate the volume:

$$\int_{\Omega} \nabla \cdot f\, dV = \int_{\Omega} \left(\frac{\partial x}{\partial x} + \frac{\partial y}{\partial y} + \frac{\partial z}{\partial z}\right) dV = \int_{\Omega} 3\, dV = 3V \tag{3-44}$$

Thus,

$$V = \frac{1}{3}\int_{\Omega} \nabla \cdot f\, dV = \frac{1}{3}\int_{\partial\Omega} f \cdot \vec{n}\, dS = \frac{1}{3}\sum_{i=1}^{n_{tri}} \int_{\partial\Omega_I} f \cdot \vec{n}\, dS_i = \frac{1}{3}\sum_{i=1}^{n_{tri}} A_i f \cdot \vec{n} \tag{3-45}$$

where *f* is the centroid of the triangle and $\vec{n}$ is the normal vector of all the triangles enclosing the high value ($G > 0$) region.

The methods described above pertain to the burnt sub-volume calculation. Then, the swept volume by the flame equals the difference of burnt sub-volumes during that time interval. Now, the format of reaction rate treatment at the flame front is formulated as below:

$$\frac{d\rho_i}{dt} = \frac{\rho\left(Y_{i,b} - Y_i\right)}{\Delta t}\frac{V_S}{V_u} \tag{3-46}$$

where ρ is the averaged cell density, $Y_{i,b}$ is the equilibrium mass fraction for species i, Y_i is the mass fraction of species i of previous time, V_S is the swept volume by the flame, V_u is the unburnt volume.

The thermodynamic equilibrium species mass fraction $Y_{i,b}$ is calculated using the element potential method [2]. The basic theory of element potential method of determining equilibrium is based on the minimization of Gibbs free energy. Usually, the chemical equilibrium composition is calculated either at fixed pressure and temperature, or at fixed pressure and enthalpy. Constraints can be imposed on individual species, or on arbitrary linear combinations of species. The code solving the above problem is called CEQ (chemical equilibrium solver) proposed by Stephen B. Pope [98] and was written as FORTRAN code. Thus, one needs to ensure compatibility between

FORTRAN code and OpenFOAM, which is based on the C++ language. The interoperability between FORTRAN and C++ can be found from Ref. [99]. However, every component must be of the interoperable type and kind and may not have the pointer or allocable attributes whose names are irrelevant for interoperability. Therefore, Cantera is combined with OpenFOAM in order to use CEQ in OpenFOAM. Cantera [100] is a helpful tool based on C++ to calculate chemical equilibrium components under specific thermal conditions. The verification of the link establishment between OpenFOAM and Cantera is described in Appendix A. The calculation of $Y_{i,b}$ is based on constant pressure and constant enthalpy conditions for this swept volume combustion model.

Other types of cell shapes commonly seen in engine mesh include prism, pyramid, and tetrahedral with 64, 32, 16 possible intersections between flame front and cell edges, respectively. The total intersection cases for hexahedra, prism, pyramid, and tetrahedral are given in Appendix B and these were implemented in the current model.

3.1.5 Reinitialization Scheme

The property $|\nabla G| = 1$ needs to be maintained during the simulation, otherwise it would make it difficult to find the location of $G = 0$ isosurface. However, this property will be disturbed after the calculation of the G transport equation due to some factors, e.g., different local velocities. To illustrate this point in a relatively simple way, the s_T and $D_t$terms are set to zero and the reduced G transport equation is listed as Eqn. (3-24):

Physically, the reduced G transport equation (Eqn. (3-24)) could be interpreted as a series of G contour lines, each moving at its local velocity $\vec{u}$. Nonetheless, the velocity $\vec{u}$ is usually not uniform for most of cases. Figure 3-13 shows two parallel isovalue lines $G\_1 = 0.1$ and $G\_2 = 0$ at two different times. The assumption is that local velocity $u1$ is greater than $u2$ is imposed for

this case. At Time = *t1* (left figure), the *G* field is a distance function that indicates that the distance between these two isovalue lines is 0.1. However, later when Time = *t2*, the absolute distance between these two isovalue lines will be less than 0.1 because *u1* is greater than *u2*. This indicates that the *G* value at Time = *t2* is not a distance function any more. This could result in an incorrect calculation of the G transport equation, and further affects the location of the $G = 0$ isosurface. Since the $G = 0$ isosurface represents the flame front where reaction occurs, reaction rates and heat release could be wrong leading to loss of accuracy of the G-Equation. Thus, a scheme named reinitialization is required to keep *G* as a distance function again after calculation of the *G* transport equation.

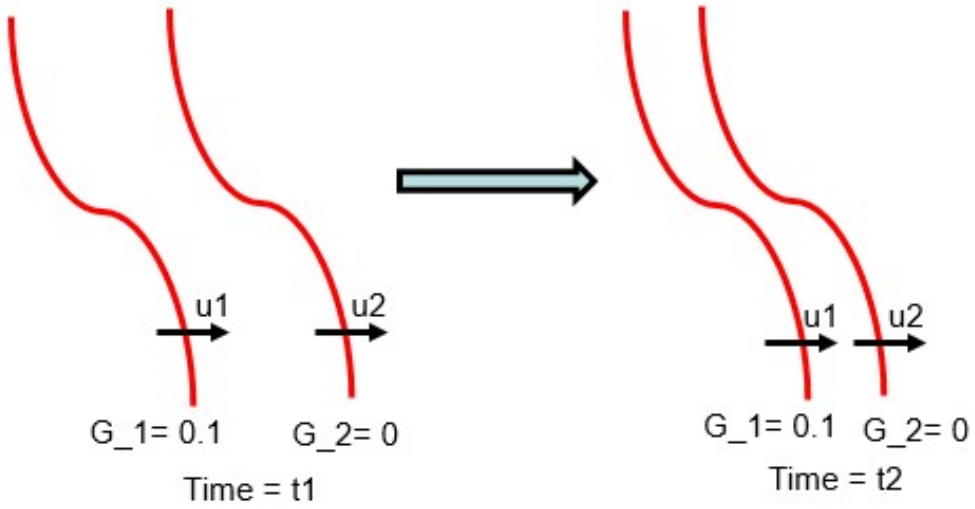

Figure 3-13 isovalue lines at two different time (*u1* > *u2*)

3.1.5.1 Reinitialization Scheme Implementation

The reinitialization scheme is used to reconstruct the signed distance function in the context of level set methods. It has been applied to a number of different circumstances, such as minimal surface [101], free boundary problems in two phase flow [102][103], crystal growth [104], and motion of multiple junctions [105]. This scheme was put forward by Sussman [102], which was developed for computing the motion of incompressible two-phase flow with steep gradients in

density and viscosity existing across the interface. This reinitialization is based on solving the following partial differential equation.

$$\frac{\partial G}{\partial t} = sgn(G^0)(1 - |\nabla G|)$$
$$G^0(x) = G(x, 0) \tag{3-47}$$

The zero level set of G^0 represents the interface location. It can be seen that $|\nabla G| = 1$ when this equation comes to its steady state, which indicates that G becomes a distance function again after reinitialization. The reinitialization scheme was implemented in OpenFOAM. Special treatments for the implementation are listed below:

(1) Reinitialization scheme is not implemented for the cell containing the $G = 0$ isosurface and its adjacent neighbor cells which are on the other side of the $G = 0$ isosurface;

(2) Upwind scheme is applied to calculate the gradient term $|\nabla G|$ for cells which are not included in (1).

However, the reinitialization scheme, as developed by Sussman, has one drawback: the interface could not stay at the fixed location at specific time after the reinitialization iteration because the algorithm is not a truly upwind discretization near the interface. Figure 3-14 shows the signal propagation off the zero level set. The solid arrows represent the unit normal to the zero level set while the dashed arrows stands for the direction of the propagation of the signal. It is obvious that the signal propagation on the zero level interface is "bidirectional." The variable ϕ corresponds to G in the G-Equation reinitialization scheme. Based on this, Russo and Smeraka [3] modified Sussman's reinitialization scheme. They made special treatment for mesh cells within one cell distance between cell centers and the interface ($G = 0$). In this way, the method provides first order accuracy for the signed distance function in the whole computational domain and second order accuracy in the location of the interface. The modified reinitialization scheme is listed below.

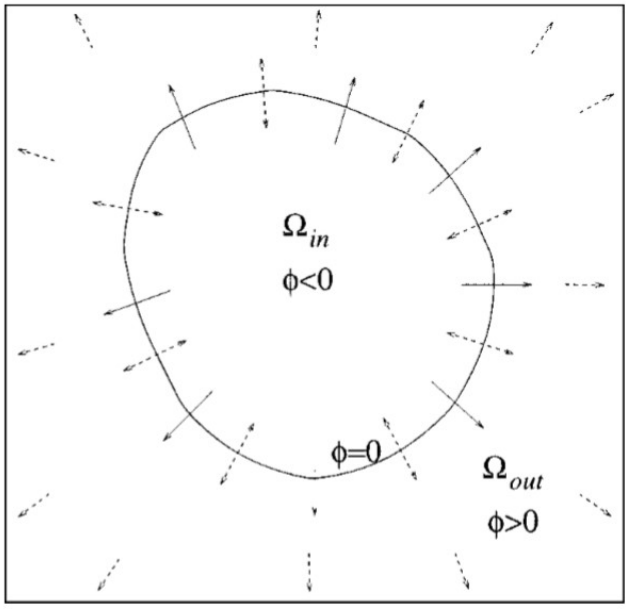

Figure 3-14 Signal propagation off the zero level set. The solid arrows represent the unit normal to the zero level set while the dashed arrows stands for the direction of the propagation of the signal [3].

$$G_i^{n+1} = \begin{cases} G_i^n - \dfrac{\Delta t}{\Delta x}(sgn(G_i^0)|G_i^n| - D_i) & if\ G_i^0 G_{i+1}^0\ or\ G_i^0 G_{i-1}^0 < 0 \\ G_i^n - \Delta t sgn(G_i^0) GRAD(G)_i & otherwise \end{cases} \tag{3-48}$$

where

$$GRAD(G)_i = \begin{cases} \sqrt{max(a_+^2,\ b_-^2) + max(c_+^2,\ d_-^2) + max(e_+^2,\ f_-^2)} - 1 & if\ G_i^0 > 0 \\ \sqrt{max(a_-^2,\ b_+^2) + max(c_-^2,\ d_+^2) + max(e_-^2,\ f_+^2)} - 1 & if\ G_i^0 < 0 \end{cases}$$

$$a = D_x^- \phi_i = \frac{(G_{i,j,k} - G_{i-1,j,k})}{\Delta x} \qquad b = D_x^+ G_i = \frac{(G_{i+1,j,k} - G_{i,j,k})}{\Delta x}$$

$$c = D_y^- \phi_i = \frac{(G_{i,j,k} - G_{i,j-1,k})}{\Delta x} \qquad d = D_y^+ \phi_i = \frac{(G_{i,j+1,k} - G_{i,j,k})}{\Delta x}$$

$$e = D_z^- \phi_i = \frac{(G_{i,j,k} - G_{i,j,k-1})}{\Delta x} \qquad f = D_z^+ \phi_i = \frac{(G_{i,j,k+1} - G_{i,j,k})}{\Delta x}$$

$$D_i = \Delta x \frac{G_i^0}{\Delta G_i^0}$$

$$\Delta G_i^0 = max\left\{\frac{\left|G_{i+1}^0 - G_{i-1}^0\right|}{2}, \left|G_{i+1}^0 - G_i^0\right|, \left|G_i^0 - G_{i-1}^0\right|, \varepsilon\right\}$$

where $\varepsilon = 10^{-8}$. Nevertheless, this reinitialization is based on the assumption of a uniform and orthogonal mesh. In fact, the mesh is non-uniform and non-orthogonal for engine cases. Therefore, a reinitialization scheme that is valid for non-uniform and non-orthogonal meshes needs to be developed, and this scheme will be introduced in this section. By analyzing the reinitialization scheme introduced above, one can see that the key parameters are the six variables *a, b, c, d, e* and *f*, which are related to the location of cell i and its neighbor cells. For uniform and orthogonal meshes, it is easy to determine the neighbor cell location for cell i by comparing the coordinate of cell i and its neighbor cells. However, for non-uniform and non-orthogonal mesh, this rule is not true anymore. Thus, a universal method needs to be found in order to get the right neighbor cells for cell i. The picture below displays the mesh vertices ordering in OpenFOAM.

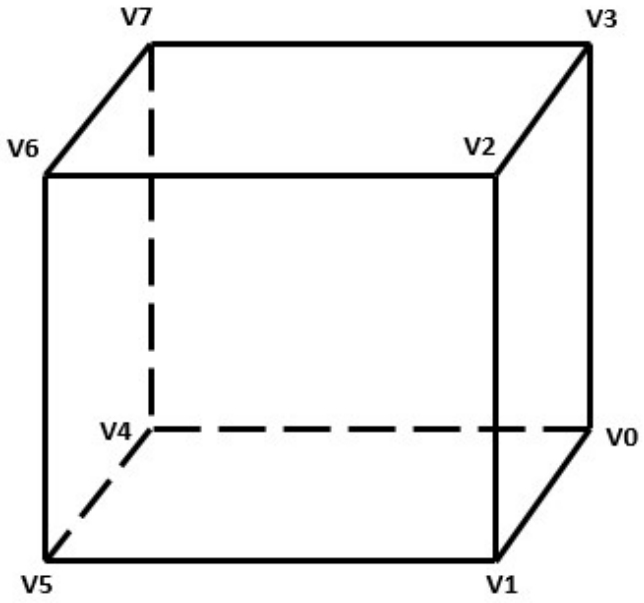

Figure 3-15 vertex ordering in OpenFOAM mesh

To determine the left side neighbor cell for this cell, one can find the neighbor cell that contains vertex 5 and vertex7 (or vertex 4 and vertex 6) in Figure 3-15. Similarly, a neighbor cell

that shares vertex 1 and vertex 3 (or vertex 0 and vertex 2) will be regarded as the right neighbor cell for this cell. For the top, bottom, front and back neighbor cells, the same method is applied. Then the numerator of the above *a, b, c, d, e* and *f* six variables (Eqn. (3-48)) can be replaced by the corresponding *G* values and the denominator can be replaced by the distance between the current cell and its corresponding neighbor cells.

3.1.5.2 Reinitialization Extension to Non-Hexahedra Mesh

Even though the above improved reinitialization scheme could be used for non-uniform and non-orthogonal mesh, it is only valid for hexahedral meshes. To extend the reinitialization scheme to all mesh types, a more universal and robust algorithm for reinitialization is introduced here [106]. The new scheme is named as "efficient direct reinitialization" and its purpose is to find the smallest distance from a certain point to an isosurface ($G = 0$ isosurface in the G-Equation) [106], which is consistent with the goal of the reinitialization scheme. The figure below is an illustration of the efficient direct reinitialization approach.

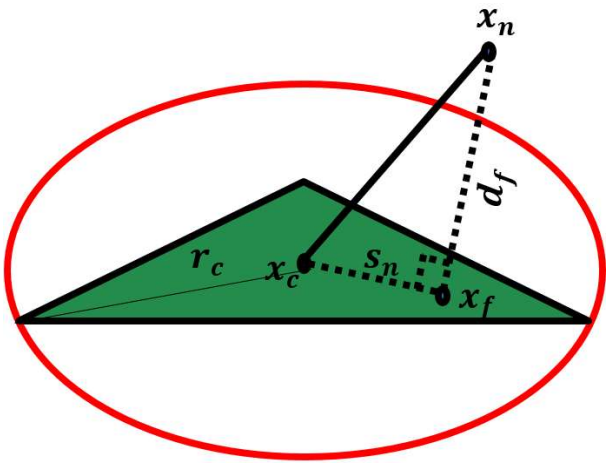

Figure 3-16 Illustration of the efficient direct reinitialization

In the figure above, the green triangle represents one piece of the triangulated $G = 0$ isosurface as described in sub-volume algorithm. x_n is a random space point, x_c is the centroid of the triangle, x_f is the projection point from point x_n to the triangle, d_f is the projection distance between the

point x_n and the triangle surface, s_n is the distance between the centroid x_c and the projection point x_f, and r_c is the largest distance between the centroid x_c and the three triangle vertices which is used as a radius to draw a circle encompassing all triangle vertices. A space point is regarded to have a projection point on the triangle surface if $s_n \leq r_c$. The projection distance d_f is calculated as Eqn. (3-49):

$$d_f = |\vec{n} * (x_n - x_c)| \tag{3-49}$$

where $\vec{n}$ is the normal of triangle surface and s_n can be calculated from the Pythagorean theorem since the distance between x_c and x_n is known. However, since the $G = 0$ isosurface is triangulated, the random point x_n might have projection points on several triangular surface. For instance, Figure 3-17 shows a random point x_n projects onto two surfaces. Under this kind of situations, the smallest projection distance is chosen to reinitialize the G field.

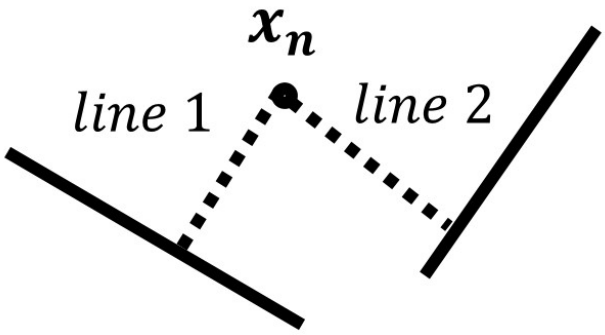

Figure 3-17 Projection of random point x_n to two triangular surfaces (bold lines) with line2 and line2 being the projection distance from x_n to the triangular surfaces

During the reinitialization process, all triangular $G = 0$ surfaces are gathered together. For each cell center point, its projection distance to every triangular surface is calculated. If the projection point x_f of cell center point is inside the circle determined by the radius r_c of that triangular surface vertices, the absolute value of G at that cell equals the corresponding projection distance—positive in the burnt region and negative in the unburnt region. If the cell center point

has projection points on several triangular surfaces, the smallest projection distance is chosen to reinitialize the *G* fields.

3.2 Ignition Model Development

The model developed in the current research is named the WSSIM model since it accounts for the effect of turbulence on wrinkling and stretching the kernel surface. Basically, the WSSIM includes four parts, namely the electric circuit model, the kernel growth model, the plasma channel model, and the restrike model, as shown in Figure 3-18. In the following sections, these four sub-models are described.

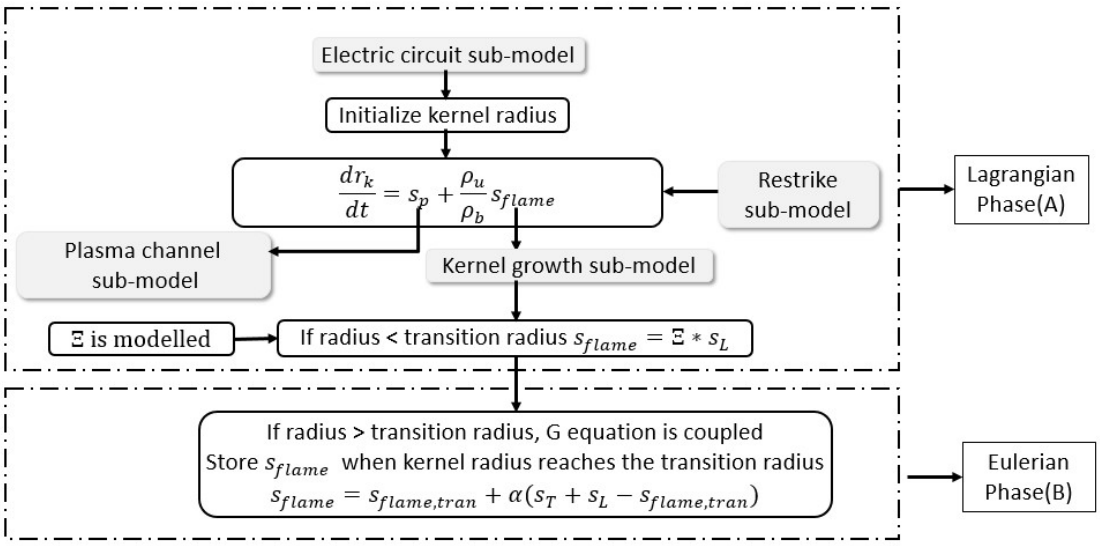

Figure 3-18 Flow chart of WSSIM (Wrinkling and Stretch Spark Ignition Model) including the electric circuit model, the plasma channel model, the kernel growth model, and the restrike model

Figure 3-18 displays the flow chart of WSSIM. The energy from the secondary coil of the ignition system is modeled by the electrical circuitry. It must be reminded here that the electric energy transfer to the gas phase is explicitly modeled in the current approach. The effect of electric energy appears as plasma speed (s_p), and the energy does increase the local temperature directly. Kernel growth modeling begins with the Lagrangian phase, where the flame kernel is modeled by

a spherical particle with a 1mm initial radius. The growth of the spherical particle is modeled by a simple ODE, which considers the plasma velocity, the laminar flame, and the wrinkling of the flame surface. Once the particle grows large enough to be resolved at the grid level, the G-Equation is initialized and used to track the flame growth and evolution of flame speed into a fully developed turbulent flame. The evolution is modeled by a hyperbolic tangent. Meanwhile, a restrike model is employed to predict if a restrike event might occur based on the distance between the kernel new location due to flow convection and the original location of the kernel where its radius is initialized.

3.2.1 Electric Circuit Sub-Model

In general, the inductive systems are composed of a primary and a secondary circuit. These are installed on the spark ignition engines as shown in Figure 3-19. In the WSSIM, only the secondary circuit is simulated.

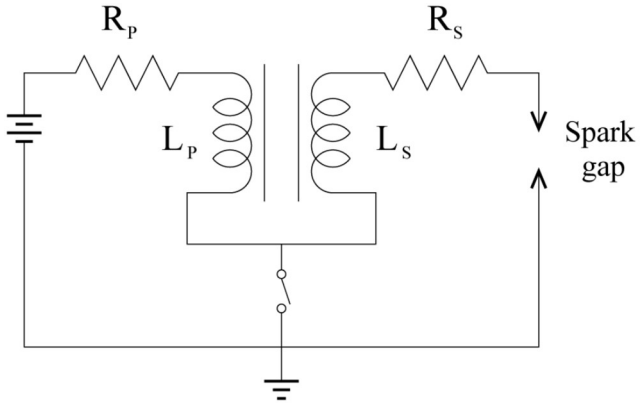

Figure 3-19 Schematic of primary and secondary circuits [24]

The electric circuitry of the secondary coil in a conventional spark ignition device is modeled to calculate how much electric energy is provided to the spark plug, similar to the ATKIM model and its variants [47]. The total energy is an input in the electric circuit sub-model. The energy

transferred from the electrical circuit to the gas phase is expressed as the product of instantaneous voltage and current. The breakdown energy is defined as follows:

$$E_{bd} = \frac{V_{bd}^2}{C_{bd}^2 d_g} \tag{3-50}$$

where C_{bd} is a constant ranging from 150 to 250 $\mathrm{kV/(J-mm)^{0.5}}$ [24][67], the spark gap d_g is in mm, and the breakdown voltage V_{bd} is calculated based on Paschen's law [34] to account for the effects of temperature as given in Eqn. (3-51).

$$V_{bd} = 4.3 + 136\left(\frac{P}{T}\right) + 324\left(\frac{P}{T}\right) d_g \tag{3-51}$$

Here *P* is the pressure in bars and T is the gas temperature in K.

The temperature and radius of the kernel are initialized based on the correlation provided by Refael [37] with the breakdown temperature T_{bd} = 60,000K.

$$T_{ikernel} = \left(\frac{1}{\gamma}\left(\frac{T_{bd}}{T_0} - 1\right) + 1\right) T_0 \tag{3-52}$$

$$r_{ikernel} = \left(\frac{\gamma - 1}{\gamma} \frac{E_{bd}}{P_0 \pi d_g (1 - T_0/T_{ikernel})}\right)^{0.5} \tag{3-53}$$

where T_0 is the average temperature, and γ is the heat capacity ratio and is set to be 1.4. The voltage during the ignition between the spark plug gaps is calculated by the relation:

$$V_{ie} = V_{cf} + V_{af} + V_{gc} \tag{3-54}$$

where V_{cf} and V_{af} are the cathode and anode voltage drop given in [107]. V_{gc} is the voltage along the spark patch and is calculated as:

$$V_{gc} = 40.46 l_{spk} i_s^{-0.32} p^{0.51} \tag{3-55}$$

The term i_s is the current in the secondary circuit and is given by the relation:

$$i_s = \sqrt{\frac{2E_s}{L_S}} \tag{3-56}$$

The electrical energy on the secondary circuit E_s is given by:

$$\frac{dE_s(t)}{dt} = -R_s i_s^2(t) - V_{ie} i_s(t) \tag{3-57}$$

The initial value of E_s is set as the same constant value as is in experiments. The term l_{spk} in Eqn. (3-55) is the spark length, which changes during the simulation due the flow convection. The spark length l_{spk} is sometimes described by a set of quasi-spherical marker particles, as shown in Figure 3-20 (a) [24][47]. In this study, however, only one flame marker particle is used, and it is convected by the gas flow. Note that this marker particle likewise serves as the flame kernel marker. Thus, an equivalent spark length is calculated as the sum of L1 and L2, which are the distance among cathode, anode, and the kernel center, as shown in Figure 3-20 (b). Also, it should be mentioned that the energy is directly deposited to gas, and the calculated energy provides information to model initial plasma propagation via a plasma flame speed, as explained in the next section.

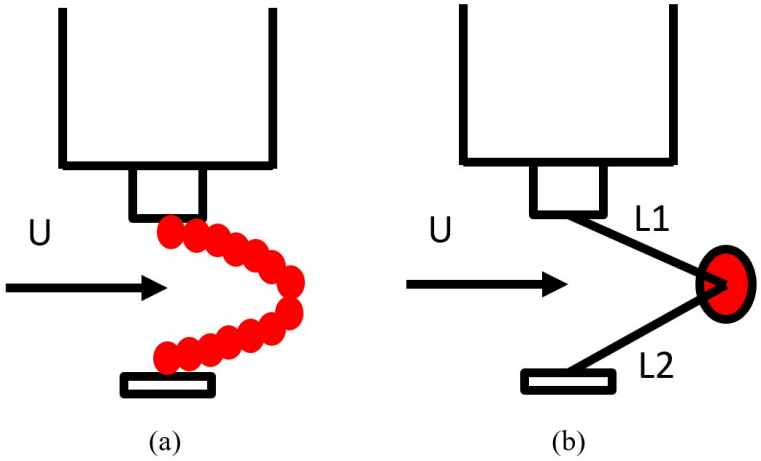

Figure 3-20 Spark length calculation in the electric circuit model. In (a), the spark length is represented by a set of Lagrangian particles. In (b), only one flame kernel is initialized, an equivalent spark length is calculated as the sum of L1 and L2

3.2.2 Kernel Growth Sub-Model

In the kernel growth sub-model, the growth rate of the spherical ignition kernel is determined by two phenomenon: the thermal expansion due to the plasma (s_p) and the turbulent flame propagation speed (s_{flame}) [24][67].

$$\frac{dr_k}{dt} = s_p + \frac{\rho_u}{\rho_b} s_{flame} \tag{3-58}$$

where ρ_u and ρ_b are the unburnt and burnt gas densities, respectively.

The plasma velocity s_p is described in the next section. The calculation of the flame propagation speed s_{flame} for the ignition kernel is divided into two phases displayed in Figure 3-21:

- Phase (a): region near laminar flame speed.
- Phase (b): transition region from near laminar flame speed to fully turbulent flame propagation speed.

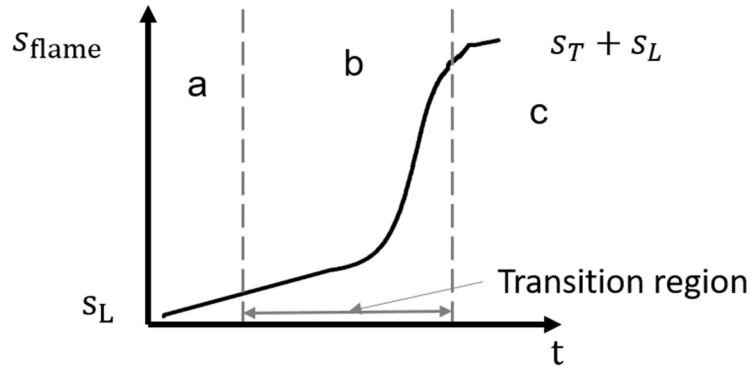

Figure 3-21 Flame speed s_{flame} evolution during the ignition process (the WSSIM includes Phase (a) and Phase (b))

Phase (a) is a near flame speed region where the flame kernel radius is small. In this region, the turbulence is not able to affect the inner flame structure but can wrinkle the flame surface which locally remains close to the laminar flame. Phase (b) is the transition region from nearly laminar flame speed to a fully turbulent flame propagation speed [108]. Separate modeling approaches have been applied to model two phases.

3.2.2.1 Kernel Growth Sub-Model: Phase (a)

Phase (a), which represents the initial development of flame kernel, is typically at a very small scale and requires a very fine mesh. To avoid the additional computational overhead, phase (a) is modeled by a Lagrangian particle which is allowed to convect as well as grow. The convection of the particle provides channel length information described in the electric circuitry model.

The flame surface is wrinkled by local flow and turbulence during phase (a), which occurs at sub-grid level and requires modeling. The effect of flame wrinkling on flame speed is modeled by a wrinkling factor as following [48][84][109]:

$$s_{flame} = \Xi * s_L \tag{3-59}$$

The Gülder correlation is employed to calculate the laminar burning velocity s_L. The term Ξ is the wrinkling factor. Initially its value is unity, representing that the flame initially travels at laminar flame speed. Temporal evolution of the wrinkling factor is modeled by the following equation [48]:

$$\frac{d\Xi}{dt} = \langle a_t \rangle_s \left\langle \frac{\Xi_{eq} - \Xi}{\Xi_{eq} - 1} \right\rangle_s \Xi \tag{3-60}$$

Here $\langle a_t \rangle_s$ represents the ability of all vortices to wrinkle the flame and Ξ_{eq} is the equilibrium wrinkling factor given by Colin [49]. The symbol $\langle \cdots \rangle_s$ indicates the average over the flame kernel surface. The variable a_t is given as [109]:

$$a_t = \Gamma_k \left(\frac{\widehat{u'}}{s_L}, \frac{\hat{\Delta}}{\delta_L} \right) \frac{\widehat{u'}}{\hat{\Delta}} = 0.75 exp \left[- \frac{1.2}{\left(\hat{\Delta}/\delta_L \right)^{0.3}} \right] \left(\frac{\widehat{u'}}{s_L} \right)^{2/3} \frac{\widehat{u'}}{\hat{\Delta}} \tag{3-61}$$

where $\widehat{u'}$ is the turbulent velocity fluctuation at scale $\hat{\Delta}$. Initially $\widehat{u'}$ is estimated from the sub-grid turbulence intensity based on the Kolmogorov cascade $\widehat{u'} = u' \left(\hat{\Delta}/\Delta \right)^{1/3}$ and $u' = \nu_t/(C\Delta)$ with

C = 0.12. The equilibrium wrinkling factor Ξ_{eq} is given in the Ref. [109], which is reproduced below:

$$\Xi_{eq} = 1 + \frac{2}{s_L}\sqrt{\frac{\widehat{v_t}a_t}{1 - \frac{\beta c^*}{1+\tau}}} \tag{3-62}$$

where $\widehat{v_t} = C\widehat{u'}\hat{\Delta}$. β = 4/3 and c^* = 0.5 are modelling constants. Moreover, $\tau = \rho_u/\rho_b - 1$ is the thermal expansion rate across the flame front.

3.2.2.2 Kernel Growth Sub-Model: Phase (b)

Phase (b) begins when the kernel radius reaches the transition radius, which is 1 mm as suggested in [108]. Once the kernel grows to the transition radius, it is assumed that the size of the initial kernel is large enough to be resolved by the grid. As such, the growth is modeled by the Eulerian model where the kernel surface begins to be represented by the G = 0 isosurface rather than the Lagrangian particle. In this region, the turbulence exerts a more significant effect on the flame wrinkling and propagation, whereas the flame propagation speed is still smaller than the fully turbulent flame propagation speed. The G-Equation is turned on, while the flame speed is modified from the original G-Equation to model the transition into the fully developed turbulent flame speed. Details of G-Equation implementation will be reviewed in the combustion model description. The flame propagation speed during the transition process is calculated as:

$$s_{flame} = s_{flame,tran} + \alpha\left(s_T + s_L - s_{flame,tran}\right) \tag{3-63}$$

where $s_{flame,tran}$ shown in Figure 3-21 is the flame propagation speed at the transition point between regions (a) and (b), s_T is the fully turbulent burning velocity given in Eqn. (3-31), and s_L is the laminar burning velocity. The laminar burning velocity s_L is based on the Gülder correlation (Eqn. (3-27)) and the fully turbulent burning velocity s_T is given as Eqn. (3-31).

The transition function α in Eqn. (3-69) varies from zero to one and is used to smoothly transition from the laminar region to the fully turbulent regime. It is given by [49]:

$$\alpha = 0.5\left(1 + tanh\left(\left(\frac{r_k}{\hat{\Delta}} - 0.75\right)/0.15\right)\right) \tag{3-64}$$

with r_k is the equivalent radius of the flame kernel calculated from the flame surface area, $\hat{\Delta}= n_{user}\Delta$ where n_{user} is a user defined constant, and Δ is the LES filter width equal to the local gird cell size. Figure 3-22 shows the relationship between the transition function value and r_k under the setting $\hat{\Delta}= 2$. It can be seen that the α value is near zero when r_k is small and becomes 1 once r_k is greater than 2.0.

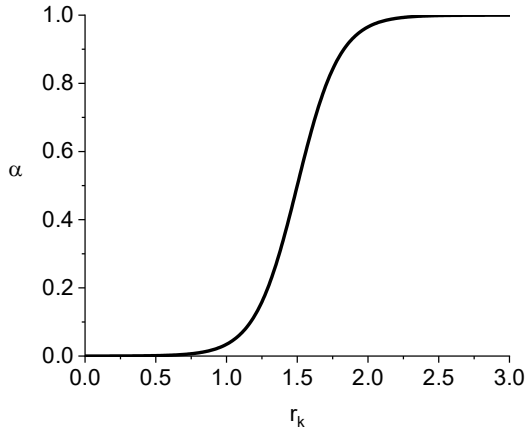

Figure 3-22 Relationship between transition function value and r_k ($\hat{\Delta}$ is set to be 2.0)

3.2.3 Plasma Channel Sub-Model

The plasma velocity, s_p in Eqn.(3-58), represents the flame expansion due to energy transfer from the electrical circuit. The arc phase and glow phase are simulated in the plasma channel sub-model. There are two different mechanisms corresponding the above phases that govern the plasma velocity, and distinguishing between these mechanism is necessary. The first mechanism corresponding to the arc phase is heat conduction dominant, which occurs from the hot plasma

channel to the unburnt mixture when the temperature inside the flame kernel is not uniformly distributed. The second mechanism corresponding to the glow phase is the expansion, as due to chemical reactions and heat transfer from the electrical circuit, under which the temperature distribution inside the flame kernel can be considered uniform. A temperature threshold was used, as suggested by Bianchi and Lucchini [24], to differentiate these two mechanisms: if the mean kernel temperature is greater than three times the adiabatic flame temperature T_{ad}, the kernel is considered to have a non-uniform temperature distribution.

For arc phase, when the plasma kernel temperature $T_p > 3T_{ad}$, the conduction effects cannot be neglected. The temperature distribution within the kernel is computed by solving a 1-D heat conduction equation. Then, the temperature and corresponding plasma velocity are given as follows [24]:

$$\frac{\partial T_p}{\partial t} = \alpha_t \left(\frac{\partial^2 T_p}{\partial r^2} + \frac{2}{r} \frac{\partial T_p}{\partial r} \right) + \frac{3\eta V_{ie}(t) i_s(t)}{4 c_p \rho \pi r_p^3} \tag{3-65}$$

$$s_p = \frac{d}{dt} \left(r_p \left(1 + \frac{LHV}{c_p T_{ad}} \right)^{1/3} \right) \tag{3-66}$$

where α_t is the thermal diffusivity, LHV is the lower heating value of the fuel, c_p is the specific heat capacity, r_p is the plasma radius determined based on corresponding adiabatic temperature, and T_{ad} is the adiabatic temperature.

The Eqn. (3-65) is solved on an axis-symmetric grid that represented the gas surrounding the plasma. The domain size is set to be 1 cm and the grid size was set to 10 μm and sub-cycled at around 1 ns in order to achieve numerical stability. The plasma temperature is initialized as suggested by [19] and listed below:

$$\begin{aligned} T_p &= T_{ikernel} \quad if \;\; r_k < r_{ikernel} \\ T_p &= T_{unburnt} \quad if \;\; r_k > r_{ikernel} \end{aligned} \tag{3-67}$$

For glow phase, when the mean temperature of the plasma goes below three times the adiabatic temperature, a uniform temperature is assumed and the plasma velocity is calculated as [19]:

$$s_p = \frac{\eta V_{ie}(t) i_s(t)}{4\pi {r_k}^2 \rho_u (h_b - h_{ub})} \sqrt[3]{1 + \frac{LHV}{c_p T_{ad}}} \tag{3-68}$$

where r_k is the kernel radius, h_b is the burnt enthalpy, h_{ub} is the unburnt enthalpy, and η is the efficiency accounting for the energy transfer between the electrical circuit and the gas phase, and the flow field influences on the energy transfer efficiency. A curve fit for efficiency was proposed by Herweg and Maly [19], as below:

$$\eta = \eta_0 + \frac{(\eta_\infty - \eta_0) U^3}{A + U^3} \tag{3-69}$$

where U is the main flow velocity, η_0 is the energy transfer efficiency for a quiescent mixture, and η_∞ is the energy transfer efficiency for very high flow velocity >> 15 m/s. Table 3-1 provides values of η_0, η_∞ , and A for arc and glow discharge. The transition from the arc to glow phase is based on the mean plasma kernel temperature. The arc phase occurs when $T_p > 3T_{ad}$, otherwise the glow phase is assumed.

Table 3-1 Constants for energy transfer efficiency calculations during arc and glow discharge phases [19]

Parameter	Arc Discharge	Glow
η_0 (%)	36	8
η_∞ (%)	50	30
A $(m/s)^3$	500	700

3.2.4 Restrike Sub-Model

The plasma channel length increases due to the interaction with the plasma channel, thus leading to the increase of the voltage across the gas column. A breakdown event, which is viewed

as a restrike event, occurs when this voltage is high enough. In this model, the spherical ignition kernel convects with the flow as described by the equation below, following [34]:

$$\frac{d\vec{x}}{dt} = \vec{U} \tag{3-70}$$

where $\vec{U}$ is the mean velocity of cells in the kernel and $\vec{x}$ is the location of the center of the kernel. Convection of the kernel with the flow is tracked based on the location of the kernel center during the whole ignition process. If the ignition kernel is displaced more than 5 mm from the initial location during the ignition process, then a restrike event is assumed to take place and a new spherical kernel is initialized at the spark ignition location. The old kernel is no longer traced.

3.2.5 Summary

The above four sub-models compose the WSSIM. Table 3-2 shows the comparison for some popular ignition models with their related applications and phases.

Table 3-2 List of commonly used ignition models and related sub-models (the check symbol indicates that the sub-model is included in that ignition model)

	Energy Deposit	DPIK	AKTIM	AKTIM Euler	ISSIM	Spark CIMM	WSSIM	Phase
Kernel growth		√	√	√	√	√	√	Eulerian
Plasma channel		√	√	√	√	√	√	Lagrangian
Restrike			√	√	√	√	√	Lagrangian
Electric Circuit			√	√	√	√	√	Lagrangian
Turbulence model	RANS LES	RANS	RANS	LES	LES	RANS	LES	

Table 3-3 displays the corresponding G-Equation and burning velocity formulas for RANS and LES. Note, in LES, the variable s_{flame} is calculated according to Eqn. (3-58) and Eqn. (3-63)

which are based on the transition radius and the smooth transition function α, respectively. s_{flame} becomes the sum of s_T and s_L when the transition function $\alpha = 1$.

Table 3-3 G-Equation and burning velocities formulas for RANS and LES

	G-Equation	s_{flame}	s_T	s_L
RANS	Eqn. (3-21)	None	Eqn. (3-29)	Eqn. (3-27)
LES	Eqn. (3-22)	Eqn. (3-58), (3-63)	Eqn. (3-31)	Eqn. (3-27)

Chapter 4 Model Validation

In this chapter, model validation is presented and is divided into four sections: the swept-volume method validation, the reinitialization validation, the ignition validation, and the TCC3 engine validation.

4.1 Swept-Volume Method Validation

To test and validate the sub-volume calculation, the algorithm described in Section 3.1.4.4 is first validated by a 3D ellipsoid and two intersected spheres. Then, the combination of this swept-volume algorithm and RANS version ignition model developed by [34] will be applied to constant volume vessel.

4.1.1 3D Ellipsoid and Two Intersected Spheres

Since the sub-volume calculation methods described in Chapter 3 are used to calculate the burnt sub-volume, it is a suitable approach to calculate the total burnt sub-volume where G is greater than zero to check the accuracy of the sub-volume algorithm.

The first case is a volume enclosed by a 3D ellipsoid surface as is shown in the Figure 4-1.The size of the domain is 100 mm * 100 mm * 100 mm in x, y, and z directions and all cells are cubic with each side 1 mm. The G value was initialized as a distance function and set to be greater than 0 inside the ellipsoid, less than zero outside the ellipsoid, and zero on the ellipsoid surface. To make the intersection between cell edges and $G = 0$ isosurface more complex, an angle of 30 degrees was set between the ellipsoid axis and the horizontal line as shown in the figure. The lengths of ellipsoid axis are $a = 40$ mm, $b = 30$ mm, and $c = 20$ mm where the axis c points inside the figure.

The second test case is a volume enclosed by two-intersected spheres as is seen in Figure 4-2. The domain size is 100 mm * 100 mm * 100 mm in x, y and z directions and all cells are cubic with each side 1 mm. The variable G was set as a distance field with values greater than 0 inside the two-intersected spheres, less than zero outside the two-intersected spheres and zero on the surface. The intersections between these two intersected spheres are complex, especially at the interface of those two spheres. To calculate the volume inside the two-intersected spheres, one needs to calculate the volume of one spherical cap and then double it. Figure 4-2 (a) from [110] shows the volume calculation of a spherical cap and the parameters a = 13 mm h = 5 mm and R = 20 mm in the test case Figure 4-2 (b).

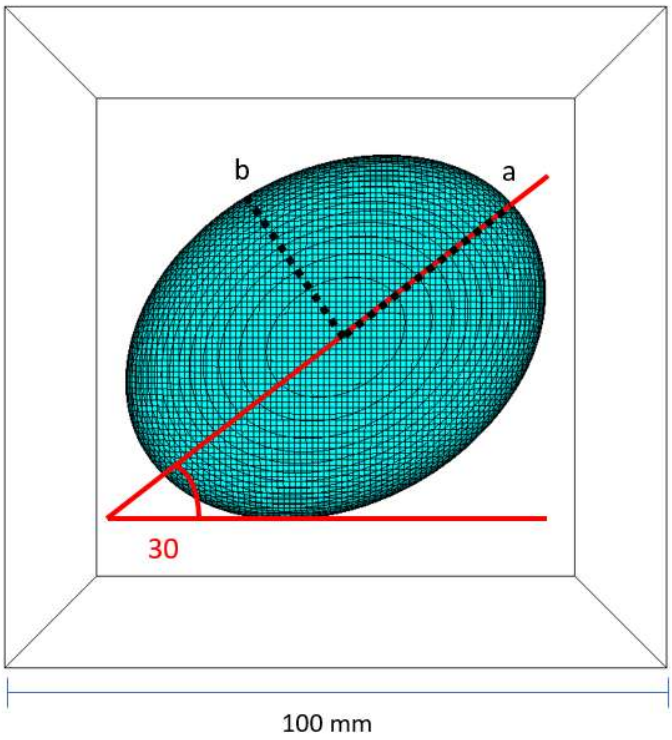

Figure 4-1 Sub-volume algorithm verification for a 3D ellipsoid with a 30 degree between the axis a and the horizontal line (a = 40 mm, b = 30 mm and c = 20 mm in x, y and z directions where the axis c points inside the picture.)

Results of the theoretical and calculated volumes, and the related errors for the two test cases are listed in Table 4-1. The basic reference case with mesh cell size 3 mm is also displayed in the

table. It can be seen from the table that the calculated volume is close to the theoretical volume values with an error less than 0.3% and can be further reduced with finer mesh resolution, thus indicating the algorithm for the calculation of sub-volume is accurate. Therefore, the volume swept by the flame during two successive time steps can be achieved from the difference of the burnt sub-volume between two time intervals.

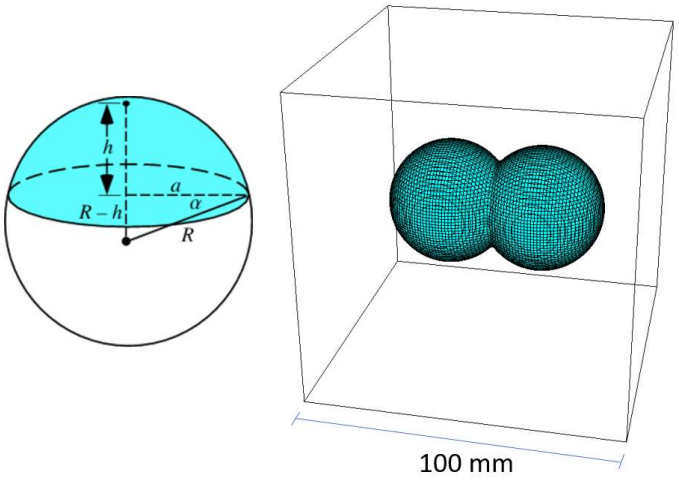

Figure 4-2 Sub-volume algorithm verification for two-intersected spheres (a = 13 mm, h = 5 mm and R = 20 mm in the test case)

Table 4-1 Burnt volume calculations based on sub-volume algorithm and calculated error comparisons between theoretical and calculated results

Case	Theoretical Volume (mm^3)	Calculated Volume for 1mm cell (mm^3)	Error (%) using 3 mm cells	Error (%) using 1 mm cells
3D ellipsoid	1.005e5	1.003e5	4.78	0.26
Two-intersected spheres	6.061e4	6.046e4	4.67	0.24

4.1.2 Constant Volume Vessel Validation

In this section, both the Xiaofeng's model (GM-model, Section 3.1.4.2) and the swept-volume algorithm introduced in Chapter 3's Section 3.1.4.4 are validated using constant volume vessel results based on RANS simulations. In the validation, the flame radius and turbulent burning

velocity comparisons between simulation and experiments [111] are implemented. In the experiments, a constant spherical vessel with a volume of 30 liters (radius = 192.8 mm) was employed. An initial methane and air mixture with charge temperature of 360 K was adopted in all experiments. The flames were imaged using schlieren photography, employing a 20 W tungsten element lamp. By subtracting the background from the image and applying threshold, a binary image was produced for each frame where the burned area was white, and the remainder was black. Flame areas were then measured by counting the number of pixels behind the flame front and the flame radii were computed as those of a circle of area equal to that of the imaged flame. Moreover, the turbulent burning velocity was calculated as

$$s_{T\_exp} = \left(\frac{1}{1.11}\frac{\rho_b}{\rho_u}\right)\frac{dr}{dt} \tag{4-1}$$

where $\frac{dr}{dt}$ is the flame propagation speed, and ρ_b and ρ_u are the burned and unburnt mixture densities, respectively. The turbulent burning velocity was measured when r = 30 mm and the same calculation was applied for turbulent burning velocity calculation from simulation during post-processing. More details about the experiments could be found in [111].

For simulation, it is stronger to use a cubic volume with each edge equal to the diameter of the constant spherical vessel. However, if one sets mesh size as 1 mm and 2mm, it will lead to a domain with mesh cell numbers about 56.6 million and 7.2 million, respectively, which makes the simulation awfully expensive. On the other side, if a smaller cubic domain was established to validate both models, it might result in inaccurate results when the flame propagates to the wall because the wall will cause modifications to the flow field close to the wall and to the turbulent burning velocity calculations [112]. Thus, a 2D circle domain with a radius 192.8 mm was used in order to simplify the calculation. The simulation domain is shown in Figure 4-3. The minimum mesh size is 1*1*1 mm in the square domain for the coarse mesh and 0.6*0.6*0.6* mm for the

finer mesh. The initial integral length scale was set to be 20 mm for all cases as described in the paper.

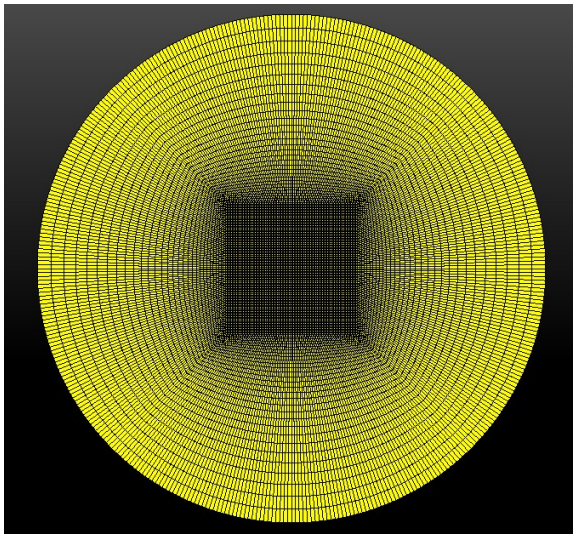

Figure 4-3 2D simulation domain for model validation

In the test, the Müller and Gülder correlations are applied to the GM and the swept-volume combustion models, respectively. The wall temperature is set to 360 K for all cases. Initial temperature and pressure are set 360 K and 1 atm, respectively. Other initial conditions are listed in Table 4-2.

Table 4-2 Initial condition for case tests

Case	Initial u' (m/s)	Equivalence ratio
Case1	2	0.9
Case 2	8e-2	1.0
Case 3	0.5	1.0
Case 4	1	1.0
Case 5	2	1.0
Case 6	4	1.0
Case 7	6	1.0
Case 8	8	1.0
Case 9	10	1.0

Figure 4-4 (case 1) compares the flame radius growth among swept-volume model, GM model and experimental data for phi = 0.9 and u' = 2 m/s. The ignition model developed by Krishna [34]

was used in this simulation. In this model, the transition from ignition to combustion occurred at about 6.7 ms. The sub-volume algorithm developed in Chapter 3 was applied to calculate the radius of flame kernel based on the same method as experiments. It can be seen from the figure that the swept-volume model gives a more accurate flame kernel radius prediction than the GM model. The predicted radius matches very well until 8.8 ms and then is relatively larger than experimental data. This result could be attributed to the u' value in the simulation. For experiments, u' is kept almost constant at 2 m/s while in the simulation the mean u' value changes from 2 m/s to 3.16 m/s for the time ranging from start of ignition to 10 ms due to the kernel growth.

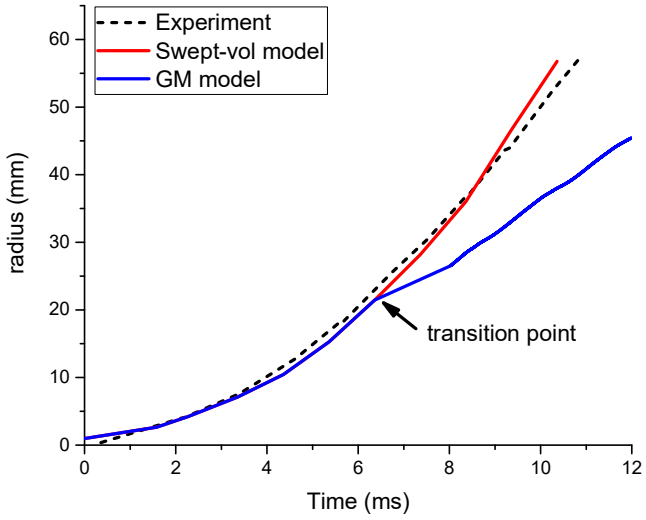

Figure 4-4 Flame radius comparison between simulation and experiments (phi = 0.9, u' = 2 m/s)

The GM model gives a much smaller flame kernel radius prediction because the Müller laminar burning velocity correlation gives a smaller s_L value in comparison to the Gülder laminar burning velocity correlation, see Figure 4-5. This further reduces the turbulent burning velocity and flame propagation. Figure 4-6 (case 2-9) displays the turbulent burning velocity comparison among the swept-volume model, the GM model, and the experimental data. In general, the turbulent burning velocity s_T from simulations shows a similar trend as experimental data. As

indicated in the figure, s_T, for both experiments and simulation decreases to laminar flame speed which is about 0.8 m/s as u' approaches zero. s_T increases with the increase of u' under a certain range. However, as u' exceeds a certain range (about 8.0 m/s in the plot), the growth rate of s_T of simulation and experiments decreases and tends to be almost a constant value. In addition, the swept-volume combustion model shows a more efficient turbulent burning velocity trend than that of the GM model.

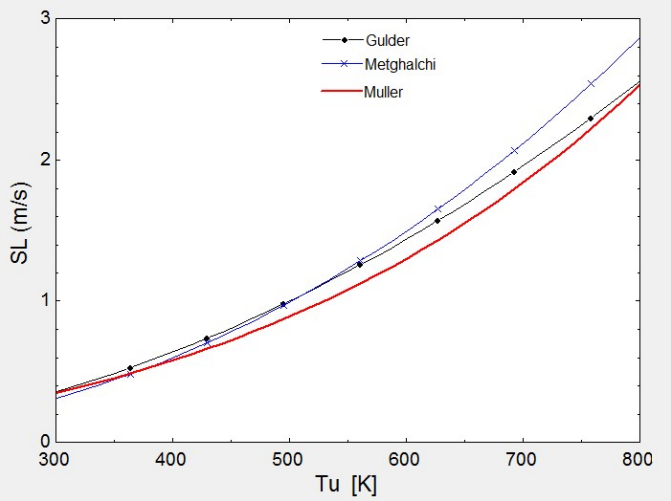

(a)

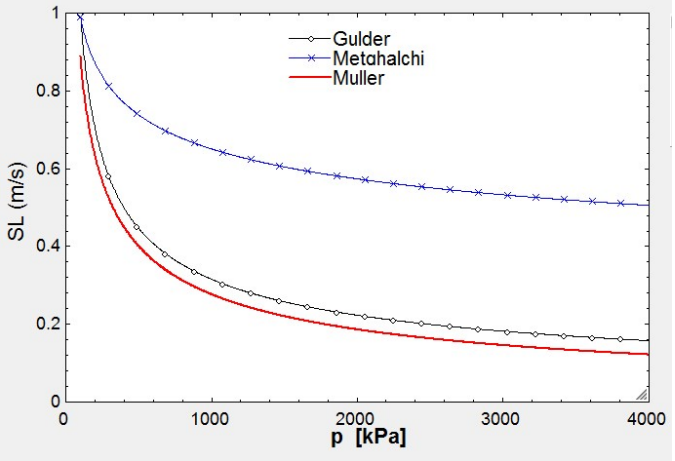

(b)

Figure 4-5 Comparison of laminar burning velocity correlations for methane ((a) phi = 1.0, p= 1 atm; (b) phi = 1.0, Tu = 300 K)

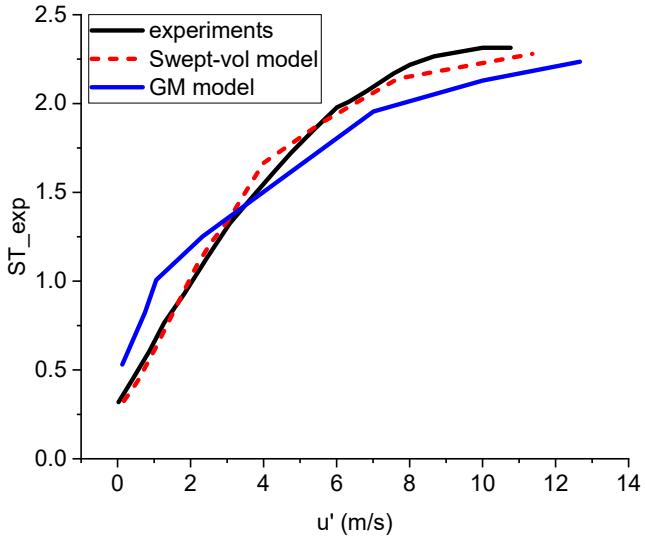

Figure 4-6 turbulent burning velocity Eqn. (4-1) comparison between simulation and experiments (phi = 1.0)

4.2 Reinitialization Validation

In this section, the reinitialization scheme developed in Chapter 3 is validated through both serial computation and parallel computation. The reinitialization on the hexahedral mesh is first validated followed by the non-hexahedral mesh.

4.2.1 Reinitialization Validation for Hexahedral Mesh

In this section, the reinitialization scheme validation is based on [3] as described in section 3.1.5.1. Figure 4-7 shows the initial *G* value on the red line of the TCC3 engine with bore 92 mm and stroke 86 mm. The smallest and largest cell sizes are 0.21*0.54* 0.50 mm and 1.68*1.23*1.50 mm in x, y, and z directions, respectively. The boundary cell size is 1*1*0.5 mm in three directions. Initially, a $G = 0$ sphere with a diameter of 20 mm was defined. *G* was set at a uniform value of 1 inside the sphere and -1 outside the sphere. In this case, 1 CPU was used to test the new reinitialization scheme.

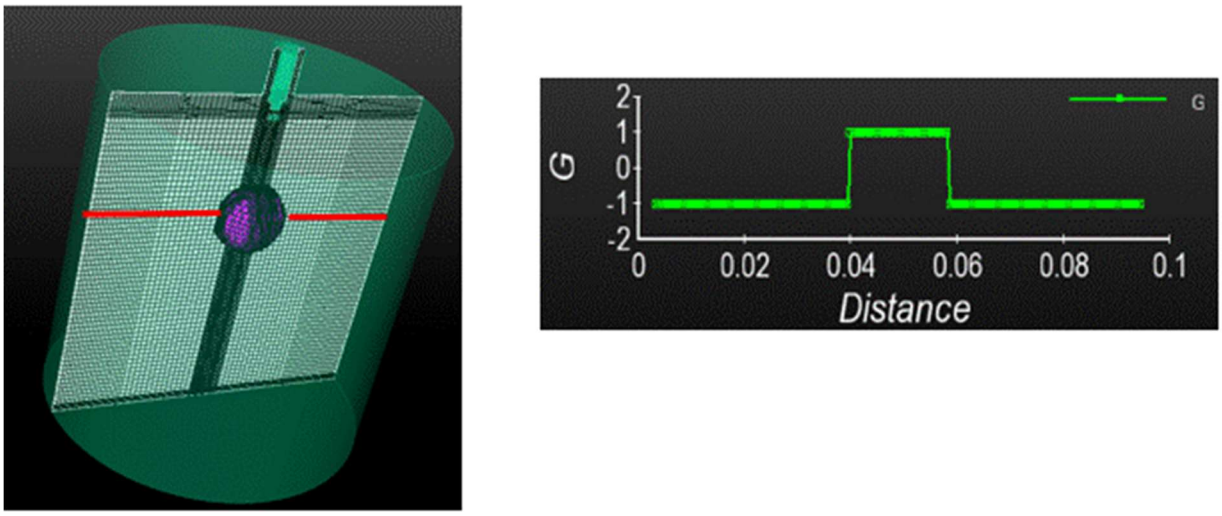

Figure 4-7 *G* value initialization for TCC3 engine mesh

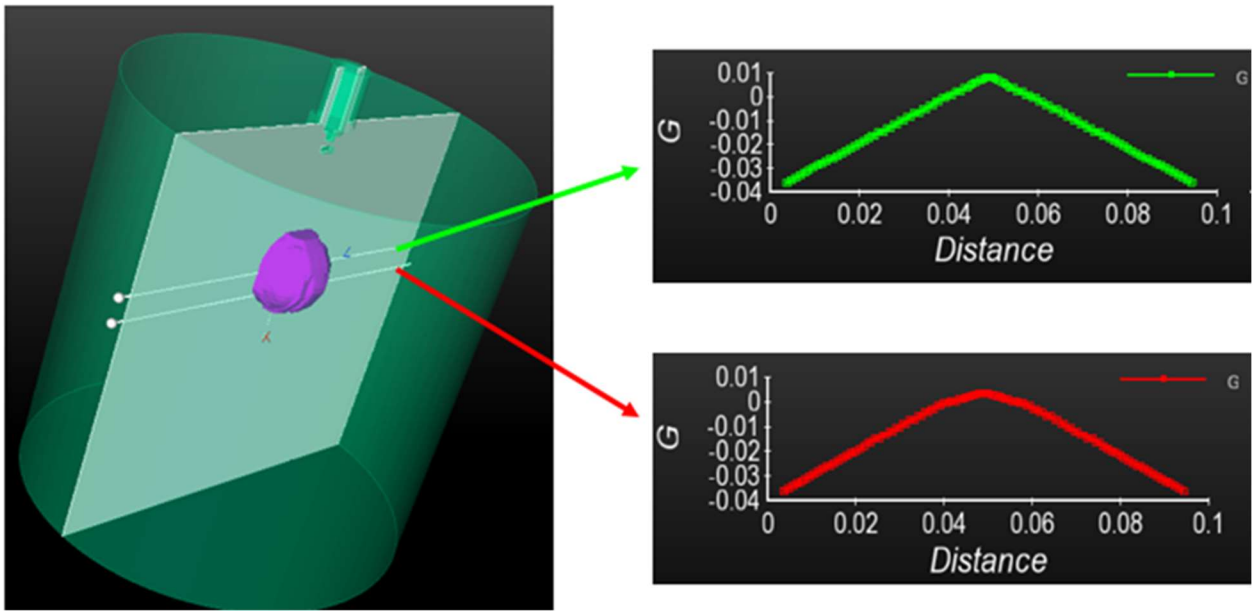

Figure 4-8 *G* value on two extracted lines after reinitialization

Figure 4-8 shows the *G* value on two lines after using the new reinitialization scheme. The top right picture (green line) displays the *G* value on the line passing the $G = 0$ sphere center and the bottom right picture (red line) shows the *G* value on the line tangent with the $G = 0$ sphere. The maximum and minimum *G* values on the top left line are 0.01 and -0.0359. Based on the definition of *G* as a distance function, the maximum *G* value should be at the sphere center. In fact, the maximum value of *G* should be equal to 0.01 which is the radius of the purple sphere. Similarly,

the minimum G value on that line should be the value at the boundary cell with a smallest distance 0.0359 to the $G = 0$ isosurface. From the output, G value on the top line of the left picture after reinitialization is consistent with the theoretical value. Yet, the maximum G value should be zero on the bottom line of the left picture, which is tangent to the sphere. From the output, it can be seen that the maximum G value on the line is 0 consistent with the theoretical G value. These illustrate that G value becomes a distance function after reinitialization. This further confirms the modified reinitialization scheme works sufficiently for non-uniform and non-orthogonal mesh.

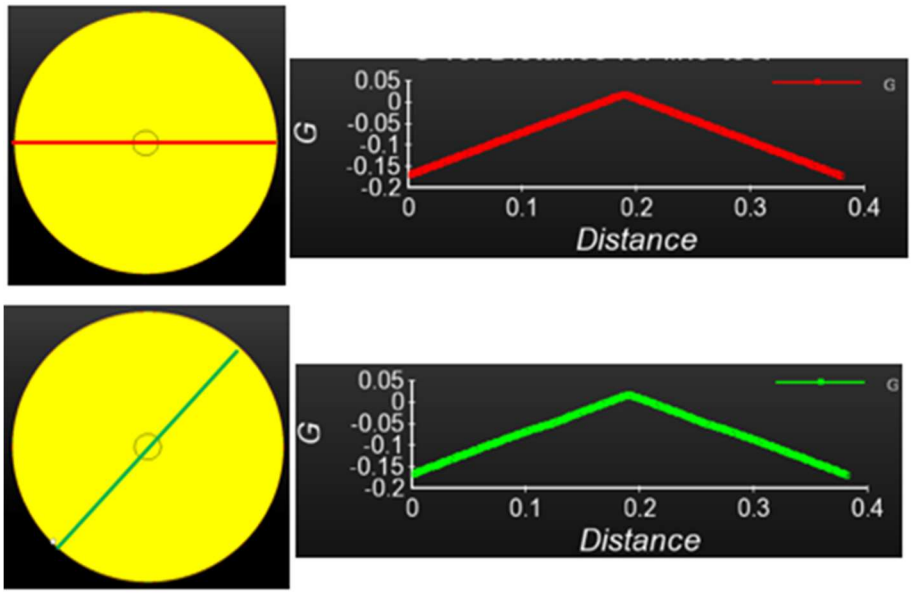

Figure 4-9 G value on two extracted lines after reinitialization (parallel computation)

The reinitialization scheme test for parallel computing is shown in Figure 4-9. In this case, a 2D circle domain with a radius of 192.8 mm is defined. Inside the domain, a $G = 0$ circle (black circle) is defined. The initial G value is set to uniform $G = -1$ outside the $G = 0$ circle and uniform 1 inside the $G = 0$ circle. To validate the application of reinitialization scheme to parallel computing, 8 CPUs were employed in this test case. The two pictures on the right side display the G value on the red and green lines in the domain after reinitialization. It can be seen that G becomes

a distance function after reinitialization, which further verifies that the new reinitialization scheme is valid for parallel computation.

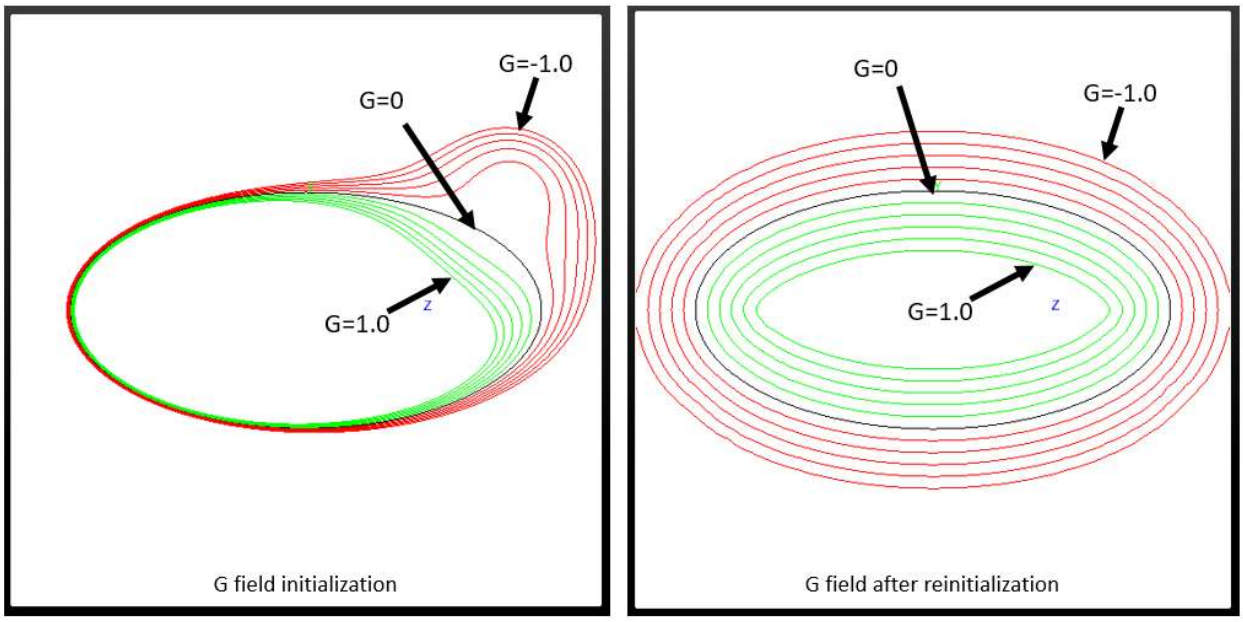

Figure 4-10 Reinitialization test [3]

Figure 4-10 displays a 2D test case as in Ref. [3]. The left picture shows 11 contours running from -1 to 1 and are spaced by 0.2. To test the reinitialization scheme, erroneous distance function isovalue lines, except $G = 0$, which is an ellipse, are created in order to have both small and large gradients near its zero-level set. As mentioned previously, G value is defined as the smallest distance from the $G = 0$ isosurface. This means that all points on a specific isovalue line should have the same smallest distance from the $G = 0$ isosurface. However, this is not true for this case. Two points on the $G = -1.0$ contour line are chosen as well as their smallest distances (line segments 1 and 2) from the $G = 0$ isosurface are displayed. It is obvious that those two line segments are not equal to one another meaning that G is not a distance function. The right picture displays the G value after reinitialization. All G contours become concentric ellipses and all contours are equally spaced.

4.2.2 Reinitialization Validation for Non-Hexahedral Mesh

In this section, the reinitialization scheme validation is based on the efficient direct reinitialization algorithm [106], as described in section 3.1.5.2.

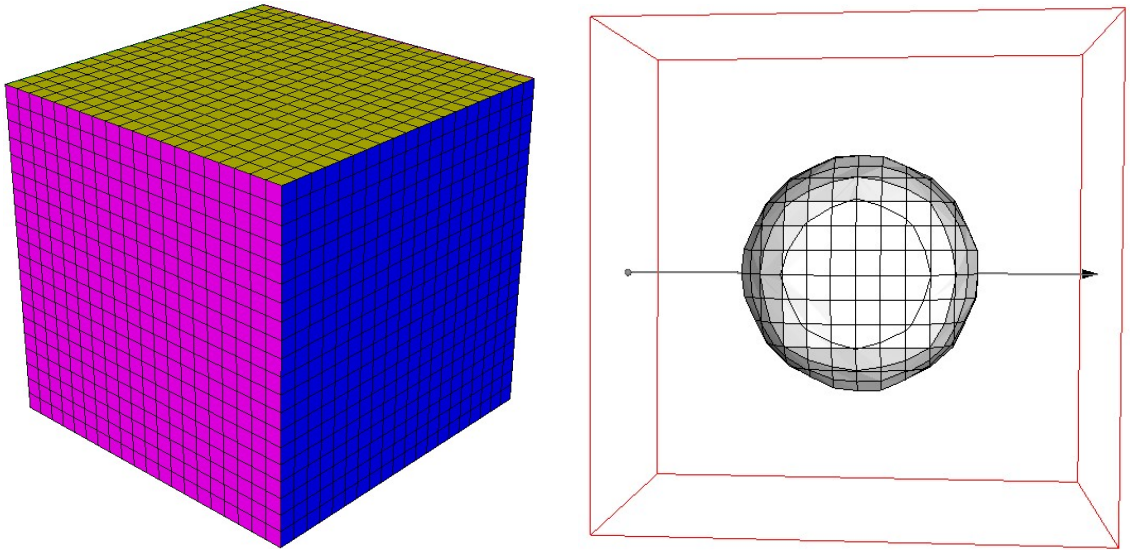

Figure 4-11 Efficient direct reinitialization test on hexahedral mesh

The reinitialization scheme tests used on the hexahedral mesh for serial and parallel computing are shown in Figure 4-11 in the domain after reinitialization. The initial G value is set to uniform G = -1 outside the G = 0 sphere and uniform 1 inside the G = 0 sphere as shown in Figure 4-12 (a). 1 CPU and 8 CPUs were separately employed in this test case. Figure 4-12 (b) displays the G value on the arrow line of Figure 4-11. In this case, a cubic volume with each side 20 mm is set and a G = 0 isosurface with a radius of 5 mm is initialized (white sphere in Figure 4-11). The G values of both serial and parallel computing become a distance function after reinitialization, which further verifies the validity of the efficient direct reinitialization scheme.

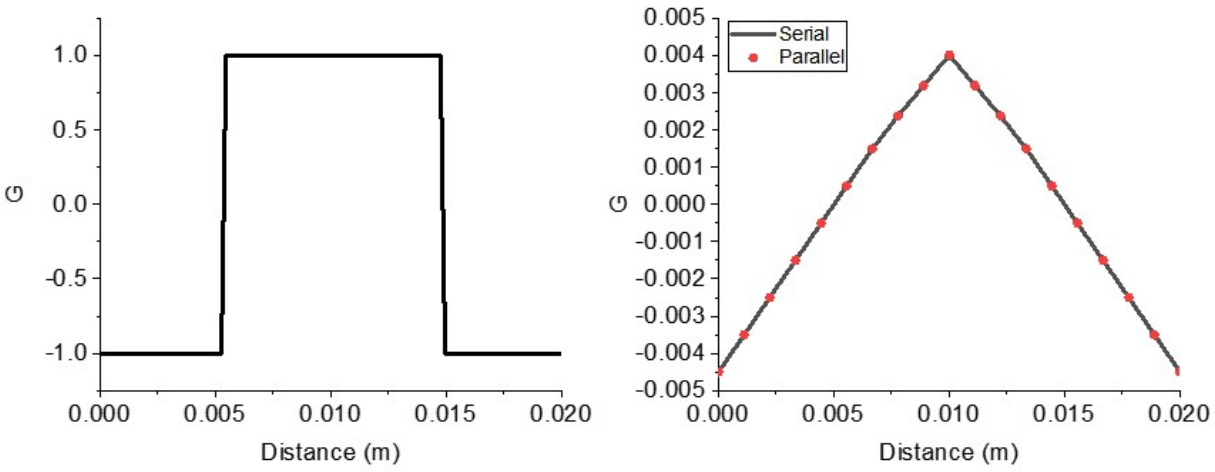

(a) (b)

Figure 4-12 Initial *G* value setting for hexahedral mesh: left picture (a); *G* value after efficient direct reinitialization scheme: right picture (b) (black solid line is the *G* value based on 1 CPU while the dot plot is the *G* value based on 8 CPUs)

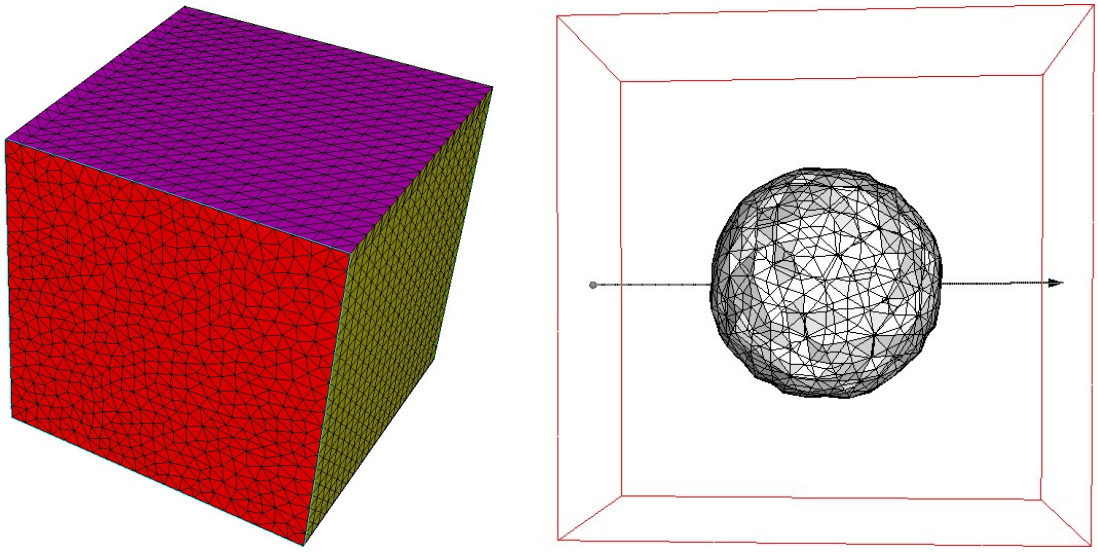

Figure 4-13 Efficient direct reinitialization test on tetrahedral mesh

The reinitialization scheme tests used on the tetrahedral mesh for serial and parallel computing are shown in Figure 4-13. In this case, a cubic volume with each side 20 mm is set (Figure 4-13) and a $G = 0$ isosurface with a radius of 5 mm is initialized (white sphere in Figure 4-13). The *G* value is set to $G = -1$ outside the $G = 0$ sphere surface and uniform 1 inside the $G = 0$ surface as shown in Figure 4-14 (a). 1 CPU and 8 CPUs were separately employed in this test case. Figure

4-14 (b) displays the *G* value on the arrow line of Figure 4-13 in the domain after reinitialization. The *G* values of both serial and parallel computing become a distance function after reinitialization, which further verifies the validity of the efficient direct reinitialization scheme. When compared with *G* value in Figure 4-12, the *G* value in Figure 4-14 (b) does not show a constant slope due to the tetrahedral mesh shape.

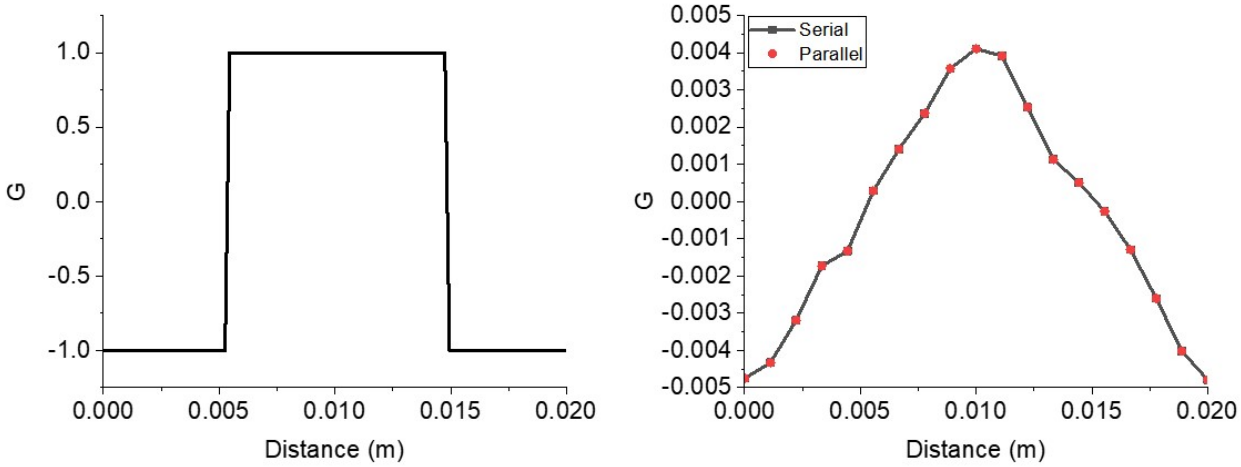

Figure 4-14 Initial *G* value setting for tetrahedral mesh: left picture (a); *G* value after efficient direct reinitialization scheme: right picture (b) (black solid line is the *G* value based on 1 CPU while the dot plot is the *G* value based on 8 CPUs)

The reinitialization scheme tests on the prism mesh for serial and parallel computing are shown in Figure 4-15. In this case, a cubic volume with each side 20 mm is set (Figure 4-15) and a $G = 0$ isosurface with a radius of 5 mm is initialized. The *G* value is set to $G = -1$ outside the $G = 0$ sphere surface and uniform 1 inside the $G = 0$ surface as shown in Figure 4-16 (a). 1 CPU and 8 CPUs were separately employed in this test case. Figure 4-16 (b) displays the *G* value on the arrow line of Figure 4-15 in the domain after reinitialization. It can be seen that the *G* values of both serial and parallel computing become a distance function after reinitialization, which further verifies the validity of the efficient direct reinitialization scheme. When compared with *G* value in

Figure 4-12 (b), *G* value in Figure 4-16 (b) does not display a constant slope due to the prism mesh shape.

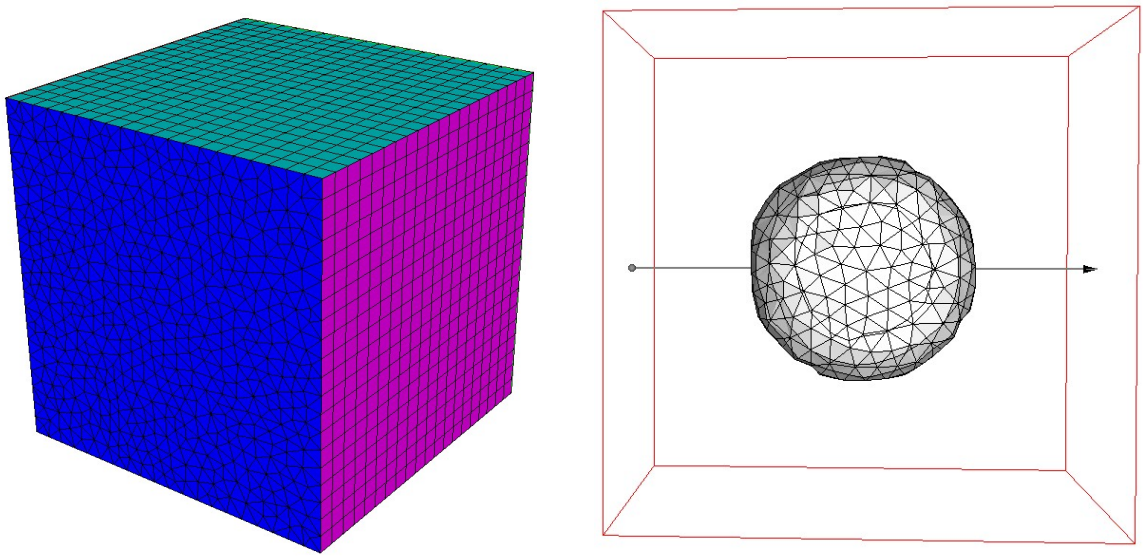

Figure 4-15 Efficient direct reinitialization test on prism mesh

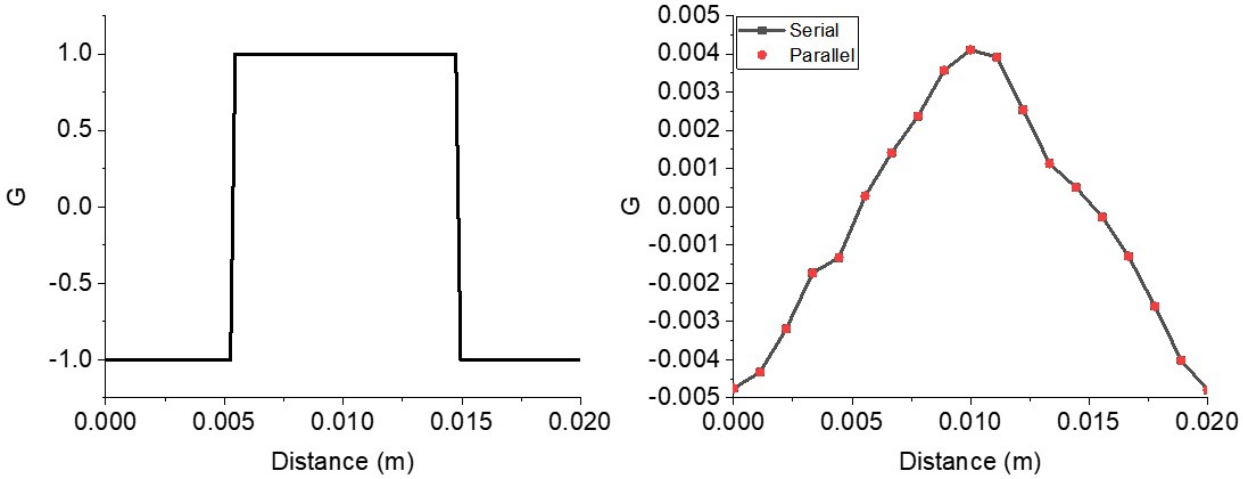

(a) (b)

Figure 4-16 Initial *G* value setting for prism mesh: left picture (a); *G* value after efficient direct reinitialization scheme: right picture (b) (black solid line is the *G* value based on 1 CPU while the dot plot is the *G* value based on 8 CPUs)

Table 4-3 shows the comparison of time consumption between serial and parallel computing for the above efficient direct reinitialization scheme tests. For parallel computing, 8 CPUs were applied. In general, parallel computing saves time in comparison with serial computing, but not exactly 8 times smaller than that of the serial computing due to the message communication among those 8 processors.

Table 4-3 Time consumption comparison for hexahedral, tetrahedral, and prism mesh based on the efficient direct reinitialization scheme

Mesh Type	Serial Time Consumption (s)	Parallel Time Consumption (s)
Hexahedra	4.65	0.72
Tetrahedron	57.61	8.35
Prism	16.51	3.68

4.3 Ignition Validation

To test the efficacy of the developed ignition model, the model is applied to a constant volume charged with mixture of propane and air, and the simulation results are compared with available experimental data [113]. The experiment was implemented in a spherical volume with isotropic and homogenous turbulence. The turbulence was generated by four symmetrically located fans driven by an independently controlled electric motor with a maximum speed of 10,000 rpm. The root mean square (RMS) turbulent velocity u', was found to vary linearly with a fan speed of *N*. The integral length scale l_t was independent of fan speed and found to be 20 mm. For the simulations, a cubic domain of 1 liter in size with a mesh size of 0.5 mm is used. For matters of simplicity, the spark plug has not been included in the mesh geometry. The LES dynamic structure turbulence model is used for all simulations [114].

Five cases are set up for the constant volume vessel and are listed in Table 4-4. In the table, there are mainly two variables that change from case to case: one is the u' and the other is the C_{bd} defined in Eqn. (3-50). Different values of u' indicate different turbulence levels, and the

parameter C_{bd} affects the breakdown energy in the ignition, which further affects the initial flame kernel size. Since the term C_{bd} is on the denominator of Eqn. (3-50), the bigger value of C_{bd} leads to a smaller breakdown voltage and furthermore a smaller initial flame kernel radius. Besides, the different C_{bd} values are set in order to initialize kernel radius in the simulations to be close to the experimental kernel radius. The term a_t in Eqn. (3-61) for wrinkling factor calculation requires the integral length scale l_t as an input even in the context of LES [109]. However, as the l_t in LES is unknown, the efficiency function in Eqn. (3-61) is estimated using SGS quantities $\hat{\Delta}$ and $\hat{u}'$.

Table 4-4 Cases set up for constant volume vessel combustion

Case #	Fuel	Equivalence ratio	u' (m/s)	T (K)	P (bar)	C_{bd} in Eqn. (3-50)
1	C_3H_8	1.0	2.36	300	1.0	300
2	C_3H_8	1.0	2.36	300	1.0	150
3	C_3H_8	1.0	2.36	300	1.0	120
4	C_3H_8	1.0	4.72	300	1.0	300
5	C_3H_8	1.0	4.72	300	1.0	120

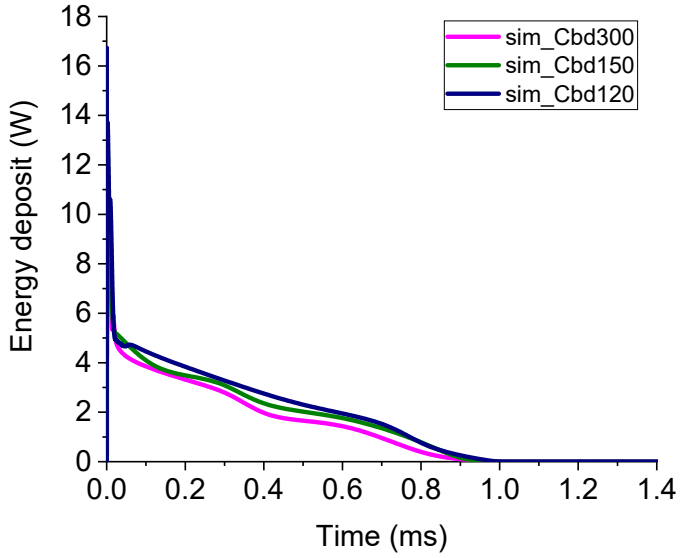

Figure 4-17 Energy deposit rate for constant volume case (Table 4-4, Case 1, Case 2 and Case 3 with C_{bd}= 300, 150, and 120 $\mathrm{kV/(J-mm)^{0.5}}$, respectively. All three cases are initialized with u'=2.36 m/s)

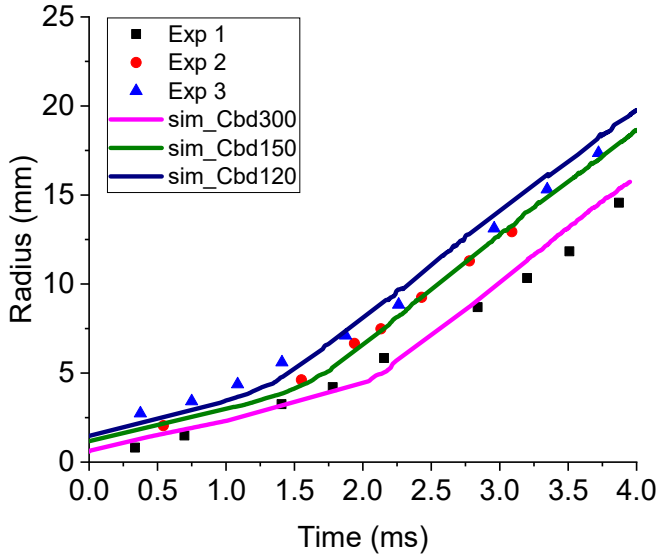

Figure 4-18 Comparison of flame kernel radius between experiment [113] and simulation for propane (Table 4-4 Case 1, Case2, and Case 3 with C_{bd}= 300, 150, and 120 $\mathrm{kV/(J-mm)^{0.5}}$, respectively. All three cases are initialized with u'=2.36 m/s)

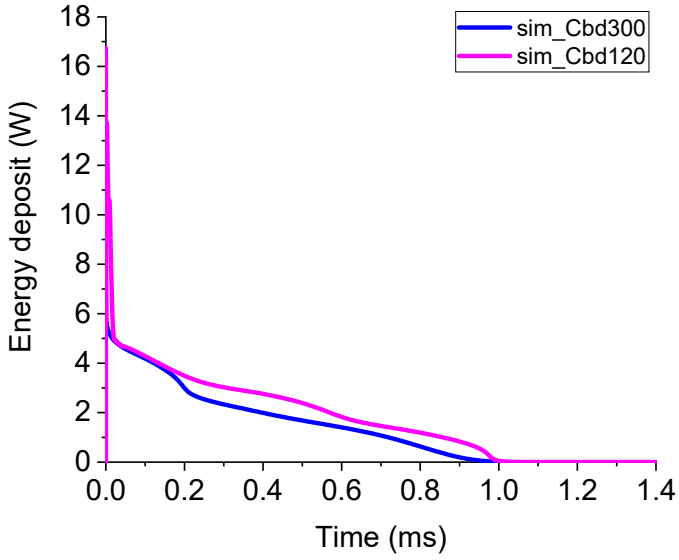

Figure 4-19 Energy deposit rate for constant volume case (Table 4-4, Case 4 and Case 5 with C_{bd}= 300 and 120 $\mathrm{kV/(J-mm)^{0.5}}$, respectively. Both cases are initialized with u'=4.72 m/s)

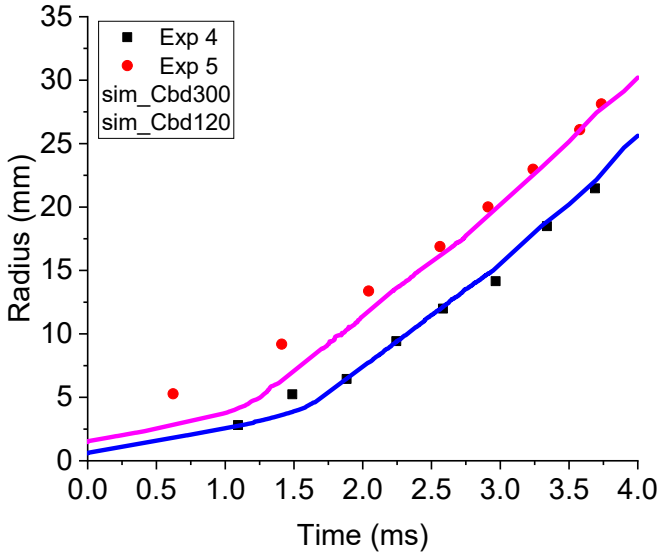

Figure 4-20 Flame kernel radius comparison between experiment [113] and simulation for propane (Table 4-4, Case 4 and Case 5 with C_{bd}= 300 and 120 $\mathrm{kV/(J-mm)^{0.5}}$, respectively. Both cases are initialized with u'=4.72 m/s)

Figure 4-17 through Figure 4-20 compare the various energy deposit rates, and compare the measured kernel radius for 1 bar propane/air mixture under $u' = 2.36$ m/s and $u' = 4.72$ m/s for the five simulation cases in Table 4-4.

In the experiments, the measured initial kernel radius differs from cycle to cycle. The big variation of kernel radius growth is principally attributed to shot-to-shot differences in the size of turbulence eddies experienced at the plug at the ignition timing [113]. To account for these phenomena, the parameter C_{bd} in Eqn. (3-50) is set to different values to initialize different flame kernel sizes. It can be deducted from Eqn. (3-50) and Eqn. (3-53) that changing the parameter C_{bd} can alter the breakdown energy E_{bd} and change the initial flame kernel radius. The total energy deposited into the gas mixture is set to be 8.5 mJ as in [35]. Based on that, the parameter C_{bd} is set to be 300, 150, and 120 (corresponding E_{bd} 2.36 V, 1.51 V, and 0.38 V, respectively) to initialize kernel radius to be 0.59 mm, 1.18 mm, and 1.47 mm for the ignition model validation, which is close to the initial kernel radius measured in the experiments. The transition radius was set to be 4

mm for calibration in the simulation since it worked better than other transition radius setting. In general, the energy deposits in Figure 4-17 and Figure 4-19 show small cycle to cycle variations for both turbulence levels. Moreover, the radius predictions from simulation display agreement with the experimental data, as shown in Figure 4-18 and Figure 4-20, and is considered to be satisfactory for varying turbulent intensities and initial conditions. Furthermore, increasing the C_{bd} value tends to decrease the initial radius, which in turn slows down the overall kernel growth. This indicates C_{bd} has a noticeable impact on the overall results which is consistent with the experimental observation [8][38][115] where increasing the breakdown energy results in an increase in kernel radius.

One last point that is crucial to notice is the kernel growth rate under different turbulence levels. When compared with the kernel radius growth under $u' = 2.36\ \mathrm{m/s}$, as seen in Figure 4-18, it is observed that as the turbulent kinetic energy increases ($u' = 4.72\ \mathrm{m/s}$), the flame kernel grows at a faster rate, as shown in Figure 4-20, for the same initial condition of pressure, temperature, and equivalence ratio.

One can see in Figure 4-21 and Figure 4-22 is the wrinkling factor Ξ calculated in Eqn. (3-60) as a function of time. The transition radius from region (a) to region (b) (Figure 3-21) is set to be 3 mm. This location is where the wrinkling factor Ξ line becomes a constant value in Figure 4-21 and Figure 4-22. The wrinkling factor Ξ is not calculated after that point due to the effect of turbulence on wrinkling the flame kernel surface is implicitly considered in the transition function α (Eqn. (3-64)). To explain this another way, the wrinkling factor increases the flame surface to increase the burning rate, while the transition function α increases the flame propagation speed and further increases the burning rate. Figure 4-21 and Figure 4-22 show that a smaller kernel size (bigger C_{bd} value) takes more time to reach the transition radius. Additionally, the

higher initial turbulence level (Figure 4-22) has a larger effect on the flame surface through a larger value of the wrinkling factor Ξ.

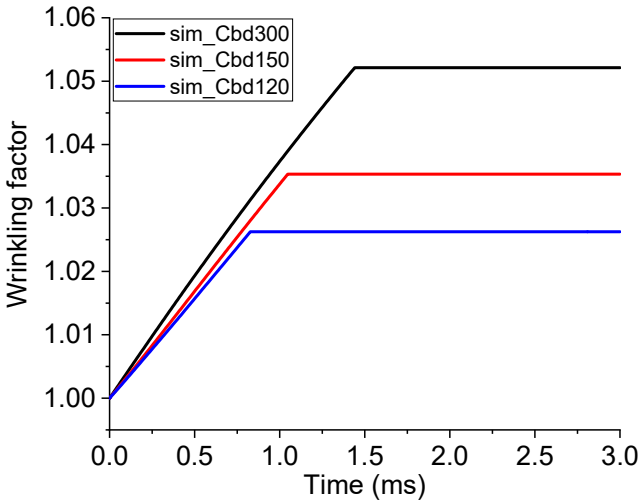

Figure 4-21 Wrinkling factor Ξ comparison for different C_{bd} (Table 4-4 Case 1, Case2, and Case 3 with C_{bd}= 300, 150, and 120 $\mathrm{kV/(J-mm)^{0.5}}$, respectively. All three cases are initialized with u'=2.36 m/s), the point where Ξ becomes constant indicates the transition from region (a) to region (b) in ignition model

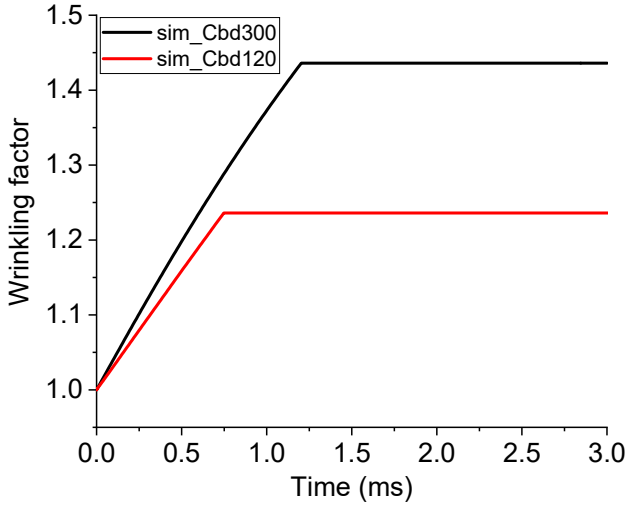

Figure 4-22 Wrinkling factor Ξ comparison for different C_{bd} (Table 4-4, Case 4 and Case 5 with C_{bd}= 300 and 120 $\mathrm{kV/(J-mm)^{0.5}}$, respectively. Both cases are initialized with u'=4.72 m/s), the point where Ξ becomes constant indicates the transition from region (a) to region (b) in ignition model

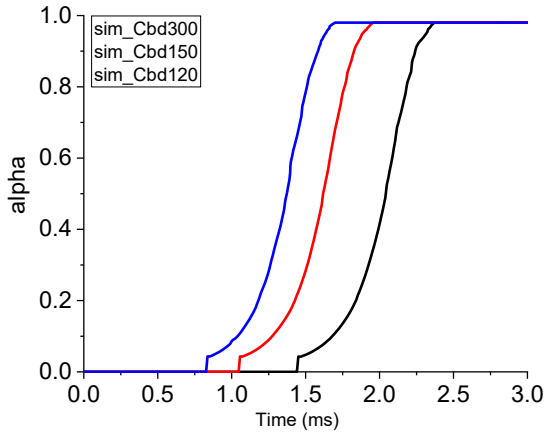

Figure 4-23 Transition function α for different C_{bd} values (Table 4-4: Case 1, Case2, and Case 3 with C_{bd}= 300, 150, and 120 $\mathrm{kV/(J-mm)^{0.5}}$, respectively. All three cases are initialized with u'=2.36 m/s). The point where the value of α rises above zero indicates the transition from region (a) to region (b) in the ignition model

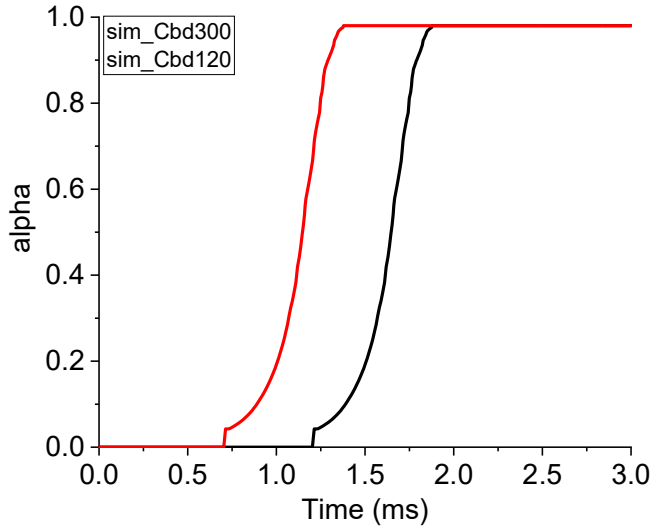

Figure 4-24 Transition function α for different C_{bd} values (Table 4-4, Case 4 and Case 5 with C_{bd}= 300 and 120 $\mathrm{kV/(J-mm)^{0.5}}$, respectively. Both cases are initialized with u'=4.72 m/s), the point where the value of α rises above zero indicates the transition from region (a) to region (b) in the ignition model

Figure 4-23 and Figure 4-24 display the α transition function for different values of C_{bd}. As the figures display, α starts to exert its effect earlier for cases with larger initial kernel size which reaches the transition radius earlier. For cases with a more intense turbulence level, the change

from transition region (region (b)) to fully turbulent flame propagation speed region (region (c)) advances in time when compared with cases with a weaker turbulence level.

Figure 4-25 illustrates the radius comparison among experiments, the simulations based on swept-volume algorithm, and the simulations without the swept-volume algorithm for u' = 2.36 m/s. The basic idea for the swept-volume algorithm is shown in Figure 3-12. The key step is to calculate the sub-volume V_s in Eqn. (3-45). For the non-swept-volume algorithm, the V_s term is approximated as the product of $s_{flame}A_F\Delta t$ with s_{flame} the flame propagation speed as in Eqn. (3-63), A_F the flame isosurface ($G = 0$) in the mesh cell, and Δt the time step. As the figure shows, the non-swept volume algorithm overpredicts the radius when compared with the swept-volume algorithm. The cause for this phenomenon is as follows: the reaction is assumed to mainly take place in the volume swept by the flame in the current G equation combustion model and the product $s_{flame}A_F\Delta t$ could not be guaranteed to approximate the correct volume during the simulation; thus, it leads to a sufficient prediction of the kernel radius.

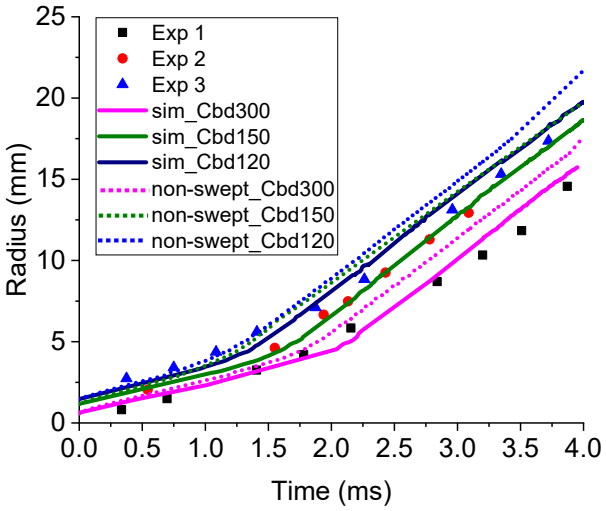

Figure 4-25 Comparison of radius among experiments, simulation based on swept-volume algorithm, and simulation without swept-volume algorithm (Table 4-4 Case 1, Case2, and Case 3. All three cases are initialized with u'=2.36 m/s)

4.4 RANS Validation for TCC3 Engine

In this section, both the GM combustion model and the swept-volume combustion model are applied to the TCC3 (transparent combustion chamber) engine case [4]. The modeled TCC3 engine is a General Motors simple cylinder test engine with a spark plug situated on the symmetry axis at the center of the cylinder head. For the TCC3 case test in this section, the mixture can be treated as homogeneous mixture and the k-epsilon turbulence model could be used. The engine geometry is given in Figure 4-26 and the mesh information is given in Table 4-5. Details about the mesh motion algorithm development in OpenFOAM can be found in [116]. The specifications and two modeled operating conditions are listed in Table 4-6.

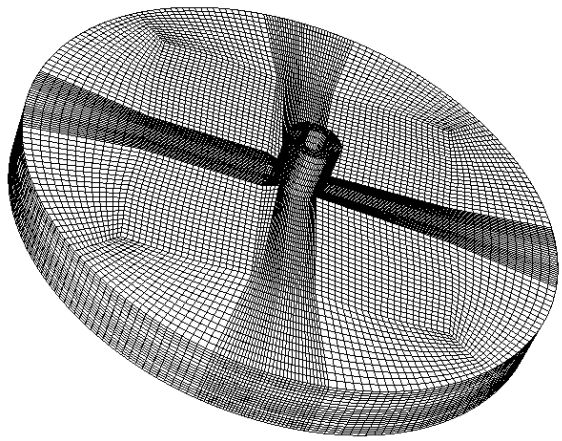

Figure 4-26 Combustion chamber geometry of TCC3 gasoline engine

Table 4-5 Mesh details

Location	No. of cells	Max/Min mesh face size
TDC	168027	2/0.1
110 BTDC	630000	2/0.1

Table 4-6 Specifications and operating conditions of gasoline TCC3 engine

Engine Type	TCC3 Engine	
Bore × Stroke	92 × 86 mm	
Compression Ratio	10:1	
IVC, EVO (°ATDC)	-110, 130	
Fuel	Propane	
Modeled Operating Conditions		
	Case 1	Case 2
Engine Speed (rev/min)	1300	1300
Equivalence Ratio	1.0	0.705
Ignition Timing (°ATDC)	-18	-25.5
Initial Temperature (K)	410.16	460
Initial Pressure (kPa)	54.53	57.32

The GM model and swept-volume mode were applied for the TCC3 engine validation. For the GM model, a one-step reaction was applied. For the swept-volume combustion model, CEQ coupled with detailed chemistry [117] was used. The simulation results were compared with the TCC3 engine data [4]. Engine combustion simulation with intake and exhaust value motion is an extraordinarily complex process and currently it is difficult to carry out this process in OpenFOAM. To simplify the complexity of the simulation, only the process between intake valve closure (IVC) and exhaust value opening (EVO) is simulated, thus indicating the valve motion process is not implemented in this section. Consequently, a suitable initial condition at the IVC point needs to be set. To solve this problem, the solution utilized mapping solution data from CONVERGE CFD software to OpenFOAM at intake valve closure. The method for the mapping is given in Appendix C. For the following simulation, only the turbulent kinetic energy, the turbulent dissipation rate, and the velocities were mapped from CONVERGE. For other variables, such as temperature and pressure, averaged in-cylinder values from experiments were applied.

For the engine simulation, the parameter b_1 in turbulent burning velocity correlation is set to 2.0 and 1.5 for the swept-volume and the GM combustion models, respectively. The pseudo flame

thickness term in delta smoothing function (Eqn. (3-41)) of GM model is set at a fixed value (2 mm). This value indicates that the flame surface exists in all mesh cells with a G value between -0.001 to 0.001. For the tested TCC3 engine mesh in this report, most mesh sizes are about 1 mm, therefore indicating reaction occurs in about two mesh layers at every time step in the GM model before the flame propagates to the wall. For the swept-volume combustion model, the swept-volume is usually much lower than the cell size for one time step [69]. As shown in Figure 3-7, the turbulent burning velocity decreases with a decrease of b_1. This decrease is the reason why a relatively smaller value was chosen for GM model.

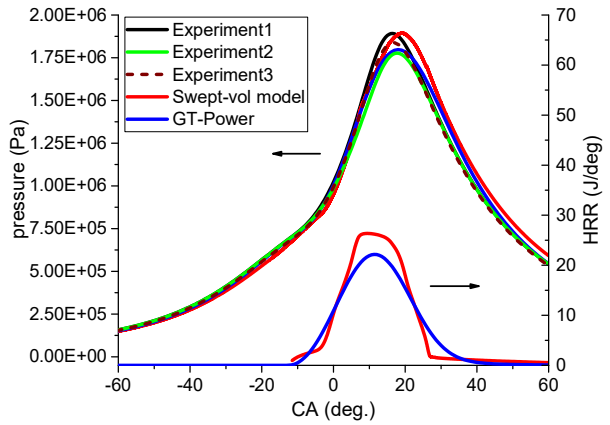

(a)

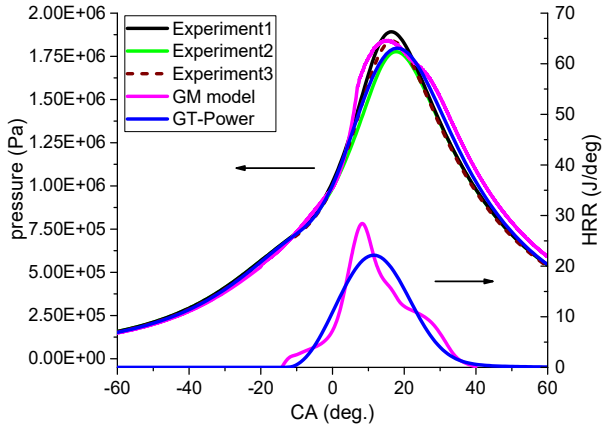

(b)

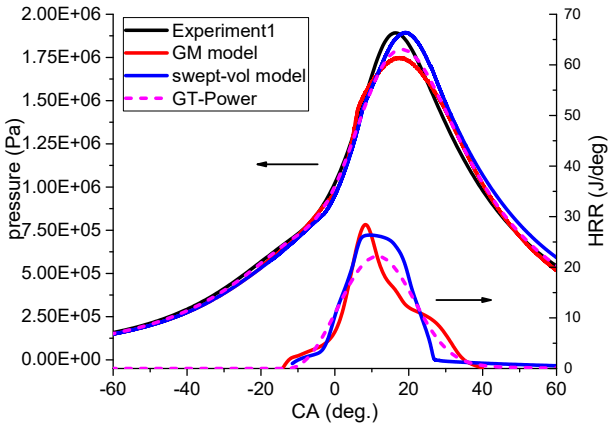

(c)

Figure 4-27 Comparison of predicted in-cylinder pressure and HRR with experimental and GT-POWER data for stoichiometric case ((a). comparison of predicted pressure trace and HRR from the swept-volume combustion model and GM model with experiments and GT-Power; (b). the predicted in-cylinder pressure trace from swept-volume model with experimental and GT-POWER data; (c). the predicted in-cylinder pressure trace from both models with experimental and GT-POWER data)

Figure 4-27 compares the predicted pressure trace and heat release rate (HRR) from the swept-volume combustion model and GM model with those of same factors from experiments and GT-Power for an equivalence ratio of phi = 1.0. The HRR was compared with that of GT-POWER. Figure 4-27 (a) shows the predicted in-cylinder pressure trace from swept-volume model with experimental and GT-POWER data. Figure 4-27 (b) shows the predicted in-cylinder pressure trace from GM model with experimental and GT-POWER data. Figure 4-27 (c) shows the predicted in-cylinder pressure trace from both models with experimental and GT-POWER data. Both predicted pressure curves match the experimental pressures reasonably well and the HRR has the same order value as that of GT-POWER. When compared with pressure trace from the swept-volume combustion model, the pressure trace of GM model is a bit more advanced. This difference is mainly due to the fact that the reaction occurs in about two mesh layers for the GM model instead of only in the volume swept by the flame, as in the swept-volume combustion model.

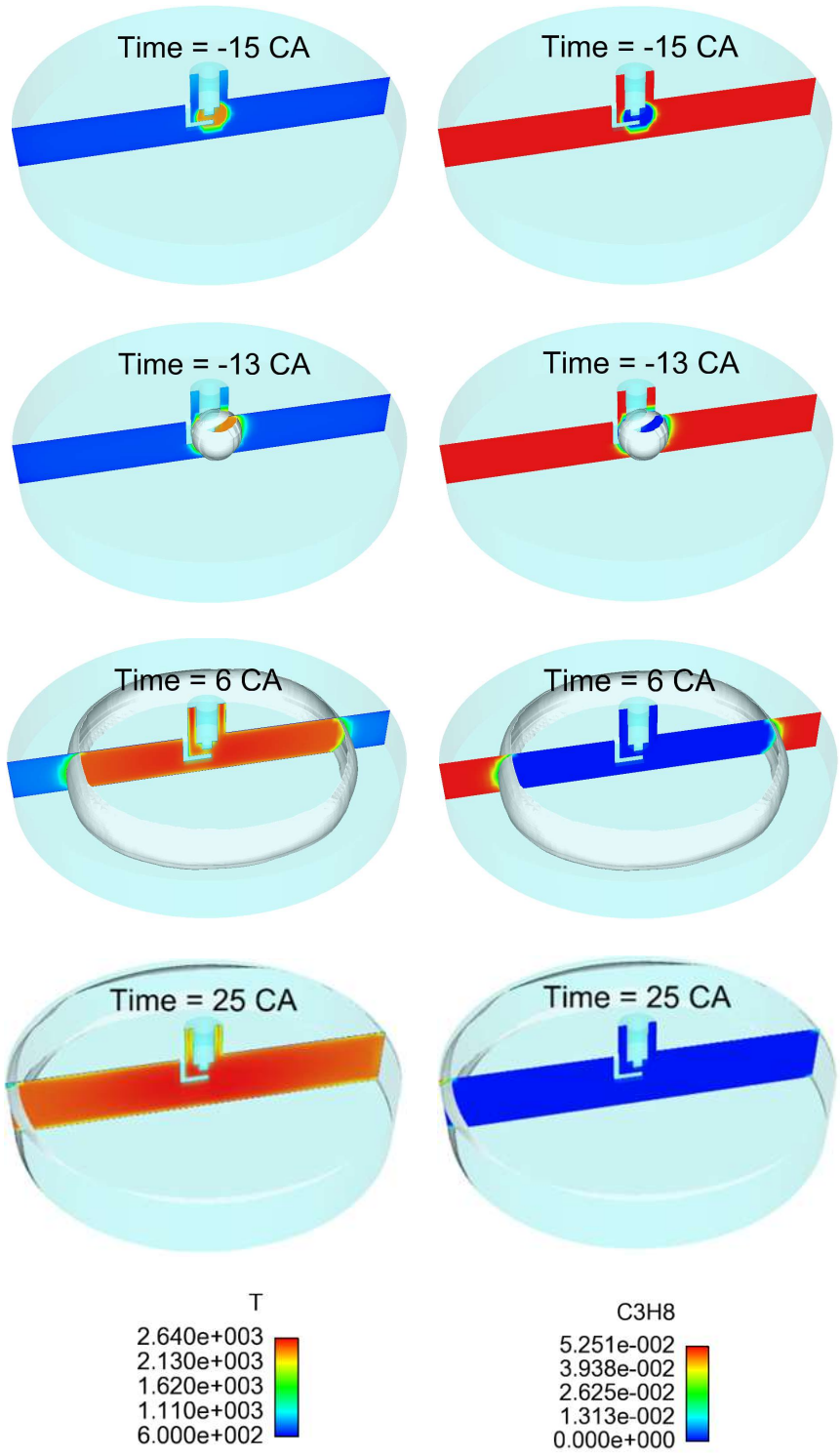

Figure 4-28 In-cylinder temperature and propane mass fraction contours at different crank angle of swept-volume model (Spark timing = - 18° ATDC). White surface indicates the flame front location.

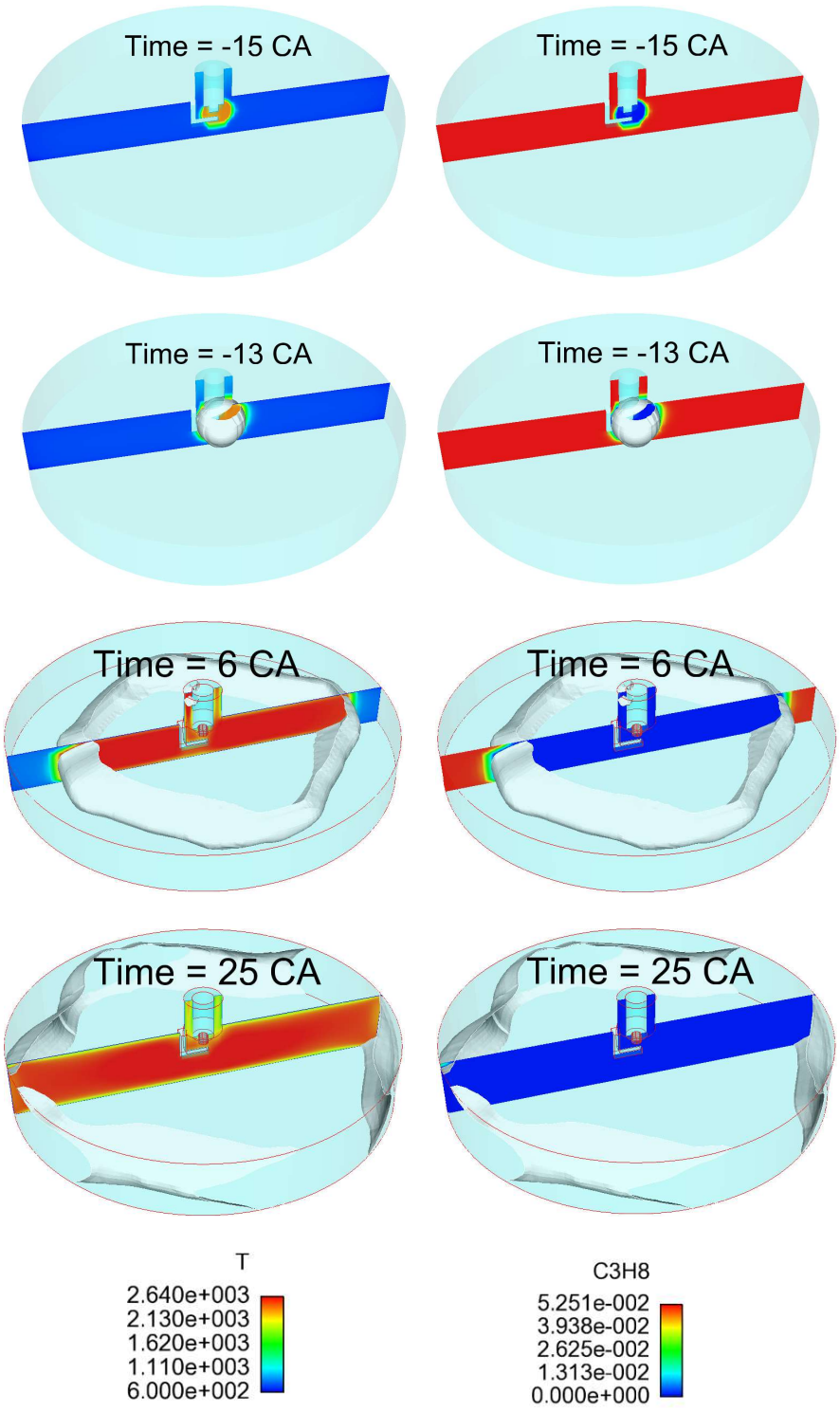

Figure 4-29 In-cylinder temperature and propane mass fraction contours at different crank angle of GM model (Spark timing = - 18° ATDC). White surface indicates the flame front location

Figure 4-28 and Figure 4-29 show the simulated in-cylinder temperature and propane profiles as the flame propagates out from the spark plug, and the white surface denotes the locations of the

mean flame front (G = 0 isosurface). As one can see, the temperatures of the mixture behind the turbulent flame brush for both the swept-volume and GM models are above 2500 K, which is approximately equal to the local equilibrium temperature. The G = 0 isosurface approximates an annular volume for the swept-volume model and a square shape for the GM model. This phenomenon occurs because the reactions mainly happen in the swept-volume region for the swept-volume model, that is much smaller than the cell size, and it occurs in about two layers for the GM model based on current TCC3 mesh size.

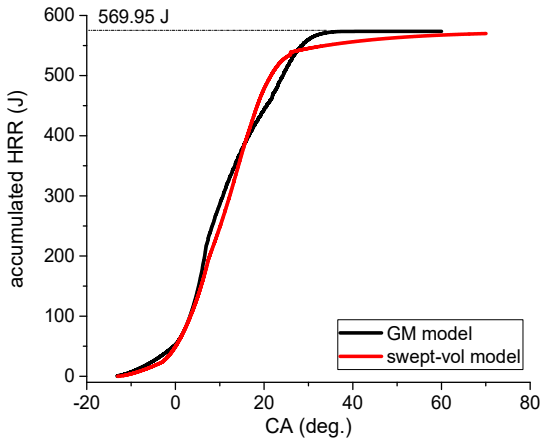

Figure 4-30 Accumulated HRR comparison between swept-volume and GM models (Stoichiometric case: Table 4-6, Case 1)

Table 4-7 Accumulated HRR comparison between simulations and experiment (Stoichiometric case: Table 4-6, Case 1)

Combustion Phase	Experiment/ Standard Deviation	Swept-volume Model	GM Model
CA10 (°ATDC)	0.55/1.59	0.39	0.52
CA50 (°ATDC)	10.36/2.23	10.77	10.04
CA90 (°ATDC)	18.55/2.88	21.41	24.34

Figure 4-30 displays the accumulated HRR for the swept-volume model and GM model. The total amount of fuel is 12.4 mg corresponding to theoretical total HRR 570.4 J based on the lower heating value (LHV) 4.6e7 J/kg for propane. The total HRR from simulation is extremely close to

the theoretical value. Table 4-7 shows the accumulated HRR comparison between the simulations and the experiments for CA10, CA50 and CA90. From the table, one can see that the crank angles of CA10, CA50 and CA90 for swept-volume model are within the allowable standard deviation of experiments. For the GM model, the occurrences of CA10 and CA50 are within the acceptable standard deviations while CA90 is retarded.

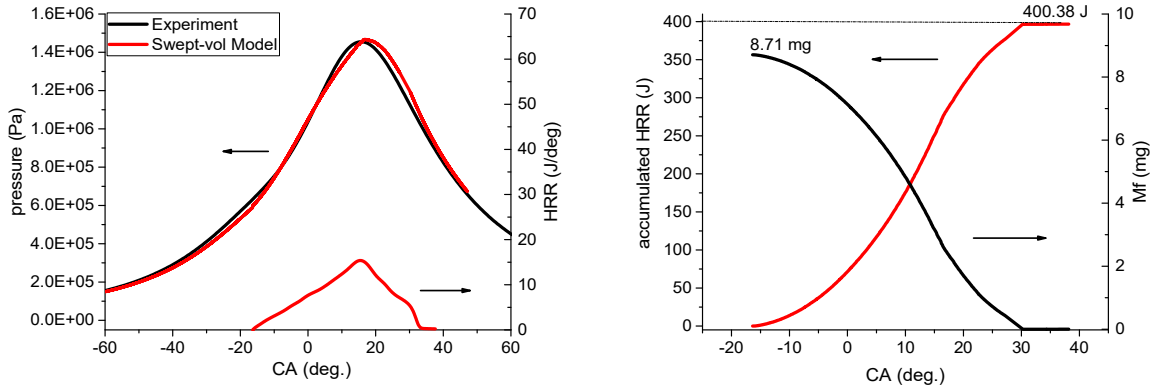

(a) (b)

Figure 4-31 Comparison of predicted in-cylinder pressure and HRR with experimental data ((a). pressure trace comparison between experiment and simulation; (b). accumulated HRR and fuel mass)

Table 4-8 Accumulated HRR comparison between swept-volume model and experiment (Lean case: Table 4-6, Case 2)

Combustion Phase	Experiment/ Standard Deviation	Swept-volume Model
CA10 (°ATDC)	-0.89/2.47	-4.03
CA50 (°ATDC)	11.38/3.68	11.54
CA90 (°ATDC)	24.56/4.91	44.05

Figure 4-31 (a) displays a comparison of the pressure trace between swept-volume model with the experiment for equivalence ratio phi = 0.705 (Table 4-6, Case 2). In general, a particularly strong agreement was obtained between the simulated and measured pressure, when considering that no-case-by-case tuning of any model constant was made. Figure 4-31 (b) shows the changes

of fuel mass and accumulated HRR over time. The total amount of fuel is 8.71 mg corresponding to theoretical total HRR 400.66 J that is based on the lower heating value (LHV) 4.6e7 J/kg for propane. This total HRR from simulation is remarkably close to the theoretical value, as displayed in Figure 4-31. Table 4-8 shows the accumulated HRR comparison between the simulations and the experiment for CA10, CA50, and CA90 for lean combustion. As in the table, the data in terms of combustion phasing is in general consistent with experiments.

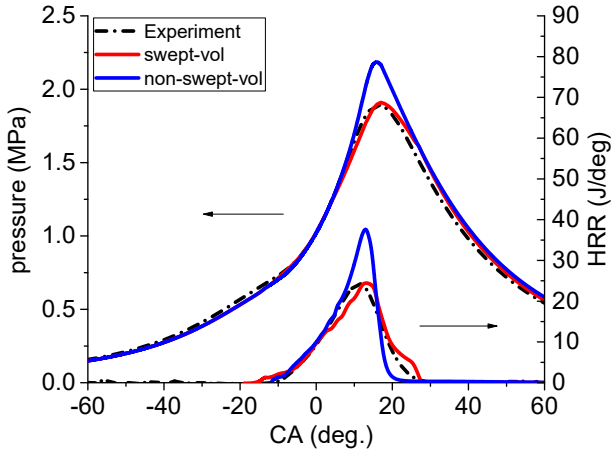

Figure 4-32 Comparison of pressure trace and heat release rate between experiment and simulations for stoichiometric propane air mixture

Figure 4-32 shows the comparison of pressure trace and heat release rate between experiment and simulation for stoichiometric propane air mixture. The reaction rate of swept-volume based combustion is calculated as indicated in Eqn. (3-46), while Eqn. (3-42) pertains to the non-swept-volume combustion model. As is displayed in the figure, the pressure trace from the swept-volume based simulation agrees with the experimental pressure trace, while the pressure trace based on the non-swept-volume algorithm overpredicts the peak pressure. The overprediction is due to the approximation of the reaction volume causing inaccurate reaction rate calculation.

Chapter 5 Engine Combustion Variability

In this chapter, the combination of ignition model and the swept-volume based combustion model is applied to the TCC3 engine to investigate the CCV phenomena. This chapter is divided into three sections: first, the relationship between mesh resolution and flame surface capture is introduced; second the model application to stoichiometric propane/air combustion is studied; and lastly lean combustion is detailed.

5.1 Effect of Mesh Resolution on Flame Surface Capture

As described in Chapter 3 the WSSIM is divided into Lagrangian and Eulerian phases. It is important to ensure that the kernel can be captured by the mesh in both phases, especially in the Lagrangian phase where the kernel size is relatively much smaller than that of Eulerian phase. Otherwise, the flame front surface cannot traced accurately and thus lead to wrong predictions of kernel radius and species reactions. This is illustrated in the following example.

In this test case, the mesh domain is a 50 * 50 * 50 mm cubic volume with uniform mesh size in x, y, and z directions given below. The initial condition setting is displayed in Table 5-1. The term C_{bd} in Eqn. (3-50) is set to be 300 $\mathrm{kV/(J-mm)^{0.5}}$ corresponding to an initial kernel radius of 0.58 mm. Two mesh resolutions are tested: 1 mm and 0.5 mm.

Table 5-1 Initial condition setting for constant volume vessel combustion

Fuel	Propane	
Pressure (atm)	1.0	
Temperature (K)	360	
Equivalence Ratio	1.0	
Ignition Timing (s)	0	
Mesh Resolution (mm)	1.0	0.5

Figure 5-1 shows the G = 0 flame front (white surface) and propane distribution on the cut plane passing the axis at 4 ms after the start of ignition. Since the pressure, temperature, species,

etc. are set to be uniform in the whole cubic domain, the kernel shape should be a sphere, in theory, as time increases. However, it can be seen from the plot that the $G = 0$ flame surface is not a sphere when the cell size is 1 mm (Figure 5-1 (a)). Moreover, it seems that species reactions occur in the unburnt domain where the flame front has not arrived from the propane distribution in Figure 5-1 (a), which is obviously unreasonable. When compared with the mesh size of 1 mm, the $G = 0$ flame surface is a sphere and species reactions only occur inside the flame surface domain, which is the burnt region when the cell size is 0.5 mm (Figure 5-1 (b)).

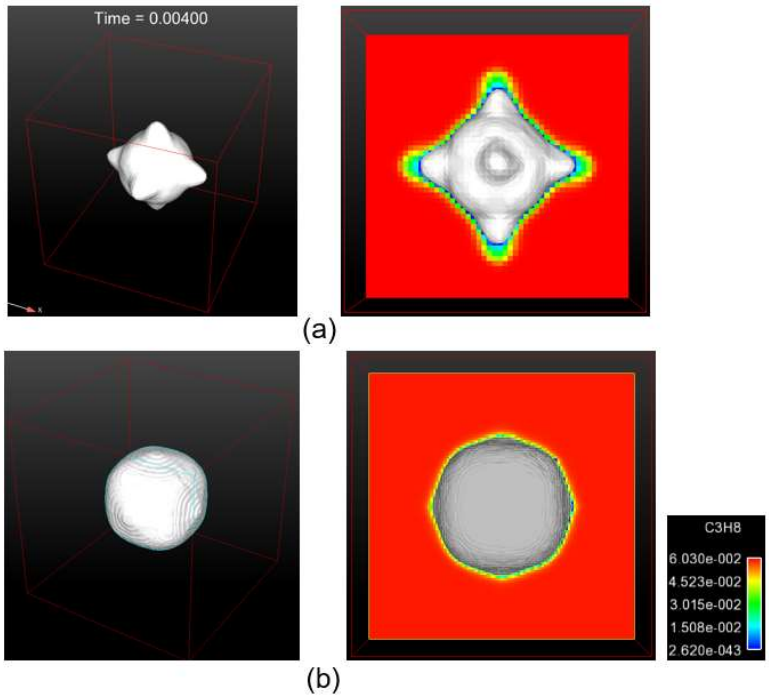

Figure 5-1 The $G = 0$ flame front (white surface) and propane distribution on the cut plane passing the axis at 4 ms after the start of ignition. ((a). results for the mesh size 1mm; (b) results for the mesh size 0.5 mm.)

The results above can be explained through the ratio of the inverse curvature to the mesh size. When the cell size is 1 mm, the ratio at the beginning of ignition is 0.58 meaning that the mesh size could not capture the curvature of the flame kernel. Although, that same ratio is 1.16 when the cell size is 0.5 mm, thus indicating the flame could be captured by such kind of mesh size. The

conclusion achieved from this test case is that the mesh size should be less than the inverse curvature of the initial kernel size in order to capture the kernel front as it grows in time.

5.2 Stoichiometric Combustion

In this section, the simulation cycles and related results are presented first, and then followed by an investigation of sensitivity tests. Then, the effect of transition radius is described. After this is a study of the effects of keeping the center location of the ignition kernel unchanged. Finally, the fuel effect on the ignition energy deposition is shown.

5.2.1 Combustion of Multiple Simulation Cycles

To investigate the CCV phenomena in engines, the TCC3 engine is modeled and 30 simulation cycles are implemented. The engine geometry is displayed in Chapter 4 (Figure 4-26) and the initial conditions for the 30 cycles are listed in Table 5-2. To simplify the complexity of the calculation, only the process between the intake valve closure (IVC) and the exhaust value opening (EVO) is simulated, which denotes that the valve motion process is not implemented in the simulation. For the initial conditions, variables include the velocity field, species, temperature, etc. and these are prescribed from a separate calculation, which is explained in Appendix C Mapping Methods [118].

Table 5-2 Specifications and operating conditions of TCC3 engine

Engine Type	TCC3 Engine
Bore × Stroke	92 × 86 mm
Compression Ratio	10:1
Engine Speed (rev/min)	1300
IVC, EVO (°ATDC)	-110, 130
Fuel	Propane
Ignition Timing (°ATDC)	-18
Initial T, p, velocity	Mapped from Converge
Initial Species	Mapped from Converge
Transition Radius (mm)	1.0
Cycle Number	30

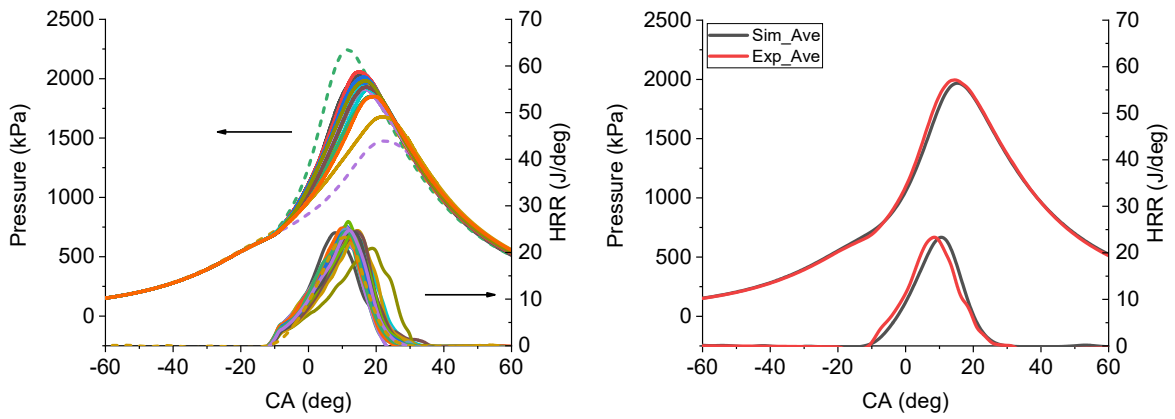

Figure 5-2 Comparison of the pressure trace and heat release rate between experiment and simulations for the stoichiometric propane air mixture ((a) Pressure trace and HRR of experiments and simulations; (b) Averaged pressure trace comparison between experiment and simulation cycles)

Figure 5-2 (a) shows a comparison of the pressure traces and the heat release rates between the experiment and the simulation for a stoichiometric propane air mixture. There is noticeable cyclic variability in the engine experimental data. In the figure, three dashed lines are the upper, lower, and averaged pressure traces based on 300 cycles from experiments [108]. In the simulation, pressure traces and heat release rates from 30 consecutive cycles are displayed in the figure which show cycle to cycle variations. Figure 5-2 (b) shows a comparison of the averaged pressure traces, where the average computed pressure of thirty numerical cycles is compared to the average measured pressure of three hundred experimental cycles. The averaged pressure trace from the simulations matches the experimental pressure trace fairly well indicating good accuracy from the current model.

Figure 5-3 shows the comparison of spark current between the experiments and the simulations. Figure 5-3 (a) represents the experimental currents of 300 cycles with the yellow line

being the ensemble averaged current. Figure 5-3 (b) shows the current based on 30 simulation cycles. The ignition timing is -18 CA ATDC, which corresponds to 0 ms in experiments. When based on the rotation speed of 1300 rpm, the crank angle at -10 CA corresponding to 1.1 ms. In general, the magnitudes of the current from simulation cycles display the same order of the experimental current. Furthermore, the current shape of simulation cycles is also similar to that of the experimental current shape.

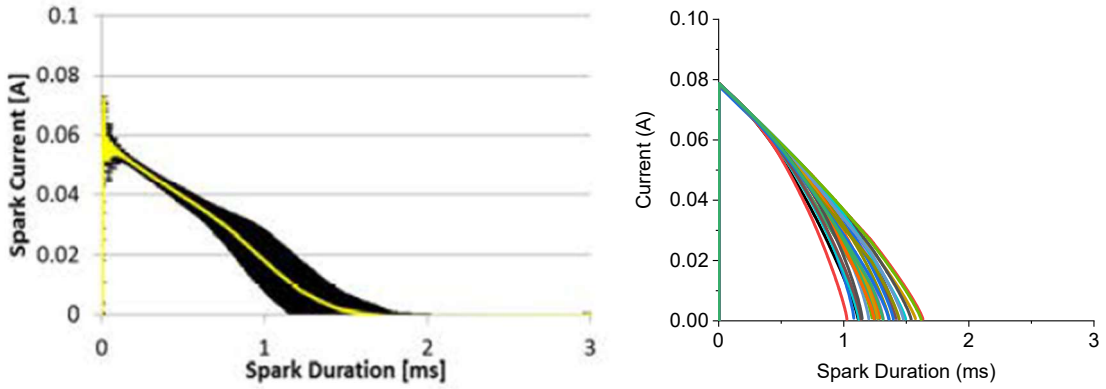

(a) (b)

Figure 5-3 Comparison of spark current between experiments and simulations ((a) current based on 300 cycles [108]; (b) current based on 30 simulation cycles)

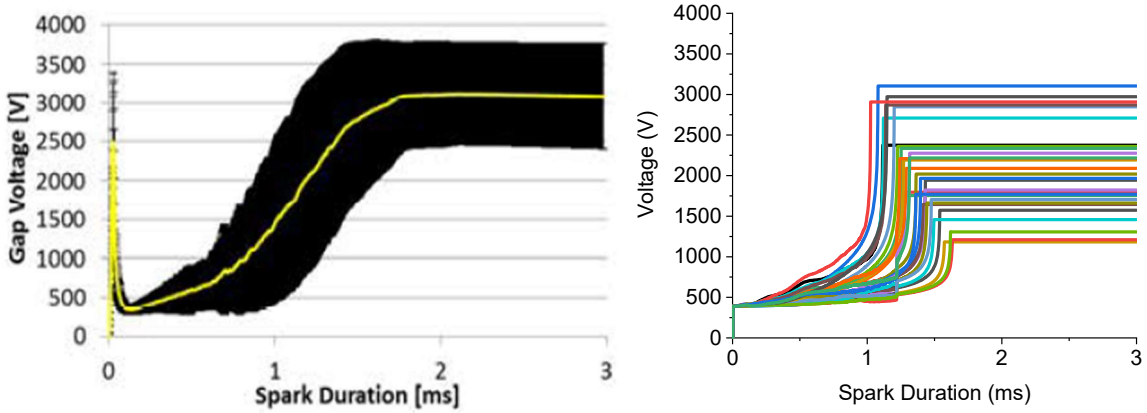

(a) (b)

Figure 5-4 Comparison of spark voltage between experiments and simulations ((a) voltage based on 300 cycles [108]; (b) voltage based on 30 simulation cycles)

Figure 5-4 displays the comparison of the spark voltage between the experiments and the simulations. Figure 5-4 (a) is the experimental voltages of 300 cycles with the yellow line being the ensemble averaged voltage. Figure 5-4 (b) is the voltage based on 30 simulation cycles. In general, the shapes of the voltage from simulation cycles are similar to those of experimental voltage. Additionally, the voltages of simulation cycles have the same order of magnitude as the experimental voltages. However, the simulation cycles show more apparent cycle to cycle voltage variations. Most cycles from experiments display the voltage magnitude at the end between 2400 V and 3600 V while the voltage magnitude at the end from simulation cycles is between1300 V and 3300 V. Moreover, there is no voltage jump at the ignition beginning in the simulations as the breakdown phase of ignition, which lasts about 1-10 ns, is not included in the WSSIM.

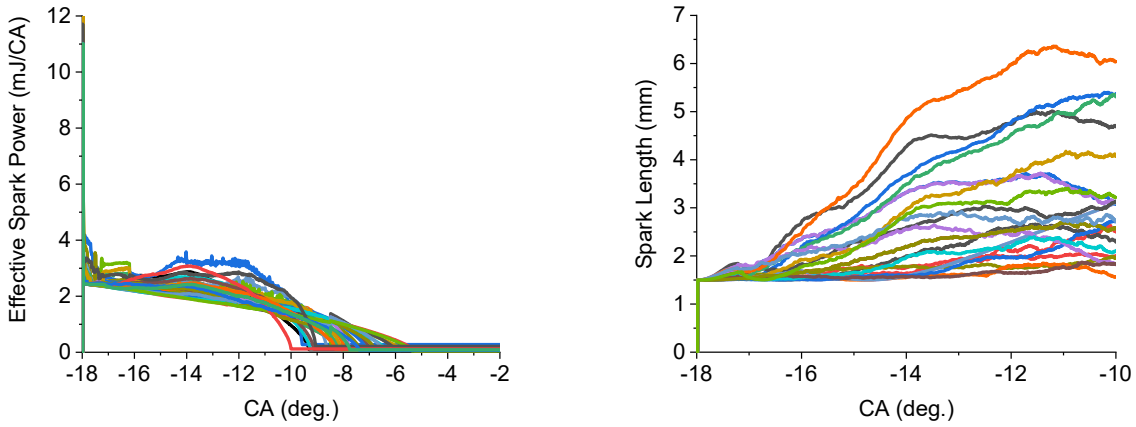

(a) (b)

Figure 5-5 The effective spark power and spark length from 30 simulation cycles ((a) effective spark power; (b) spark length)

Figure 5-5 (a) displays the effective spark power, the term $\eta V_{ie}(t) i_s(t)$ in Eqns. (3-65), (3-68), which is deposited to the propane/air mixture during the ignition process. The total initial energy input to the mixture is set to 30 mJ, which is consistent with experiments. It is clear that CCV occurs in the effective spark power based on the 30 simulation cycles. The reason is mainly due to

the variations in the current and the voltage, as displayed in Figure 5-4 and Figure 5-5. Besides this, the voltage calculation as Eqn. (3-54) is correlated with the spark length, as shown in Eqn. (3-55). Thus, the variations in voltage are caused by the variations in the spark length, which is displayed in Figure 5-5 (b). The calculation of spark length is described in Figure 3-20 and its length value is related to the convection effect of the local flow fields near the spark plug region.

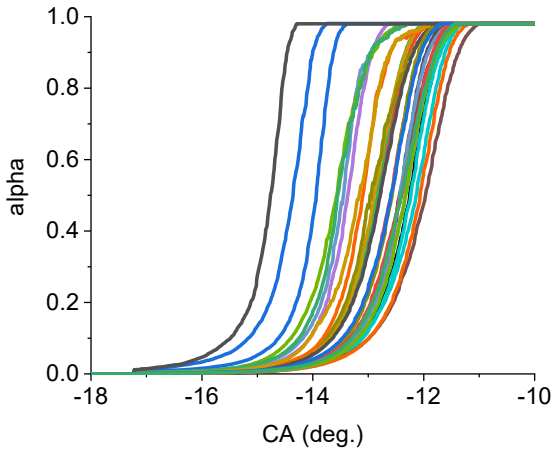

Figure 5-6 alpha transition function used for the flame propagation transition from nearly laminar to fully turbulent propagation

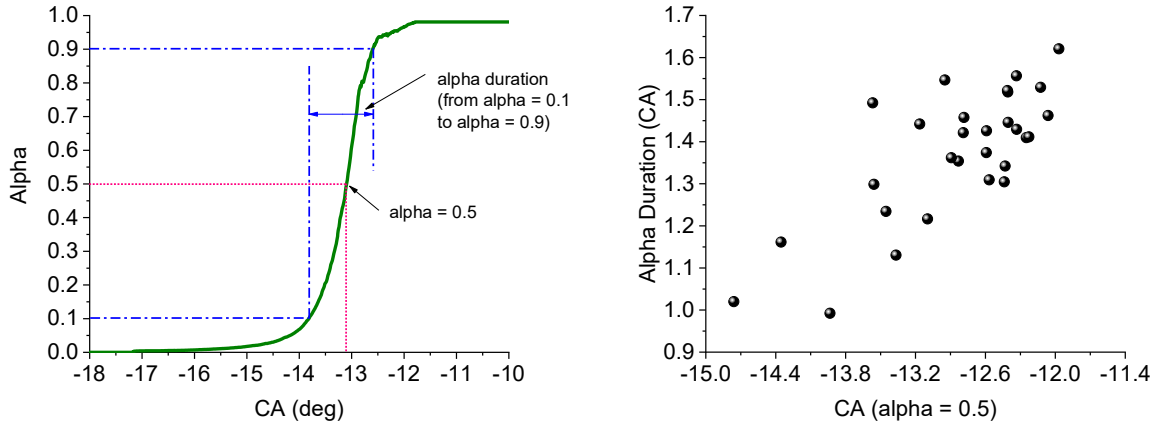

(a) (b)

Figure 5-7 Definition of alpha properties and relationship between those properties ((a) definition of $\alpha = 0.5$ and alpha duration; (b) relationship between alpha duration and $\alpha = 0.5$)

The alpha transition function, α, is calculated as shown Eqn. (3-64). This function changes the flame propagation speed from a nearly laminar flame speed when the flame kernel size is small (less than 1 mm) into a fully turbulent flame propagation speed as the kernel grows. The changing rate of α determines the rate at which the kernel propagation speed reaches the fully turbulent flame speed. Figure 5-6 represents the alpha transition functions for 30 simulation cycles, which shows variations from cycle to cycle. Two characteristics of the alpha transition function are calculated: one is the crank angle corresponding to $\alpha = 0.5$ and the other is the alpha duration, which is defined as the crank angle duration from $\alpha = 0.1$ to $\alpha = 0.9$ (Figure 5-7 (a)). In general, the earlier crank angle that $\alpha = 0.5$ occurs, then the shorter the alpha duration (Figure 5-7 (b)).

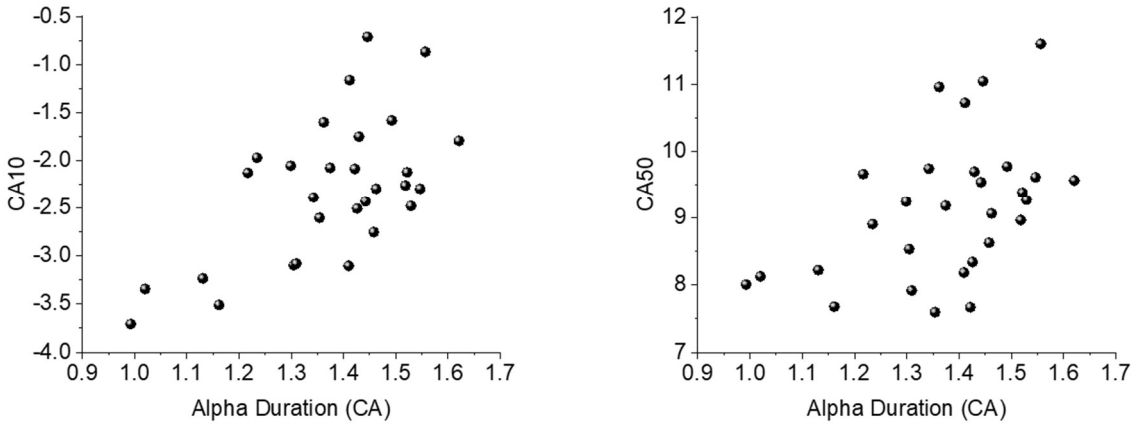

(a) (b)

Figure 5-8 Relationship among CA10, CA50 and alpha duration ((a) relationship between CA10 and alpha duration for 30 simulation cycles; (b) relationship between CA50 and alpha duration for 30 simulation cycles)

It is stimulating to study the relationship between the property of alpha transition function and the combustion, as the previous and following findings of this study support. Figure 5-8 shows the relationship among CA10, CA50 and alpha duration. Figure 5-8 (a) represents the relationship between CA10 and alpha duration for 30 simulation cycles. Figure 5-8 (b) demonstrates the relationship between CA50 and alpha duration for 30 simulation cycle. In general, shorter alpha

duration lead to an earlier CA10 and CA50. This result is reasonable since a shorter alpha duration indicates faster kernel growth rate (radius term in Eqn. (3-64)), which further denotes that the flame propagation speed is relatively bigger, as shown in Eqn. (3-58) and Figure 5-9 (a).

Figure 5-9 (a) compares the plasma velocity s_p with the turbulent burning velocity s_T for the 30 simulation cycles. As the figure illustrates, the value of plasma velocity s_p calculated in Eqn. (3-66) and (3-68) is more than four times bigger than that of turbulent burning velocity s_T when calculated using Eqn. (3-31), therefore demonstrating that s_p dominates the kernel growth at the start of ignition. Over time, s_T becomes one order larger than s_p, so s_T dominates the combustion process. Besides, the s_T values become nearly constant (about 4 to 5 m/s) between -12 CA to -11 CA, which signifies that the alpha transition function stops working. Due to the CCV in flame propagation speed, the kernel growth rates also show CCV, as displayed in Figure 5-9 (b).

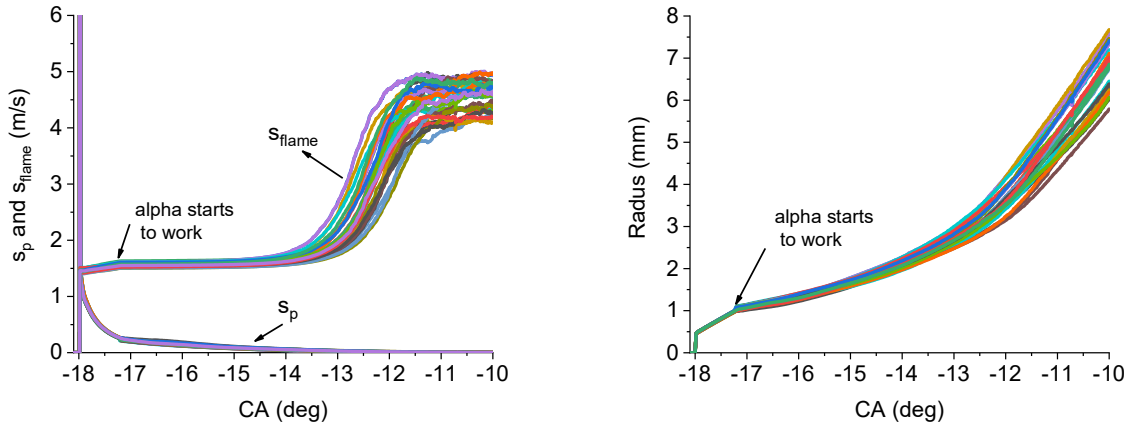

(a) (b)

Figure 5-9 Flame propagation speed and kernel radius for the 30 simulation cycles ((a) Plasma velocity s_p and flame propagation velocity s_{flame}; (b) kernel radius)

As mentioned in Section 5.1, it is imperative to guarantee that the ratio of the curvature inverse to mesh size is greater than 1 in order to capture the kernel surface for the mesh. Figure 5-10 shows the ratio of the inverse of curvature to the filter size where the filter size is the local mesh resolution.

Seven random cycles are chosen to display that ratio where the ignition timing is -18 CA ATDC. It is apparent that the ratio is greater than 1 at the start of ignition and then becomes larger as the ignition continues, thus designating that the mesh resolution can capture the kernel curvature. In addition, the ratio of curvature inverse to mesh size shows a linear relationship with a crank angle, and then followed by a non-linear part, which is explained through Figure 5-9 (b). In this figure, the radius, equivalent to the curvature inverse in values, grows linearly with a crank angle before the alpha transition functions starts working. At this point, the mesh size is about 0.3 mm during the period between the start of ignition and when the alpha starts to work. Thus, the ratio of curvature inverse to mesh size increases linearly. As the alpha transition function starts working, which is not linear as shown in Figure 5-6, the kernel growth does not stay in a linear relationship with the crank angle. This leads to a non-linear growth of ratio of the curvature inverse to the mesh size.

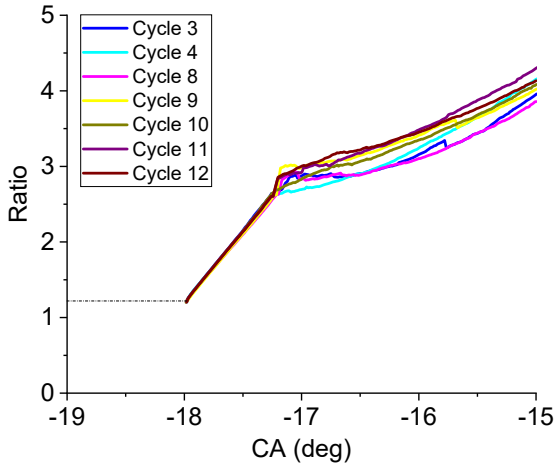

Figure 5-10 The ratio of the curvature inverse to mesh size for seven cycles

5.2.2 Sensitivity Tests

From the variations in pressure traces, HRR, current, etc., it is necessary to investigate the effects of some variables on the combustion. Three representative simulation cycles were chosen

and will be explored in more details: the high case (simulation05 with CA10 = -3.60 CA ATDC), the medium case (simulation29 with CA10 = -2.12 CA ATDC), and the low case (simulation05 with CA10 = -0.71 CA ATDC). These were chosen based on their CA10 values (Figure 5-11).

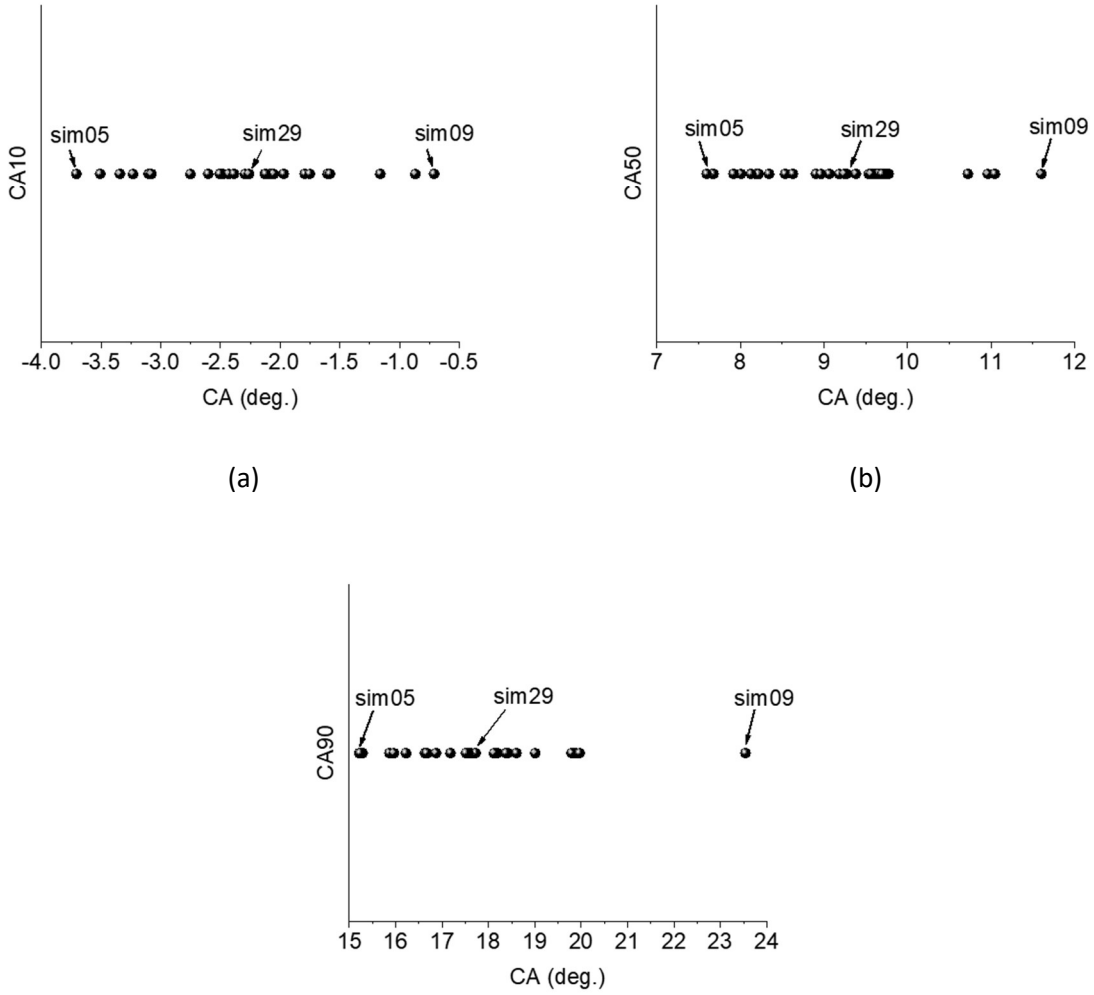

Figure 5-11 CA10, CA50, and CA90 for 30 simulation cycles ((a) CA10; (b) CA50; (c) CA90)

Table 5-3 Initial global averaged subgrid kinetic energy k_{sgs}, temperature T, and equivalence ratio ϕ for high, medium, and low simulation cycles at IVC (-110 CA ATDC)

Global Averaged	High (sim05)	Medium (sim29)	Low (sim09)
ksgs (m^2/s^2)	4.027	4.279	3.159
T (K)	715.637	712.304	711.117
ϕ	0.99747	0.99739	0.99739

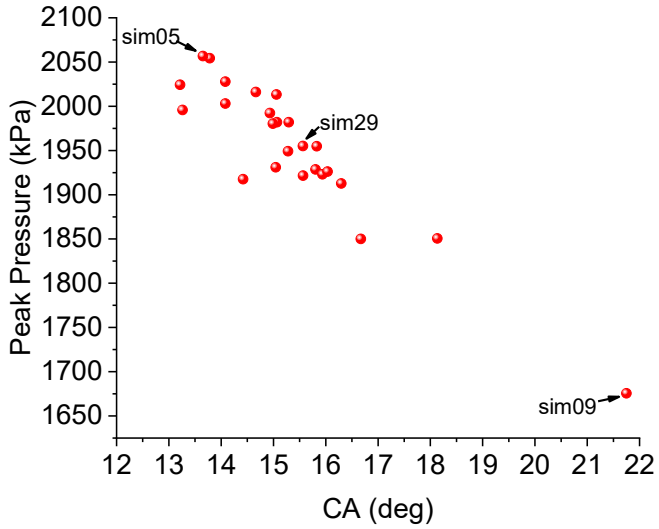

Figure 5-12 Peak pressures and corresponding crank angels for 30 cycles with high (sim05), medium (sim29), and low (sim09) being labeled

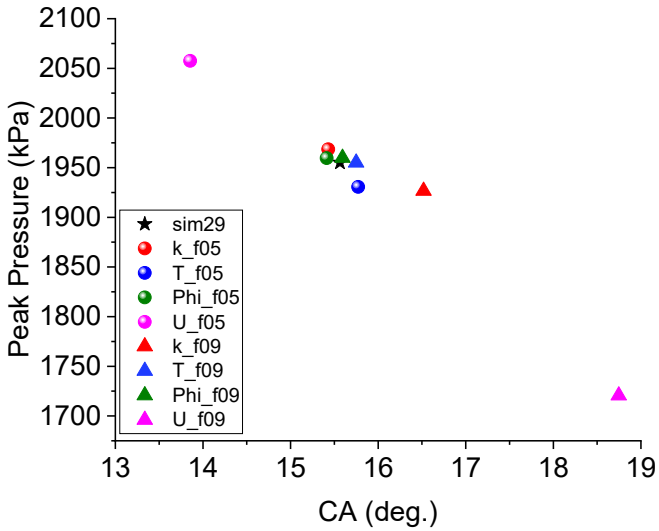

Figure 5-13 Sensitivity tests (Set the medium case sim29 as the base case and replace its k_{sgs}, T ϕ, and U from high case sim05 and low case sim09

Table 5-3 shows that the initial global averaged subgrid kinetic energy k_{sgs}, temperature T, and the equivalence ratio ϕ for these three simulation cycles at -110 CA ATDC corresponding to the IVC point. As seen from the table, the high case has a relatively higher temperature; the medium case displays higher subgrid kinetic energy k_{sgs}; and the low case shows lower k_{sgs} and

T when compared with the high and medium cases. The equivalence ratio is extremely close among the three representative cases.

In Figure 5-12, the crank angle corresponds to the peak pressure of 30 simulation cycles where the high (sim05), medium (sim29), and low (sim09) are indicated. Figure 5-13 displays the test where the medium case sim29 is set as the base case (the black star in Figure 5-13) and its replace is k_{sgs}, T, ϕ, and the velocity field U from high case sim05 and low case sim09. For instance, the label "k_f05" means to take the k_{sgs} from sim05 and to replace the k_{sgs} of sim29. The label "U_f09" means to take the velocity field U from sim09 and to replace the velocity field U of sim29. It can be seen that changing the equivalence ratio ϕ has a small effect on combustion while changing the U has the most significant effect on combustion.

Figure 5-14 shows the CA10, CA50, and CA90 after replacing the k_{sgs}, T , velocity field (U), and ϕ of medium case sim29 from high case sim05 and low case sim09. Again, changing the velocity field U of sim29 with sim05 advances the CA10 (Figure 5-14 (a)), CA50 (Figure 5-14 (b)), and CA90 (Figure 5-14 (c)) while changing the velocity field U of sim29 with sim09 delays the CA10, CA50 and CA90. In addition, replacing U exerts more apparent effect on CA10, CA50, and CA90 while negligible changes for CA10, CA50, and CA90 occur when replacing the equivalence ratio. This result indicates the velocity field needs further investigation to display the difference from cycle to cycle. On the other hand, it is reasonable that the equivalence ratio displays a slighter effect on CA10, CA50, and CA90 since the equivalence ratios are very close among sim05, sim29, and sim09, and the TCC3 engine propane/air mixture is approximately homogeneous. Moreover, replacing the k_{sgs} and T of sim29 with that of sim05 advances the CA10, CA50, and CA90 while delaying with the k_{sgs} and T of sim09. One interesting phenomenon is that even though the global averaged temperature of sim05 is smaller than that of

sim29, it still advances the CA10, CA50, and CA90. Thus, one needs to analyze the local values of k_{sgs} and T near the spark plug region since those local values are incorporated into the wrinkling factor, turbulent burning velocity, and laminar burning velocity, as shown in Eqns. (3-60), (3-31) and (3-27), which further affects the kernel growth rates.

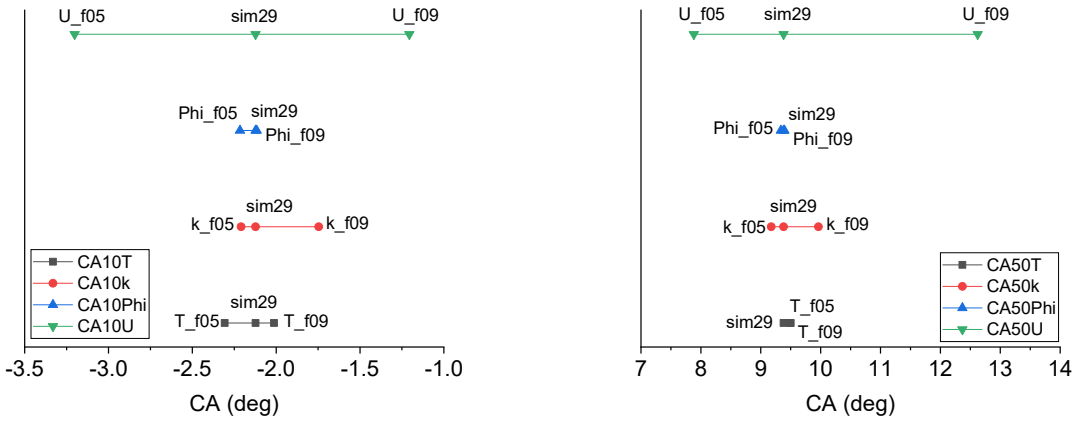

(a) (b)

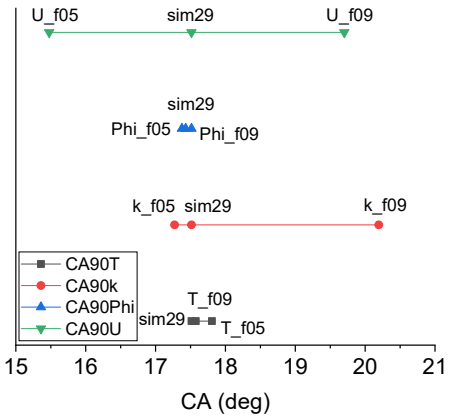

(c)

Figure 5-14 CA10, CA50, and CA90 after replacing the k_{sgs}, T and ϕ of medium case sim29 from high case sim05 and low case sim09 ((a) CA10; (b) CA50; (c) CA90)

Figure 5-15 represents the subgrid kinetic energy k_{sgs} contours and k_{sgs} on a line passing through the spark gap at -20 CA ATDC, which is 2 crank angles before the start of ignition on the

cut plane passing the spark ignition location. From the contour plot (Figure 5-15 (a)), sim29 shows a stronger k_{sgs} field when compared with sim05 and sim09. However, the k_{sgs} value of sim05 on the axis, especially near the spark ignition, known as the center point on the axis, is stronger than sim29 and sim09. The flame kernel development is divided into two phases: the Lagrangian phase and the Eulerian phase, as indicated in Figure 3-18. In the Lagrangian phase, the flame propagation speed is calculated as the product of the wrinkling factor and the laminar flame speed as Eqn. (3-50) while k_{sgs} is implicitly included in the wrinkling factor through the turbulent viscosity ν_t.

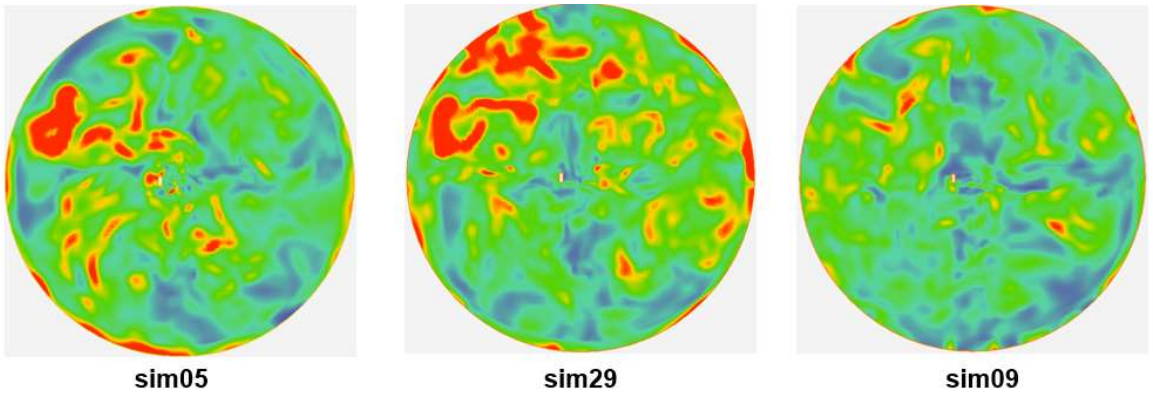

(a)

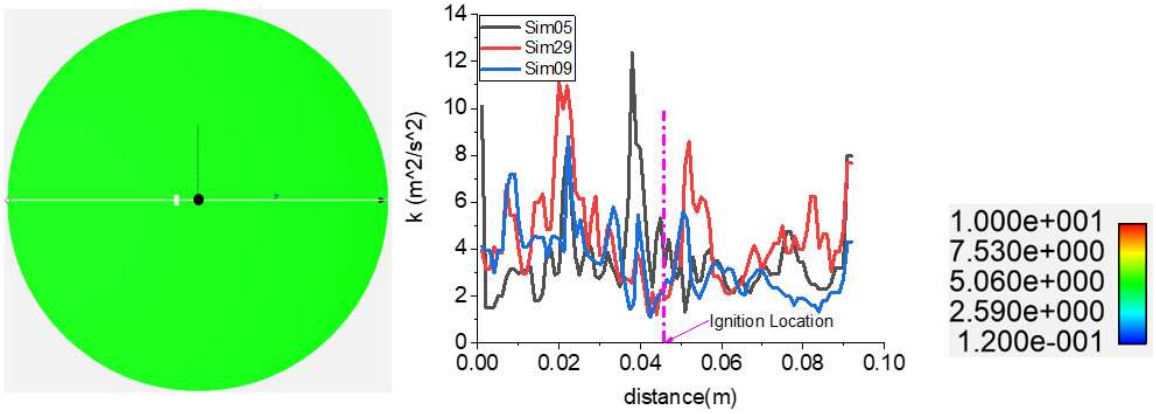

(b)

Figure 5-15 Subgrid kinetic energy k_{sgs} contours and k_{sgs} on the axis at -20 CA ATDC on the cut plane passing the spark ignition location ((a) k_{sgs} contours on the cut plane; (b) k_{sgs} on the line passing the ignition location (the black dot) as indicated by the white line in the figure to the left)

Figure 5-16 displays the wrinkling factors for the high (sim05), the medium (sim29), and the low (sim09) cycles. It can be seen from the figure that the wrinkling factor is bigger in the case of (sim05) with a local higher k_{sgs} value (about 5 m^2/s^2) and smaller for the case (sim09) with a local lower k_{sgs} value (about 2 m^2/s^2). In addition, the values of the wrinkling factor stop increasing after a short crank angle duration. This is the point at which the flame kernel radius reaches the transition radius, which is 1 mm in current study. Also, this is the point when the wrinkling factor stops working and the alpha transition function starts to work. Moreover, the wrinkling factor stops working a little earlier for case with a stronger local k_{sgs} value near the spark plug. The effect of k_{sgs} on combustion in Eulerian phase is integrated in the turbulent burning velocity s_T as Eqn. (3-31). Thus, a stronger k_{sgs} field indicates a bigger value of s_T, which promotes the flame kernel growth.

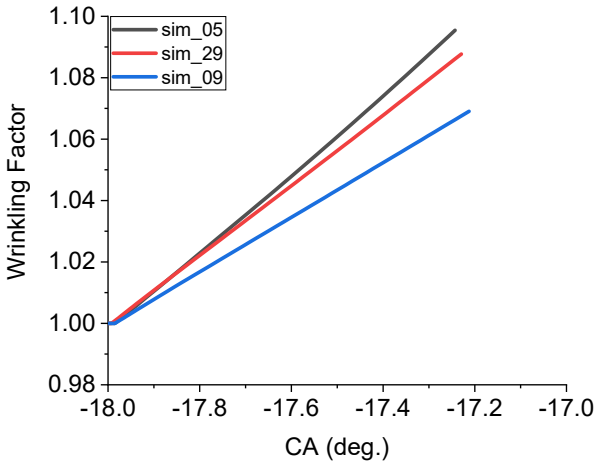

Figure 5-16 Wrinkling factor for high (sim05), medium (sim29) and low (sim09) cycles (the wrinkling factor stops working once it stop increasing at which the alpha transition function starts to work)

Figure 5-17 shows the temperature contours and the temperature on the axis at -20 CA ATDC, which is 2 crank angles before the start of ignition on the cut plane passing the spark ignition location. Higher temperatures occur near the spark plug region due to the temperature of the spark

plug set at 900 K. However, the temperature of sim05 is higher than that of sim29 and sim09 near the spark plug, therefore leading to a higher laminar burning velocity which further contributes to a higher flame propagation speed by combining with the wrinkling factor, as shown in Eqn. (3-50). In the Eulerian phase, higher temperatures indicate a bigger laminar burning velocity and turbulent burning velocity.

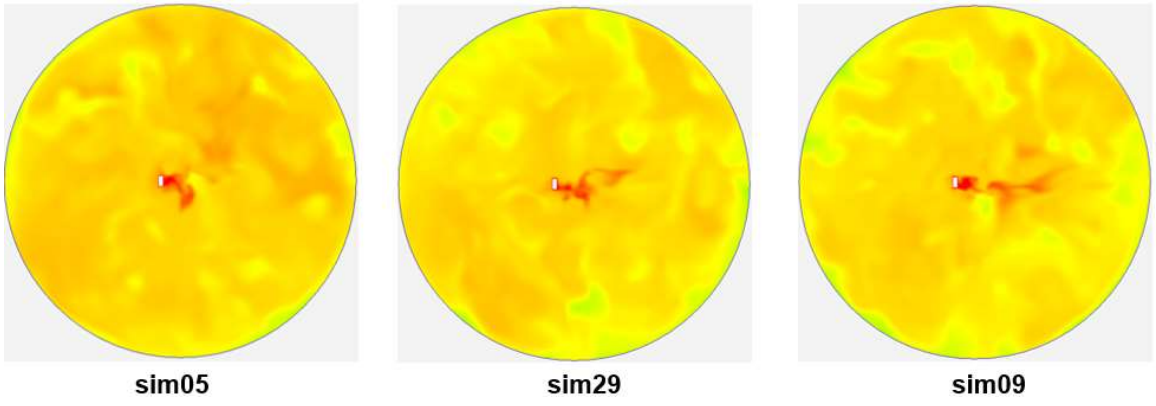

(a)

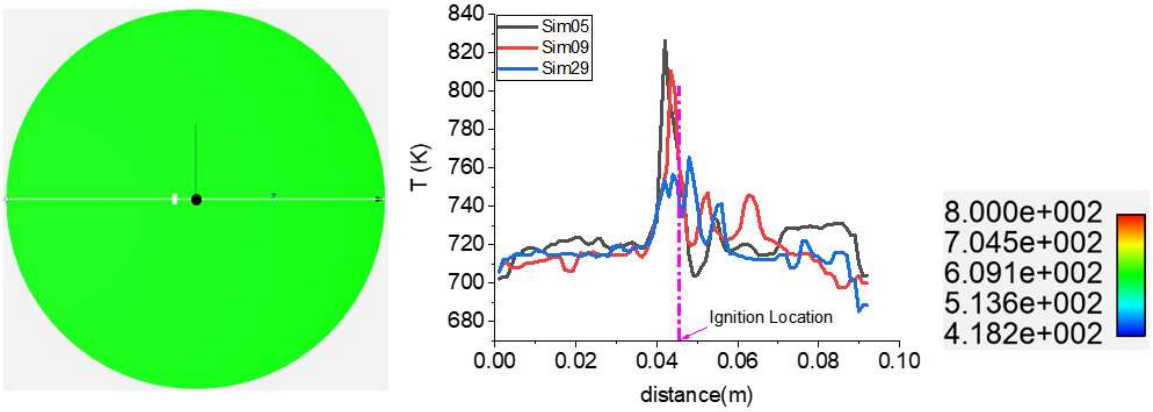

(b)

Figure 5-17 Temperature contours and temperature on the axis at -20 CA ATDC on the cut plane passing the spark ignition location ((a) temperature contours on the cut plane; (b) temperature on the line passing the ignition location (the black dot))

As mentioned above, velocity exerts more significant effect on combustion. Therefore, it is worth digging into the velocity fields among cycles. Besides, it is useful to study how the flame surface (G = 0 isosurface) correlates with the flow fields at early crank angles. Figure 5-18

illustrates the flow fields and $G = 0$ flame front (red curve) of sim05, sim29, and sim09 at CA = 348 and CA = 354 corresponding to 6 crank angle and 12 crank angles after the start of ignition. The figures correspond to images from experimental work [119] and are a cut plane passing the ignition location from the top view with each side 60 mm with the spark plug at the center.

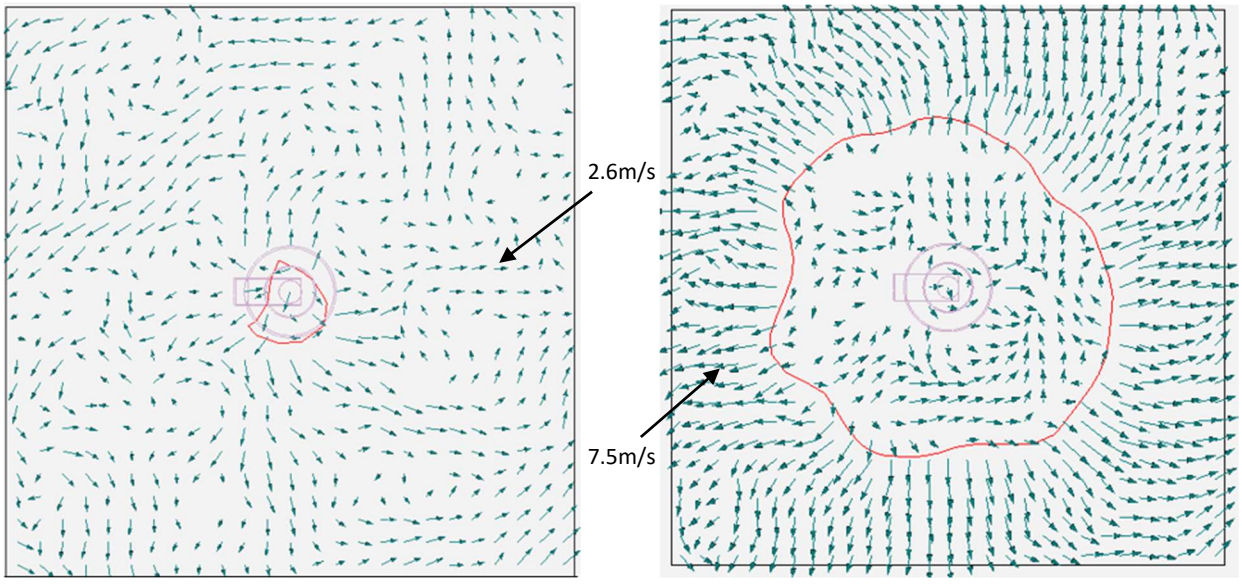

CA = 348 CA = 354

(a) High (sim05)

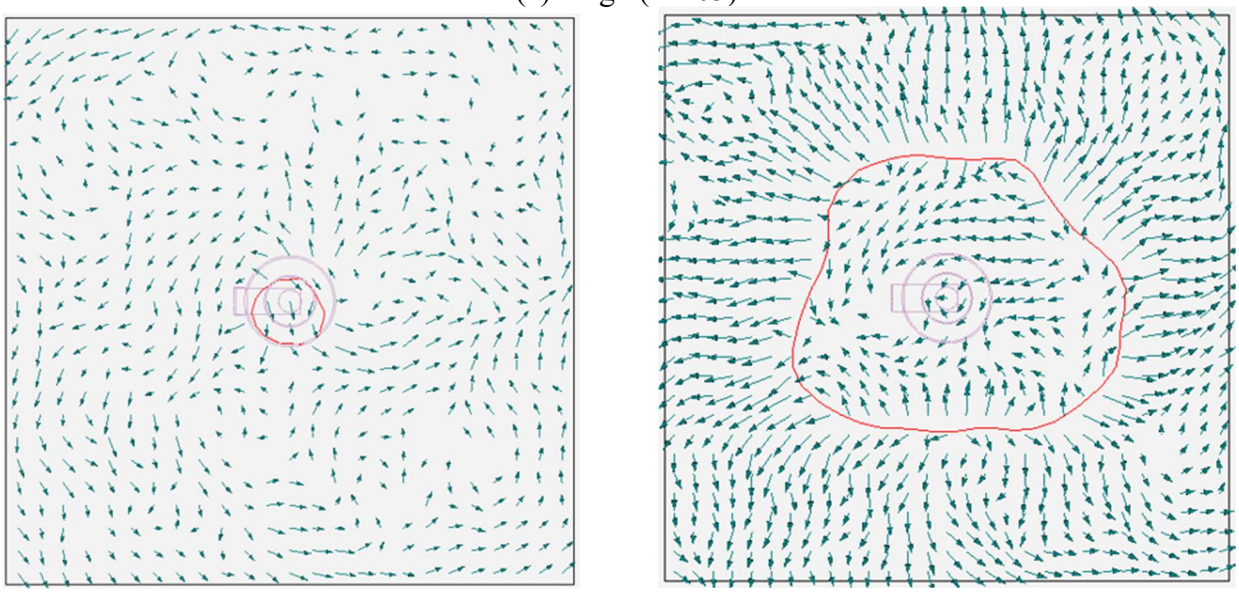

CA = 348 CA = 354

(b) Medium (sim29)

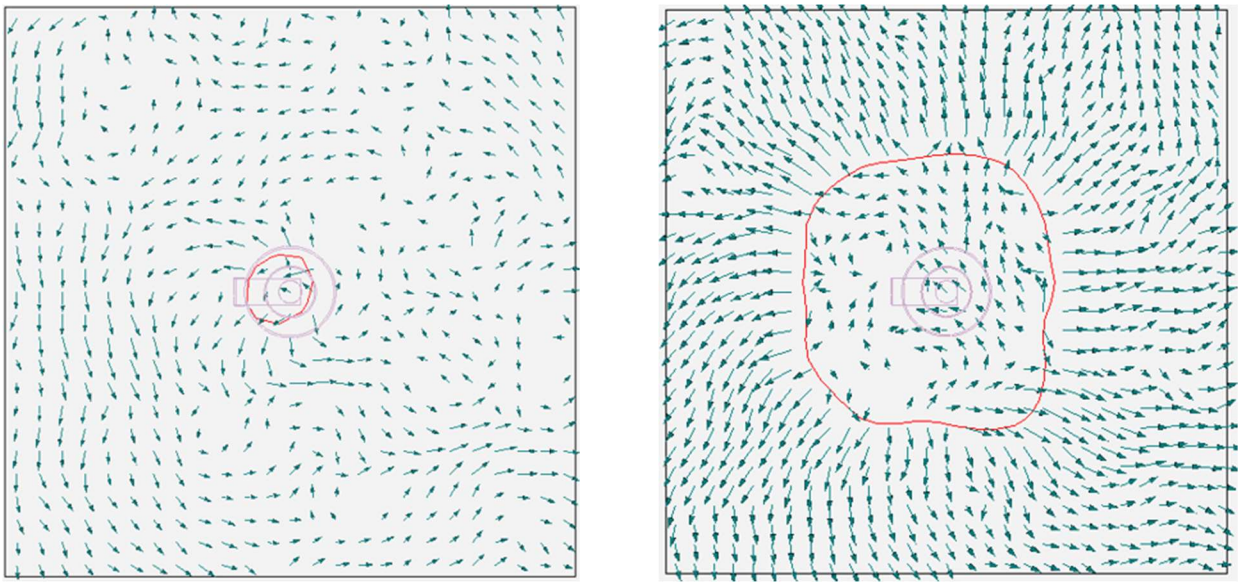

CA = 348 CA = 354

(c) Low (sim09)

Figure 5-18 Velocity fields and $G = 0$ flame front (red curve) of sim05, sim29, and sim09 at CA = 348 and CA = 354 ((a) sim05; (b) sim29; (c) sim09)

In Figure 5-18, only the velocities with magnitude between 1.1 m/s to 65 m/s are displayed, which is consistent with the experiments [119]. As it is indicated in Figure 5-18, the flow field at CA = 348 near the spark plug spreads in all directions for the high case (sim05) while the flow field for low case (sim09) is weaker on the top right of Figure 5-18 (c) at CA = 348. Two velocity scales, 2.6 m/s and 7.5 m/s, are labeled in Figure 5-18 (a). Thus, when compared with the laminar burning velocity with magnitude around 0.8 m/s for stoichiometric propane/air combustion, the velocity fields are one order bigger than the laminar burning velocity. Moreover, it can be seen from Figure 5-18 (a) that even though the $G = 0$ flame front (red curve) is not a perfect circle at CA = 348, its shape becomes relatively symmetric at CA = 354 due to the velocity direction spreading out in all directions at CA = 348. But, for the low case (sim09), its velocity field at CA = 348 does not point to all directions, hence leading to a non-symmetric $G = 0$ flame front at CA = 354. Finally, the velocity fields propagate outward due to the dilatation effect of flame growth and propagation at CA = 354, at which the flame propagation dominates the process.

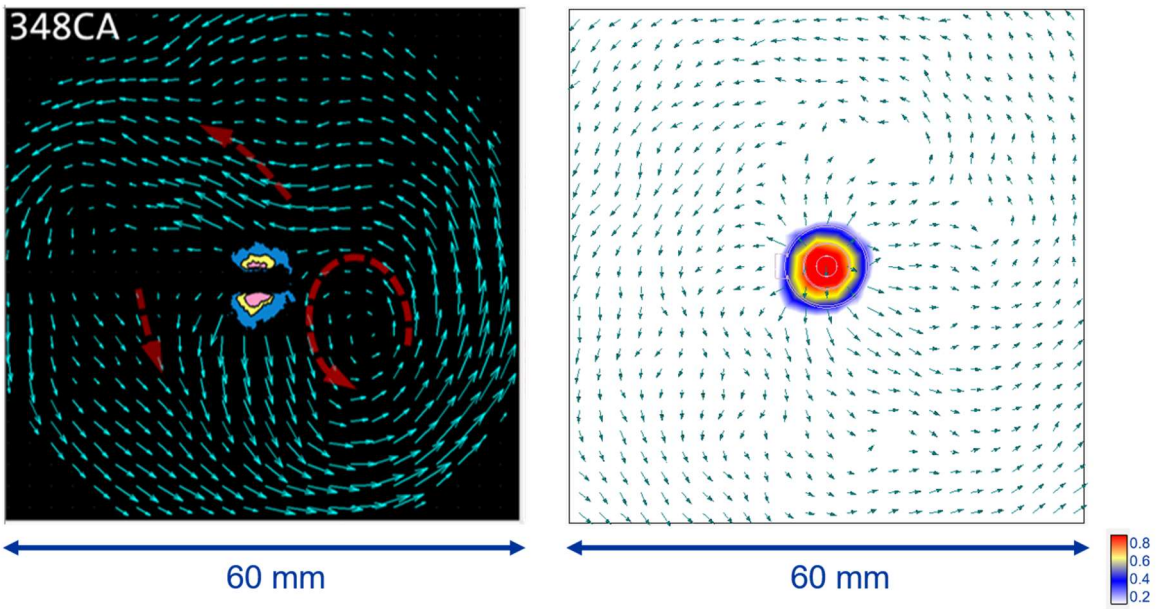

(a) Averaged fast cycles (left: experiments (80 cycles) [119]; right: simulation (8 cycles))

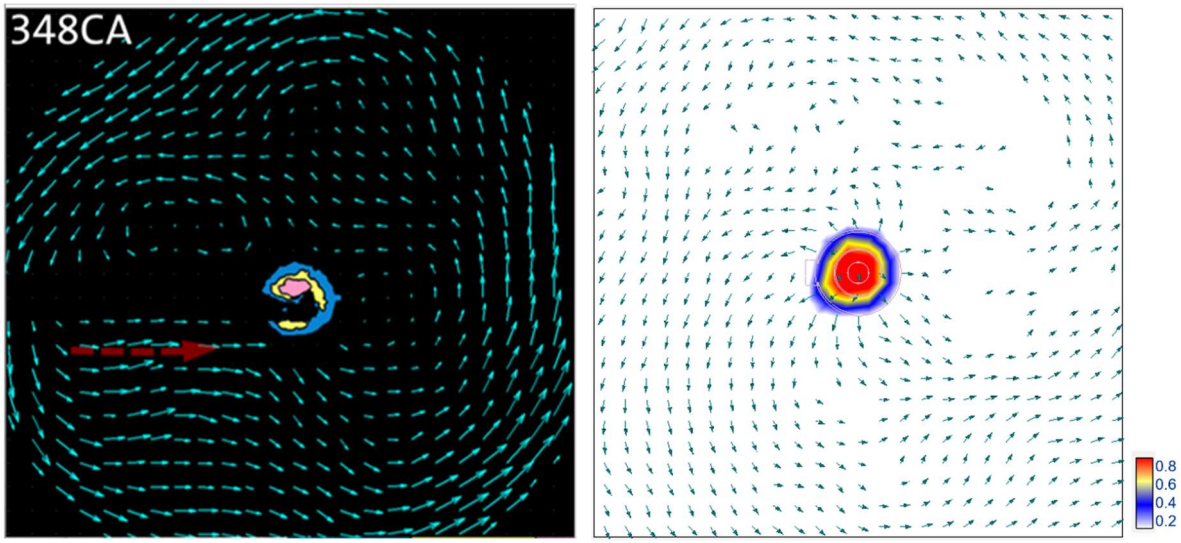

(b) Averaged slow cycles (left: experiments (80 cycles) [119]; right: simulation (8 cycles))

Figure 5-19 Comparison of averaged velocity field and burnt probability between experiment and simulation cycles at CA = 348 ((a) averaged fast cycles; (b) averaged slow cycles)

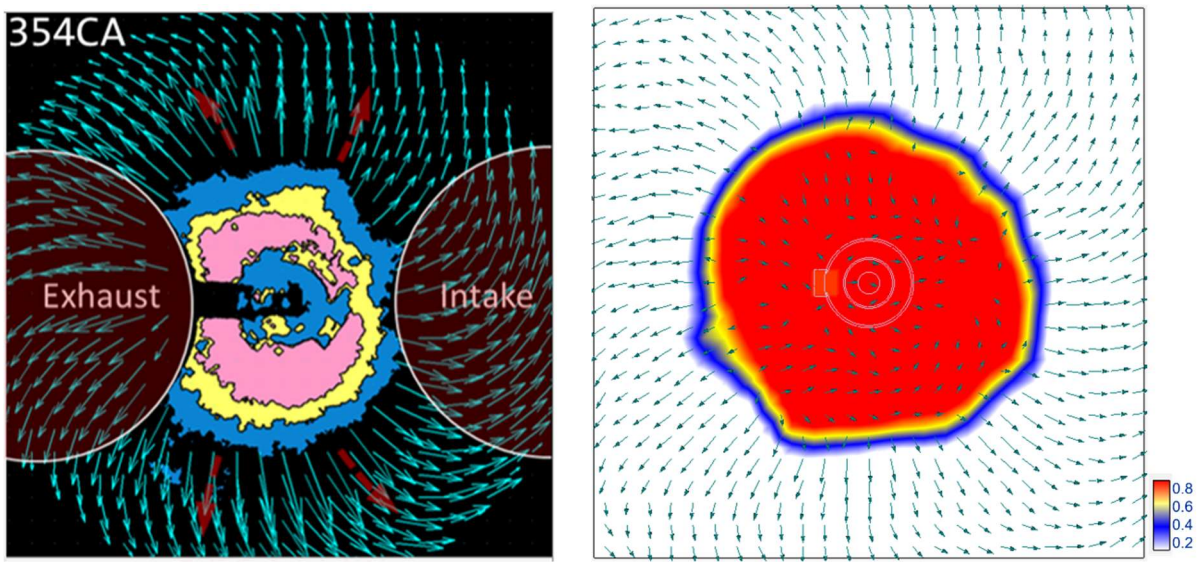

(a) Averaged fast cycles (left: experiments (80 cycles) [119]; right: simulation (8 cycles))

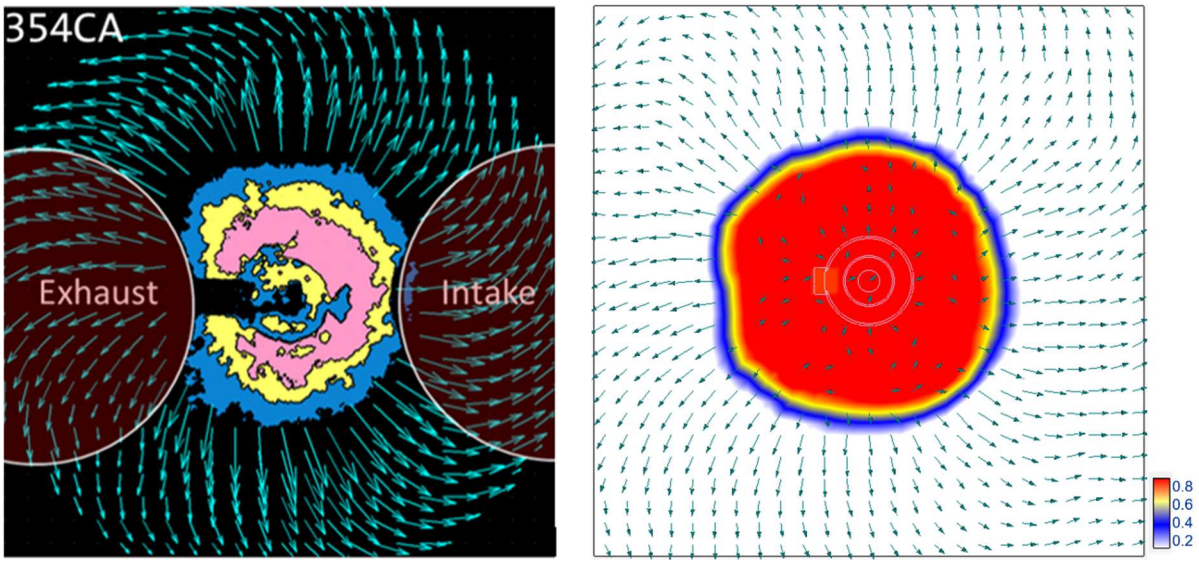

(b) Averaged slow cycles (left: experiments (80 cycles) [119]; right: simulation (8 cycles))

Figure 5-20 Comparison of averaged velocity field and burnt probability between experiment and simulation cycles at CA = 354 ((a) averaged fast cycles; (b) averaged slow cycles)

Figure 5-19 and Figure 5-20 display the averaged velocity field and the burnt probability between the experiment and the simulation cycles at CA = 348 and CA = 354. Velocities only with magnitude from 1.1 m/s to 65 m/s are shown for both the experiments and the simulations. In the experiments, silicon oil is used to capture the flame [119] and to calculate the burnt probability. In

the simulation, the flame probability calculation for a certain cell is based the occurrence of G > 0 among 8 chosen cycles. The flame probability of one cell would fall into the 80% region if G > 0 occurs greater than or equal to at least seven times among the eight cycles. It would fall into the 60% region if G > 0 occurs greater than or equal to four but less than seven times among the eight cycles. Several phenomena can be observed from these two figures. First, for the averaged fast cases at CA = 348 in Figure 5-19 (a), the velocity direction is the same direction as the experiments on the left side, which is the exhaust valve region. However, on the right side, known as the intake value region, the averaged simulation cycles do not show an apparent vortex as the experiments, which might be due to the fact that only 8 cycles are averaged instead 80 cycles as in the experiments. Second, when compared with the averaged fast simulation cycles at CA = 348, the averaged slow simulation cycles at CA = 348 (Figure 5-19 (b)) shows weaker velocity fields, especially at the right side which is the intake valve region. Third, the flow fields directions for both experiments and simulations are dominated by the flame propagation at CA = 354, as illustrated in Figure 5-20. Fourth, the flame probability from the simulations display similar contour plots to the experiments for both the averaged fast and slow cases at CA = 348. Note that the burnt probability does not show lower values (0.2) near the spark plug region at CA = 354 for both the averaged fast and slow cases of simulations. This phenomena is due to the operation in the experiments where the low probability maps of the center in experiments were caused by the low signal-noise-ratio with the noise being from the reflection [119].

5.2.3 Effect of Transition Radius

The stoichiometric combustion results, shown in Section 5.2.2, use a transition radius setting of 1 mm. The transition radius is when the wrinkling factor stops working and the alpha transition

function starts to work (see Eqns. (3-59) and (3-63)). In this section, two more transition radius, 2 mm and 3 mm, are investigated to illustrate the effects on combustion.

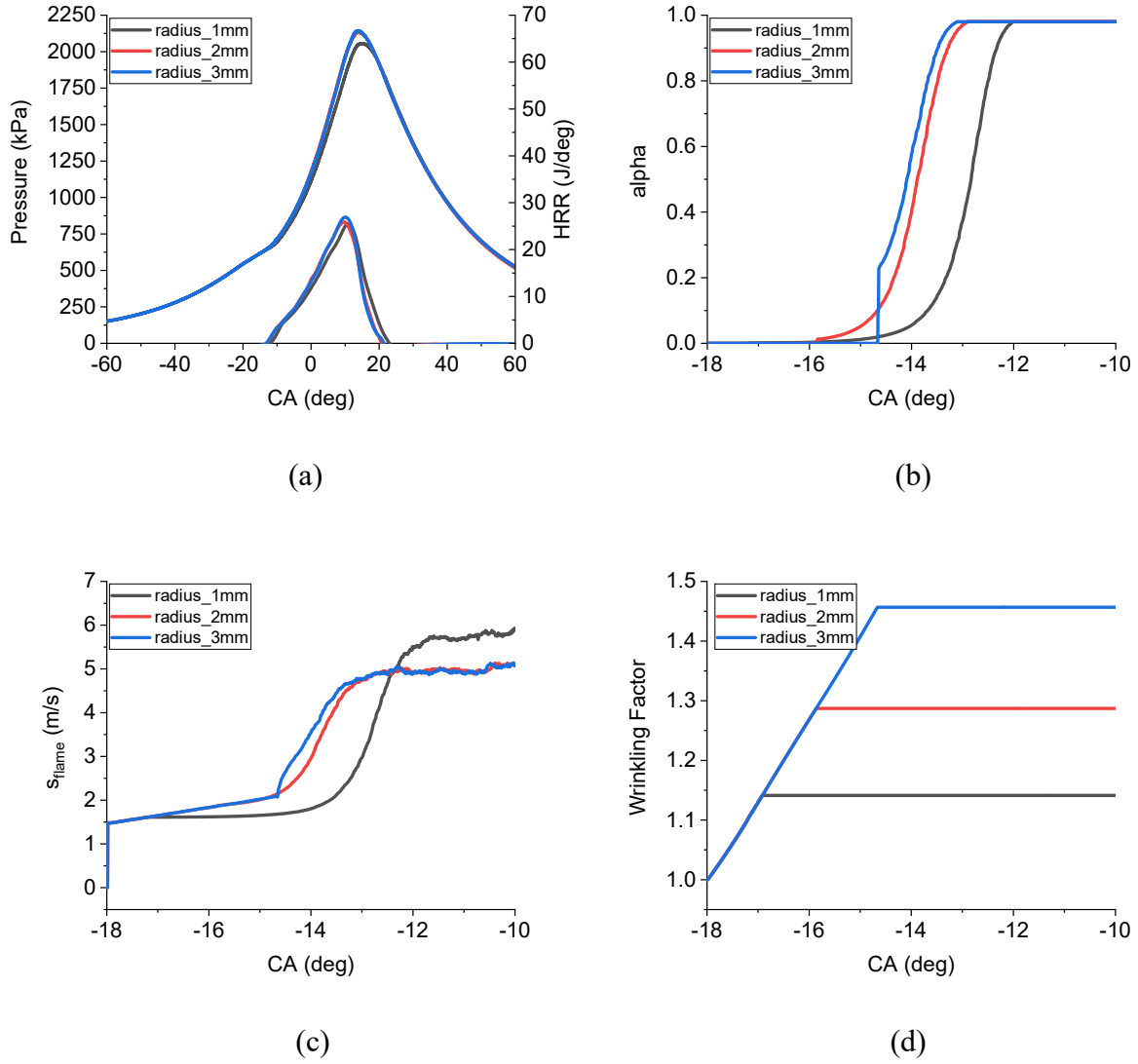

Figure 5-21 Effect of transition radius on combustion ((a) pressure trace and heat release rate; (b) alpha transition function; (c) turbulent burning velocity; (d) wrinkling factor)

Figure 5-21 elucidates the effect of the transition radius on combustion. As seen from Figure 5-21 (a), changing the transition radius from 1 mm to 2 mm results in a higher and advanced pressure trace and heat release rate, while changing the transition radius from 2 mm to 3 mm does

not show as much of an effect on pressure traces and heat release rate. An explanation for this phenomenon can found from Figure 5-21 (b) and (c). Figure 5-21 (b) displays that changing the transition function from 1 mm to 2 mm advances the flame propagation speed to a fully turbulent flame propagation speed ($\alpha = 1$) much more quickly than changing from 2 mm to 3 mm. This indicates that changing the transition radius from 1 mm to 2 mm increases the value of turbulent burning velocity much more effectively than changing from 2 mm to 3 mm, which is consistent with the result of Figure 5-21 (b). Another thing to point out is that the role that the wrinkling factor plays in comparison to the role that the alpha transition function plays. For instance, the wrinkling factor stops working and the alpha transition function starts to work at 1 mm if the transition radius is set to be 1 mm. However, the wrinkling factor continues to work until the kernel radius is 2 mm if the transition radius is set to be 2 mm. The latter causes a higher peak pressure, which indicates that the wrinkling factor exerts a larger effect on the flame speed than the alpha transition function from kernel size of 1 mm to 2 mm.

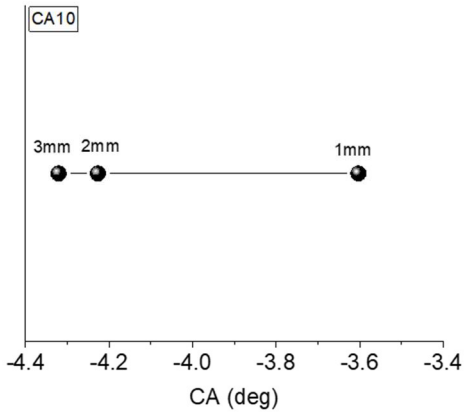

(a)

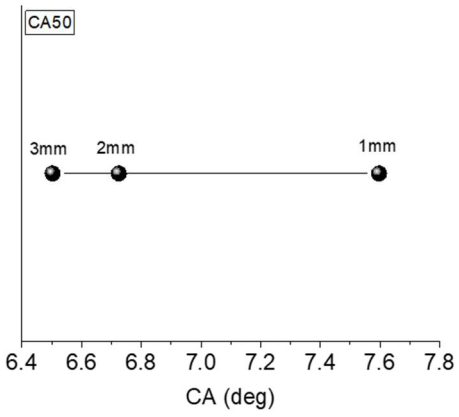

(b)

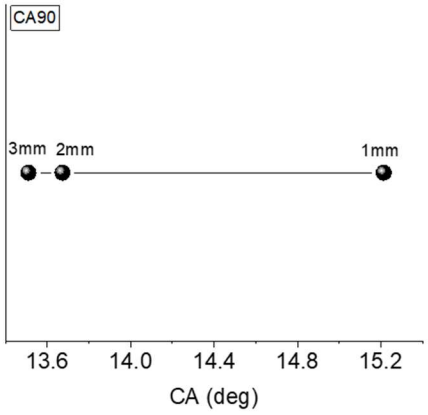

(c)

Figure 5-22 CA10, CA50, and CA90 based on transition radius of 1 mm, 2 mm, and 3 mm ((a) CA10; (b) CA50; (c) CA90)

Figure 5-22 showcases the CA10, CA50, and CA90 based on transition radius of 1 mm, 2 mm, and 3 mm. The results from Figure 5-22 are consistent with the phenomena in Figure 5-21: First, changing the transition radius from 1 mm to 2 mm and 3 mm advances the combustion resulting in earlier CA10, CA50, and CA90. Second, setting the transition radius from 1 mm to 2 mm has a greater effect than that of changing the transition radius from 2 mm to 3 mm. Thus, the extent that CA10, CA50, and CA90 advances from 1 mm to 2 mm is greater than that from 2 mm to 3 mm.

5.2.4 Effect of Spark Kernel Convection

In the previous sections, the kernel is initialized at the spark ignition location and then is convected by the flow fields. The effects of setting the ignition kernel to be fixed at the ignition location are explored, which this section exhibits. Two simulation cycles, sim13 and sim16, are chosen as the objects of study and the transition radius is set to be 1 mm.

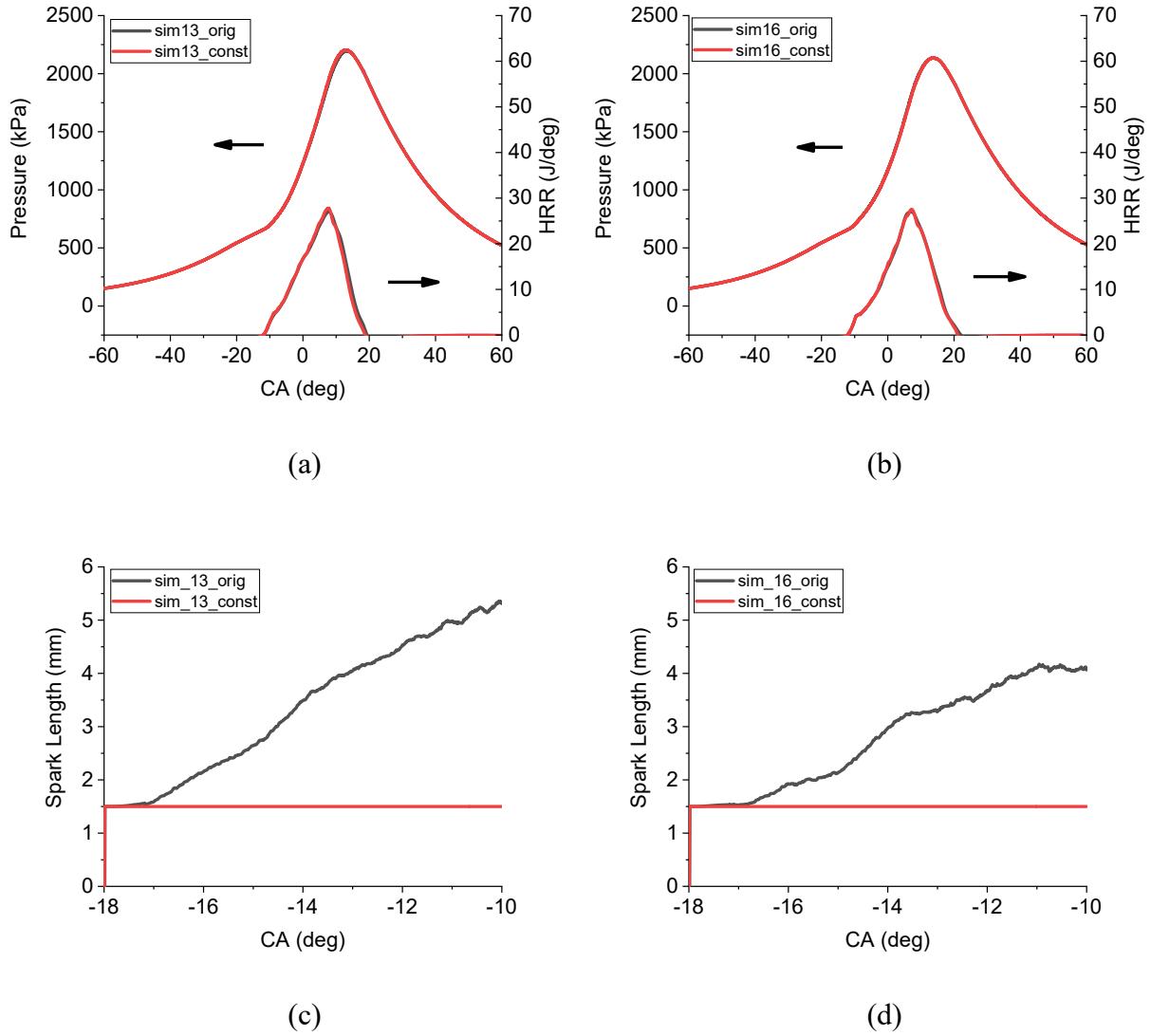

Figure 5-23 Effect of keeping kernel center unchanged on combustion ((a) pressure trace and HRR for sim13; (b) pressure trace and HRR for sim16; (c) spark length of sim13; (d) spark length of sim16)

As shown in Figure 5-23 is the effect of keeping the kernel center unchanged on the combustion for sim13 and sim16. In Figure 5-23, "sim13_orig" is the original case where the kernel is convected by the local flow for sim13, while "sim13_const" is the case where the kernel center is fixed at the ignition location. The same labeling applies for "sim16_orig" and "sim16_const." It is evident that fixing the kernel location at the ignition location does not affect the combustion from the pressure trace and HRR for both sim13 and sim16 (Figure 5-23 (a) and

(b)), even though the spark length does not change for "sim13_const" and "sim16_const." This indicates that the energy from the electric circuit is not important anymore once the kernel can sustain its growth through the heat release from the chemical reactions.

5.2.5 Effect of Fuel on Combustion

In this section, the effect of fuel chemical energy deposition is investigated during ignition processes when electrical spark energy is being deposited. This is performed under conditions of fuel and non-fuel with other variables staying constant. Once again, sim13 and sim16 are the chosen study cases, and the transition radius is set to 1 mm.

Figure 5-24 displays the effect of fuel on energy deposition. In Figure 5-24, "sim13_orig" is the original case where propane exists for sim13, while "sim13_W/O_fuel" is the case where only the air is in the cylinder. The label applies for "sim16_const" and "sim16_W/O_fuel." As shown in the figure, it takes more time to deposit all the electric energy to the gas for the case without fuel. In addition, without fuel, the kernel grows slower due to the laminar and turbulent burning velocities being zero when no fuel is present.

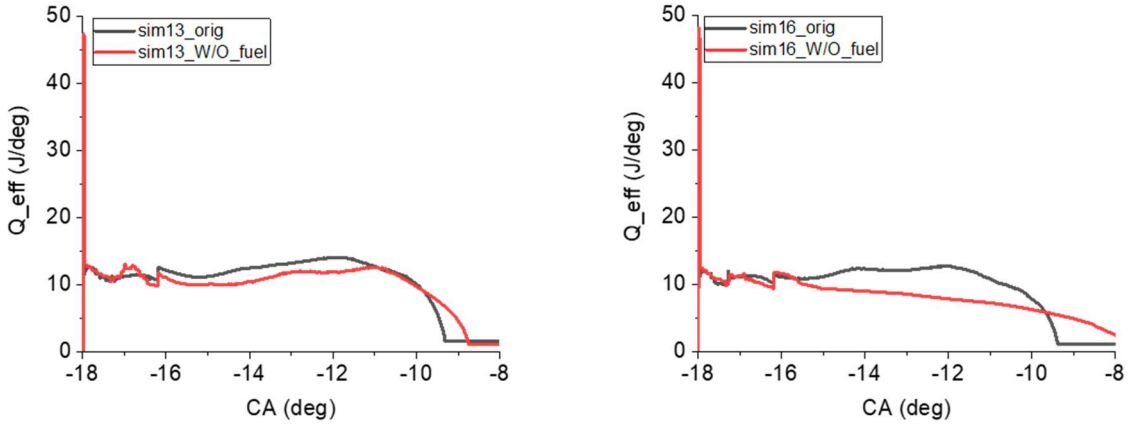

(a) (b)

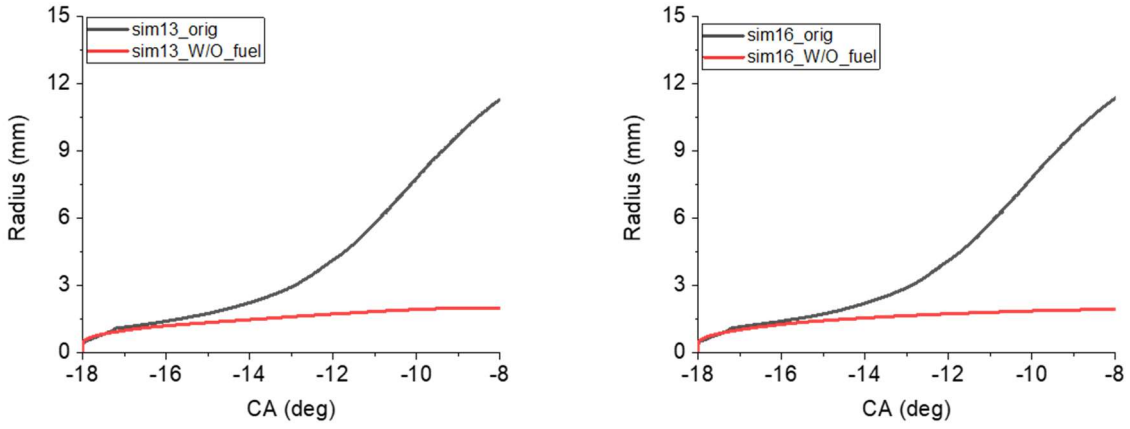

(c) (d)

Figure 5-24 Effect of fuel on energy deposition ((a) effective energy deposition to gas mixture for sim13; (b) effective energy deposition to gas mixture for sim16; (c) kernel radius of sim13; (d) kernel radius of sim16)

5.3 Lean Combustion

The ignition model and combustion model were tested in lean combustion cases to further validate the model. For lean combustion, it was found that the alpha transition function needs to be turned off to sustain the combustion. This will need to be explored further in future studies. The goal for the lean combustion study is to validate if the current model could be applied not just to stoichiometric combustion but also to lean combustion. Seven random cycles are chosen where the initial conditions, such as temperature and flow fields, are borrowed from the stoichiometric cases while the uniform species mass fractions corresponding to the equivalence ratio 0.705 and uniform pressure are applied. The pressure and heat release rate are shown in Figure 5-25.

In Figure 5-25, one can see the pressure traces and the HRR comparison between the experiments and the lean combustion. The three dashed lines “Upper Bound,” “Lower Bound,” and “Averaged,” represent the highest cycle, lowest cycle, and ensemble averaged cycles in the experiments. In general, the seven simulation cycles a reasonable range of variation compared to the experiments. However, since the initial conditions were artificially constructed from the

stoichiometric cases, the pressure and heat release show significant differences from the experimental results. Better initial conditions and probably additional model calibration will be needed for future studies on lean combustion.

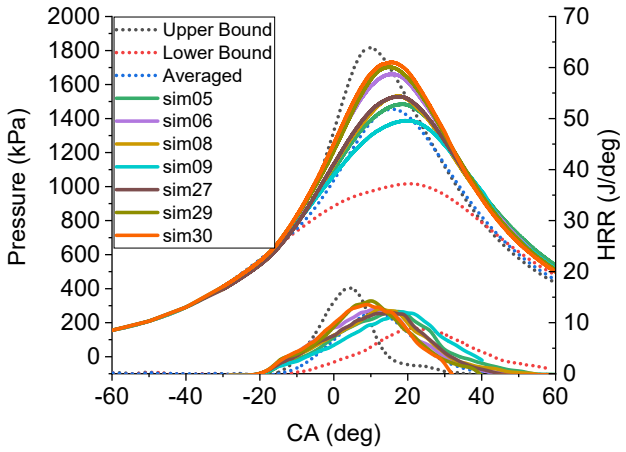

Figure 5-25 Pressure traces and HRR comparison between experiments and lean combustion (seven random cycles are chosen for simulations)

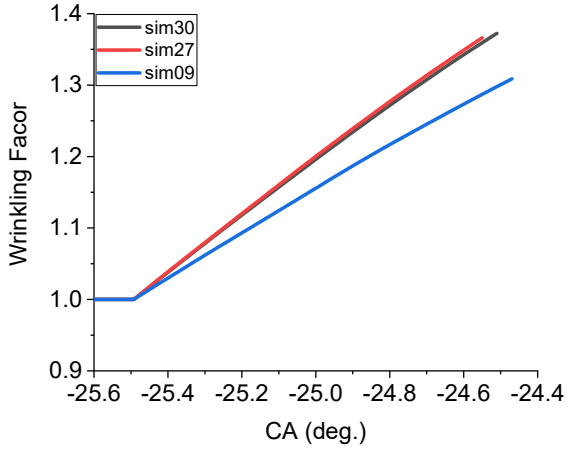

Figure 5-26 Wrinkling factors for high, medium, and low cycles (high: sim30; medium: sim27; low: sim09)

Among those seven simulation cycles, the high (sim30), medium (sim27), and low (sim09) cases are chosen based on their CA10 values to investigate the wrinkling factor and flow fields. Figure 5-26 shows the wrinkling factors for high, medium, and low cycles. The high and medium

cycles display a larger wrinkling factor values than that of low cycle, which accelerates the kernel growth. There is only a slight difference for the wrinkling factor between the high and the medium cycles.

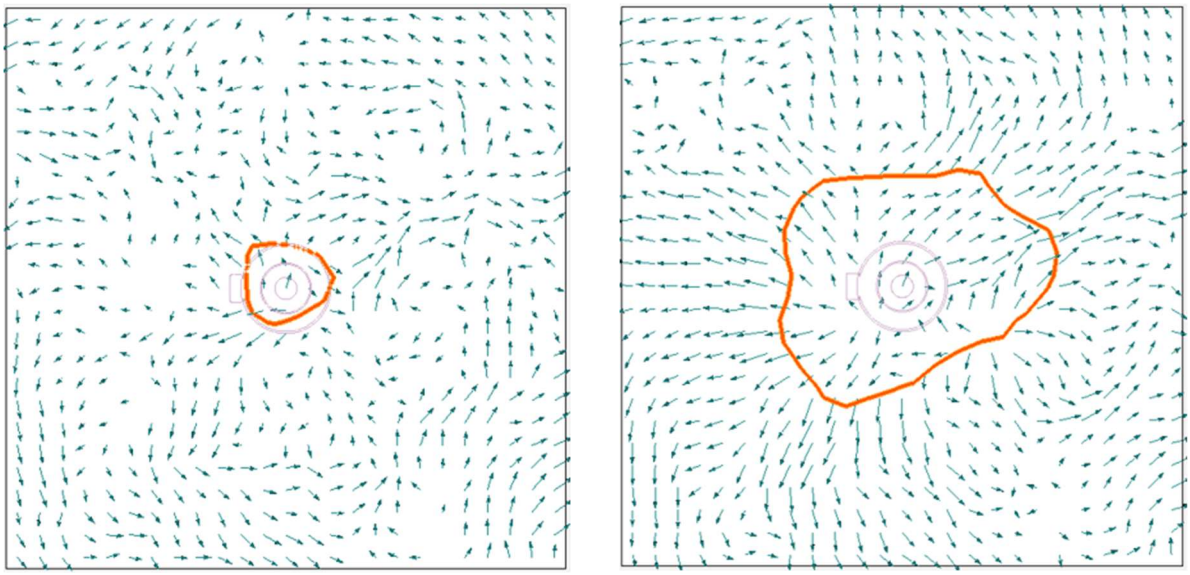

CA = 340 CA = 346

(a) High (sim30)

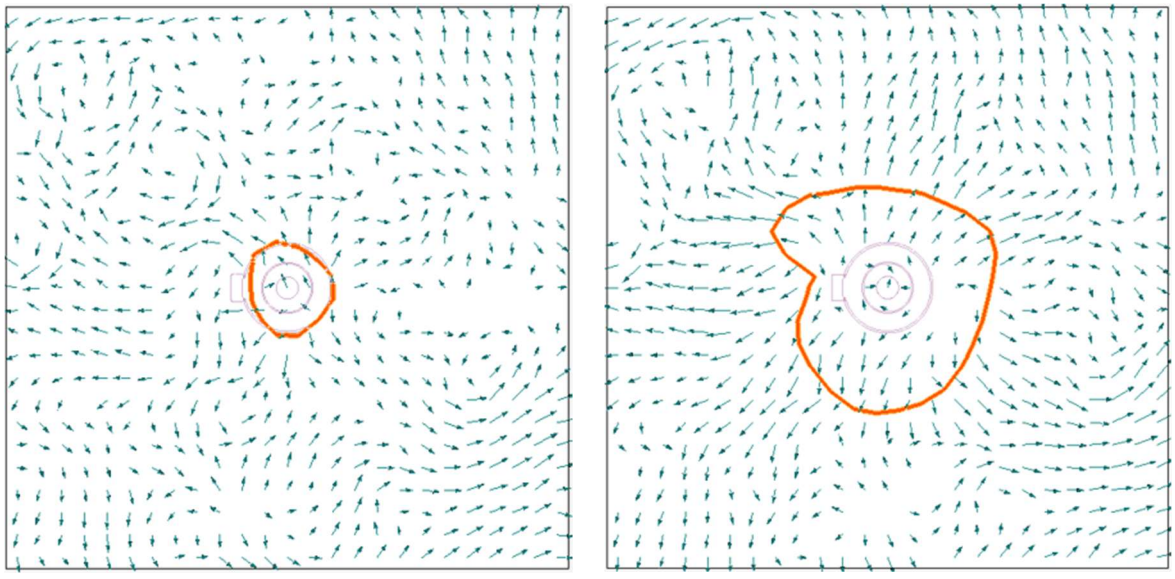

CA = 340 CA = 346

(b) Medium (sim27)

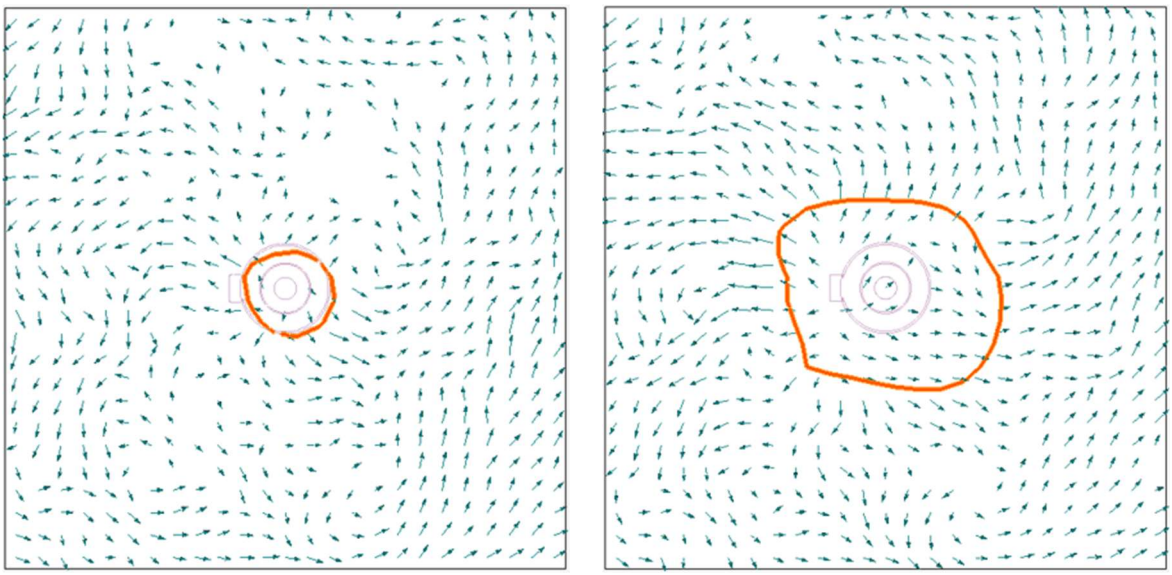

CA = 340 CA = 346

(c) Low (sim09)

Figure 5-27 Velocity fields and $G = 0$ flame front (red curve) of sim05, sim29, and sim09 at CA = 348 and CA = 354 for lean combustion ((a) sim30; (b) sim27; (c) sim09)

As mentioned in stoichiometric combustion, velocity exerts a significant effect on combustion. Thus, the relationship of the flame surface ($G = 0$ isosurface) and the flow fields at an early crank angle is also displayed. Figure 5-27 illustrates the flow fields and $G = 0$ flame front (red curve) of sim30, sim27, and sim09 at CA = 340 and CA = 346 corresponding to 5.5 crank angles and 11.5 crank angles after the start of ignition. The figures are the cut plan passing the ignition location from the top view with each side 60 mm and the spark plug located at the center of the plot.

In Figure 5-27, only the velocities with a magnitude between 1.1 m/s to 65 m/s are displayed, which is consistent with the experiments [119]. As indicated in Figure 5-27, the flow field at CA = 340 shows a clear vortex near the spark plug and the top right region for the high case (sim30), while the flow field for low case (sim09) is weaker on the top of Figure 5-27 (c) at CA = 340. Moreover, it can be seen from Figure 5-27 (a) that even though the $G = 0$ flame front (red curve) is relatively circular at CA = 340, its shape becomes non-symmetric at CA = 346 due to the vortex

near the spark plug at CA = 340. On the other hand, for the low case (sim09), the velocity field is weaker at both CA = 340 and CA = 346 based on the vector arrow lengths. Finally, the velocity fields propagate outward due to the dilatation effect of the flame growth and propagation at CA = 346.

Chapter 6 Summary, Conclusion and Future Work

6.1 Summary and Conclusions

The contributions of this thesis can be divided into four parts. First, in Chapter 3 the LES version ignition model, WSSIM, was developed by accounting for the effect of turbulence on wrinkling and stretching the flame surface. Second, an innovative swept-volume algorithm was implemented and combined with the WSSIM to simulate the ignition and combustion processes in premixed propane/air mixtures. Previous studies have not used the swept-volume algorithm for premixed combustion to investigate the cycle to cycle variations. This work also demonstrates the coupling of the swept-volume algorithm and the G-Equation combustion model for the application in TCC3 engine. Third, a reinitialization scheme was implemented and extended to hexahedral cells, non-hexahedral cells, and parallel computation. Fourth, the models were validated for both stoichiometric combustion and lean combustion. All models were implemented in the open source software OpenFOAM-5.0. This section provides a summary and review of conclusions about the implemented sub-models.

Ignition Model Development

To simulate the ignition process and further investigate the CCV phenomena, an LES version ignition model, WSSIM, was developed by taking the effect of turbulence on wrinkling and stretching the kernel surface into account. Basically, the WSSIM includes four parts, namely the electric circuit model, the plasma channel model, the kernel growth model, and the restrike model. In the electric circuit sub-model, the secondary circuit is simulated to calculate how much electric energy is provided for the spark plug. In the kernel growth sub-model, the calculation of the flame propagation speed for the ignition kernel is divided into two phases: phase (a) and phase (b). Phase (a) is a Lagrangian process, in which the kernel radius is less than the transition radius and the

wrinkling factor controls how the flame speed changes. Phase (b) is an Eulerian process where the kernel radius exceeds the transition radius and the alpha transition function regulates the flame propagation speed. In addition, the G-Equation is turned on in phase (b). In the plasma model, the arc phase and glow phase are simulated and the plasma velocity calculation is based on whether the temperature inside the plasma channel is three times that of the corresponding adiabatic temperature. In the restrike sub-model, if the ignition kernel is displaced more than 5 mm for the initial location during the ignition process, a restrike event is assumed to take place. Therefore, a new spherical kernel is initialized at the spark ignition location, and the old kernel is no longer traced.

The ignition model was applied to a constant volume charged with a mixture of propane and air, and the predicted kernel size from simulations were successfully compared with the available experimental data [113].

G-Equation Combustion Model and Swept-Volume Algorithm

Level set methods have been widely used for capturing interface evolution, especially when the interface undergoes extreme topological changes such as merging or pinching off. In the current study, the G-Equation is used to track the flame surface during the combustion process where the flame front is set at $G = 0$. The G-Equation for both the corrugated and thin reaction flamelet regimes were implemented in OpenFOAM, and its RANS and LES version were given.

To calculate the species reaction rate and heat release rate more accurately, a new innovative swept-volume approach based on precise sub-volume calculations was implemented in OpenFOAM. The basic idea behind the swept-volume algorithm is to find the intersection points between the flame fronts and the mesh cell edges to determine the burnt sub-volume, triangulate the burnt sub-volume, and finally to apply the Gaussian divergence theorem [1] to calculate the

burnt sub-volume. Moreover, the swept-volume algorithm was extended to hexahedral, prism, pyramid and tetrahedral meshes with the number of different intersection cases of 256, 64, 32, and 16, respectively.

The swept-volume algorithm was validated by a 3D ellipsoid, and two intersected spheres with errors less than 0.3% when the mesh resolution is 1 mm. Beyond this, the swept-volume algorithm was coupled with G-Equation and showed a more accurate radius prediction than that of GM model radius prediction when compared with experimental data [111]. Both the GM combustion model and the swept-volume combustion model were applied to the TCC3 engine case, and the swept-volume combustion model gave a more accurate pressure trace prediction when compared to experimental measurements.

Reinitialization Scheme Implementation

The property $|\nabla G| = 1$ needs to be maintained during the simulation in order to find the correct location of the $G = 0$ isosurface. Therefore, a reinitialization scheme was used for the reconstruction of the signed distance function in the context of level set methods.

In this research, the method put forward in [3] was improved by extending to non-uniform and non-orthogonal for engine hexahedral mesh cases, and further extended to parallel computing by accurately determining the neighbor cells for each mesh cell. The reinitialization was generalized to be more universal to all mesh types. The new scheme was named “efficient direct reinitialization” and was implemented in OpenFOAM.

The reinitialization scheme was validated by both serial computation and parallel computation. The reinitialization on the hexahedral mesh was first validated followed by the non-hexahedral mesh. The validation was also performed for both 2D and 3D meshes.

Application to TCC3 Engine

The combination of the ignition model and the swept-volume based combustion model was applied to the TCC3 engine to investigate the CCV phenomena. Three topics were investigated: first, the relationship between mesh resolution and flame surface capture was studied; then the model application to stoichiometric propane/air combustion was studied; finally, the application of the model to lean combustion was presented.

The conclusion achieved from the relationship between mesh resolution and flame surface capture was that the mesh size should be less than the inverse curvature of the initial kernel size in order to capture the kernel front accurately.

To investigate the CCV phenomena in engines, the 30 TCC3 engine simulation cycles were performed. The pressure traces of these 30 cycles shows CCV phenomena, and the averaged pressure trace from the simulations matched the experimental average pressure trace fairly well indicating good accuracy from the current model. Meanwhile, the magnitudes of the current and voltage from simulation cycles displayed similar shape and magnitude as the experimental values.

Sensitivity tests were implemented by choosing three representative cases: high, medium, low according to their CA10 values. It was found that changing the equivalence ratio ϕ had slighter effect on combustion (CA10, CA50, and CA90) while changing velocity fields U had the most significant effect on combustion. In addition, the effect of transition radius was also investigated. The results showed that changing the transition radius from 1 mm to 2 mm results in a higher and advanced pressure trace and heat release rate, while changing the transition radius from 2 mm to 3 mm did not show as much effect on pressure traces and heat release rate.

For the lean combustion, the pressure trace, wrinkling factor, and velocity fields are analyzed. Again, the pressure traces show CCV phenomena. Investigation of the velocity fields show a vortex near the spark plug region at early crank angles for the faster combustion cases.

6.2 Recommendations for Future Work

Based on the work in this study, some research topics are suggested for future work.

1. More accurate laminar and turbulent flame speed formulas are needed since they are fundamental in the turbulent flame combustion simulations. In the engine environment where temperature and pressure are high, the flammability might be different from that measured at room temperature and atmospheric pressure. It is desired to formulate the laminar and turbulent burning velocity that are accurately sensitive to the surroundings such as temperature and residual gas.
2. It is recommended to further investigate the role that turbulence plays on wrinkling the flame surface. In this way, this could also give some recommendations for the transition radius setting in the combustion.
3. When applying the models to lean combustion, the alpha transition function needed to be turned off. Thus, for the future work, it is expected to find some evidence to guide when to turn on the alpha transition function and when to turn it off. It will be best if a formula between the alpha transition function and equivalence ratio could be formed.

Appendix A Chemical Equilibrium Solver Test

To examine if the CEQ from Cantera works well in OpenFOAM, one test case from the website [120] was implemented. The initial temperature and pressure were 1500 K and 202650 Pa, respectively. The initial mixture was with 1 mole O_2, 2 mole H_2 and 1 mole Ar. The case was tested under constant temperature and constant pressure given above. The figure shows the state of chemical equilibrium output comparisons under above conditions from Cantera and OpenFOAM. It is apparent that output parameters under equilibrium condition such as temperature, pressure, density, mass fraction of each species, etc. are exactly the same for both Cantera and OpenFOAM, which indicates the success of coupling C++ version CEQ (Cantera) with OpenFOAM.

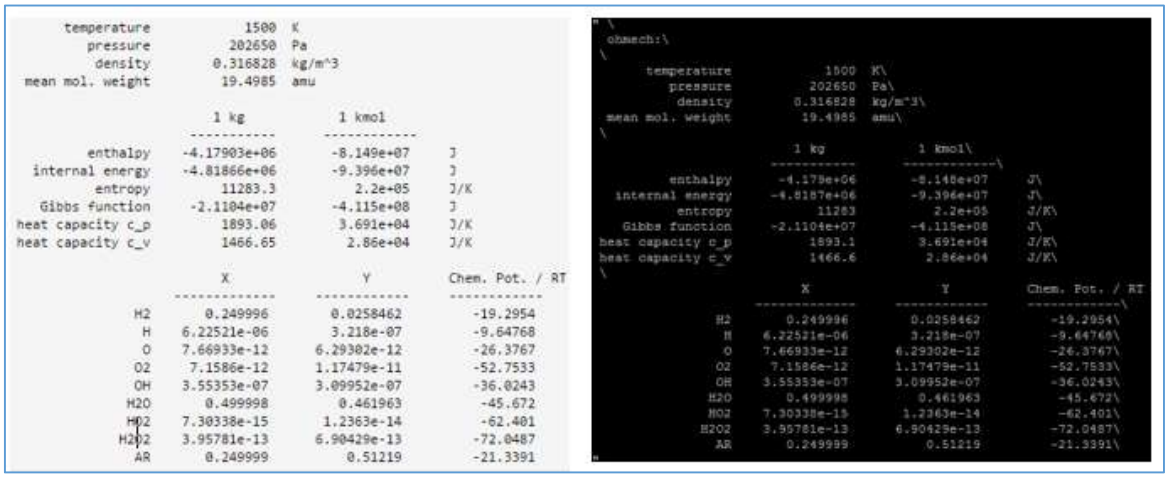

temperature	1500	K
pressure	202650	Pa
density	0.316828	kg/m^3
mean mol. weight	19.4985	amu

	1 kg	1 kmol	
enthalpy	-4.17903e+06	-8.149e+07	J
internal energy	-4.81866e+06	-9.396e+07	J
entropy	11283.3	2.2e+05	J/K
Gibbs function	-2.1104e+07	-4.115e+08	J
heat capacity c_p	1893.06	3.691e+04	J/K
heat capacity c_v	1466.65	2.86e+04	J/K

	X	Y	Chem. Pot. / RT
H2	0.249996	0.0258462	-19.2954
H	6.22521e-06	3.218e-07	-9.64768
O	7.66933e-12	6.29302e-12	-26.3767
O2	7.1586e-12	1.17479e-11	-52.7533
OH	3.55353e-07	3.09952e-07	-36.0243
H2O	0.499998	0.461963	-45.672
HO2	7.30338e-15	1.2363e-14	-62.401
H2O2	3.95781e-13	6.90429e-13	-72.0487
AR	0.249999	0.51219	-21.3391

(a) Results from Cantera

(b) Results from OpenFOAM

Figure A-1 Comparison of CEQ results from Cantera and OpenFOAM

Appendix B Intersections between flame front and cell edges [1]

The swept-volume algorithm in Chapter 3 was used to improve the calculation of the species reaction rates by calculating the sub-volume more accurately. The sub-volume calculation depends on the mesh shapes and this appendix gives the hexahedra, prisms, pyramids, and tetrahedral.

1. Hexahedra: 256 cases in total

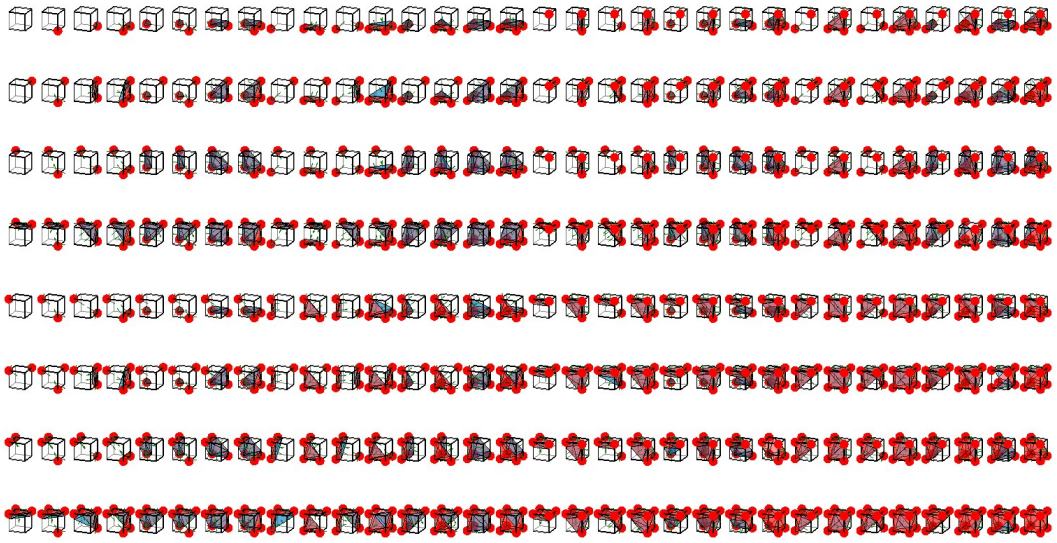

2. Prism: 64 cases in total. The following shows 16 cases where the rest 16 cases the complementary volume.

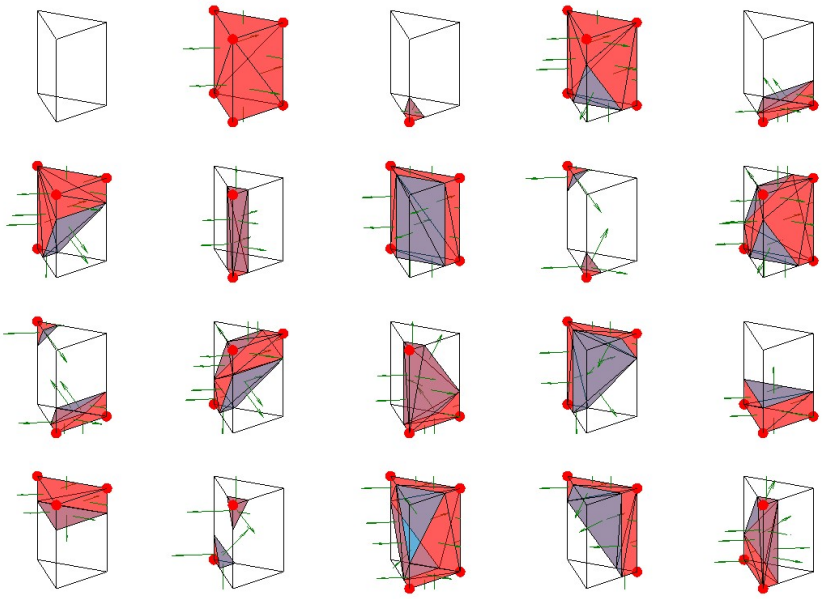

3. Pyramid: 32 cases in total.

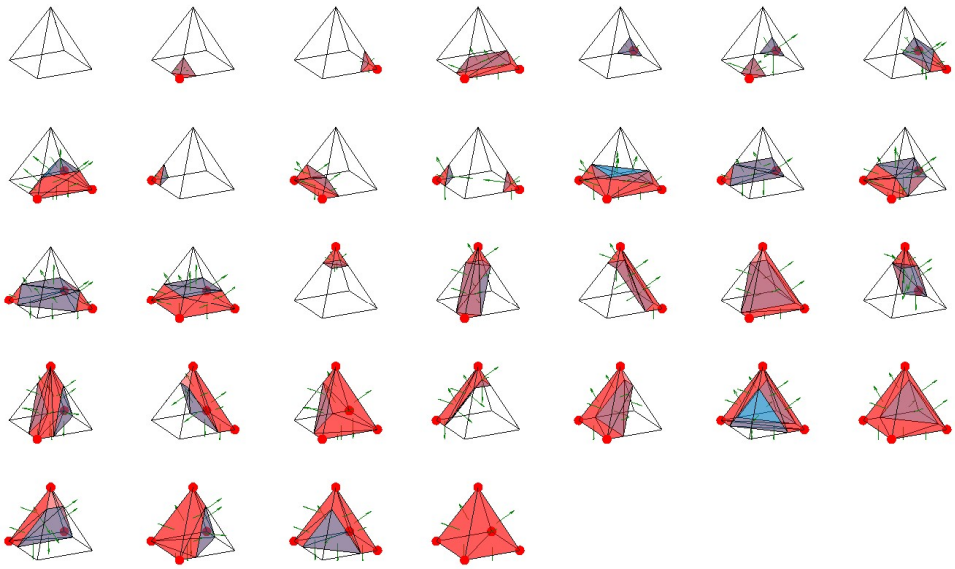

4. Tetrahedral: 16 cases in total.

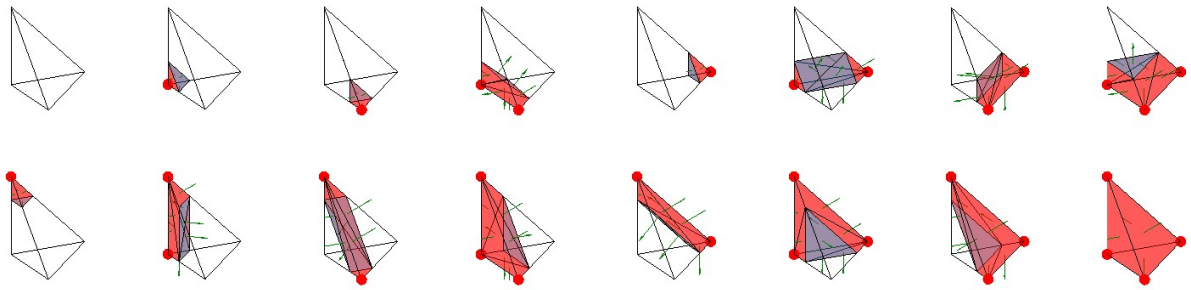

Appendix C Mapping Methods

Figure C-1 shows the engine geometries of CONVERGE and OpenFOAM. The CONVERGE mesh includes the intake and exhaust valves while OpenFOAM mesh does not. To reduce the effect of flow field of port on the whole engine, the crank angle during both intake and exhaust valves are closed, and this was considered to be an appropriate point to do the mapping. From the simulation in CONVERGE, it was recognized that both intake and exhaust valves were closed at 70 CA BTDC. Thus, the flow data mapping process was implemented at this crank angle. The mapping process was executed with the help of Ensight software [118], which uses the nearest cells with linear interpolation to do the mapping. The interpolation method performs the cell mapping by selecting cells from the CONVERGE mesh that have the smallest distance to the cell-centered coordinates to the reference OpenFOAM mesh. The cell properties of these selected CONVERGE cells are then reassigned to OpenFOAM using the nearest neighbor values.

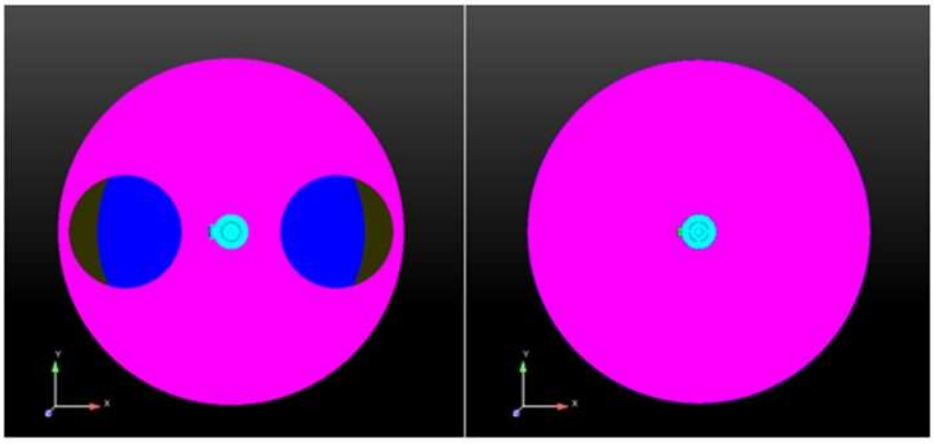

(a) Converge geometry (b) OpenFOAM geometry

Figure C-1 Engine geometry of CONVERGE and OpenFOAM

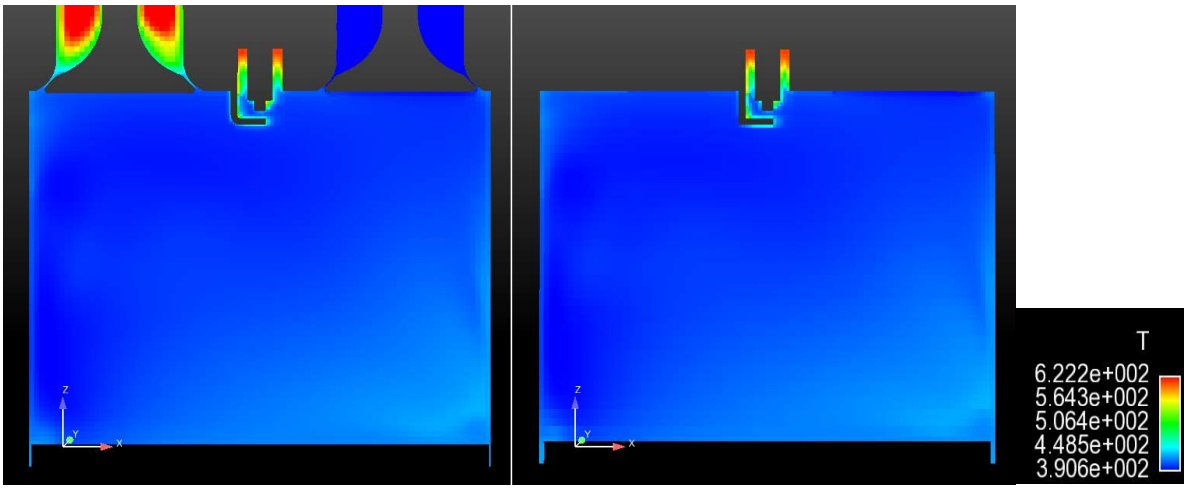

(a) Converge geometry (b) OpenFOAM geometry

Figure C-2 Temperature comparison between CONVERGE and OpenFOAM

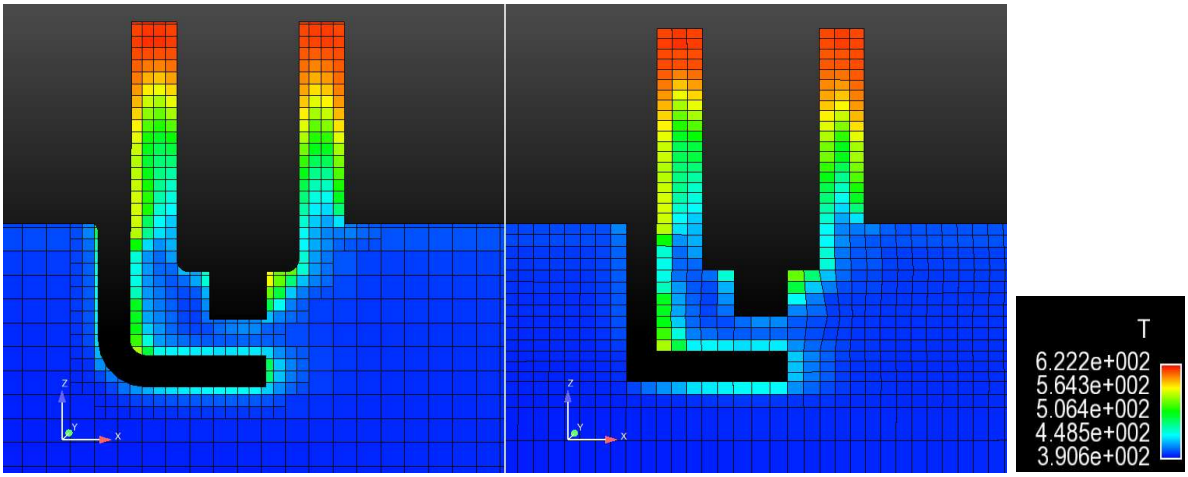

(a) Converge geometry (b) OpenFOAM geometry

Figure C-3 Temperature comparison of amplified spark plug regions between CONVERGE and OpenFOAM

Figure C-2 (a) shows the original CONVERGE flow data and Figure C-2 (b) shows the mapped temperature data based on EnSight. In general, mapping result is consistent from CONVERGE to OpenFOAM, with higher temperatures on the spark plug and lower temperatures at the right bottom corner. Figure 3 shows the amplified spark plug region for both engine

geometries. As displayed in the plot, the mapped temperature result is consistent with the original data from CONVERGE. The local difference is due to mesh resolution.

To gain more insight to check if the mapped temperature is accurate, temperature data on two lines (yellow and green) of the same location cross planes of CONVERGE and OpenFOAM geometries were extracted and compared, as seen in Figure C-4. The top left picture is the CONVERGE cross plane and the left bottom picture is the OpenFOAM cross plane. The top right plot displays a comparison of temperature between the original CONVERGE temperature data and the mapped temperature in OpenFOAM on the yellow line. The bottom right plot displays a comparison of temperature between the original CONVERGE temperature data and the mapped temperature in OpenFOAM on the green line. The mapped temperature in the OpenFOAM mesh is extremely consistent with the original temperature data from CONVERGE. This finding lays a solid foundation for research testing the TCC3 engine simulation.

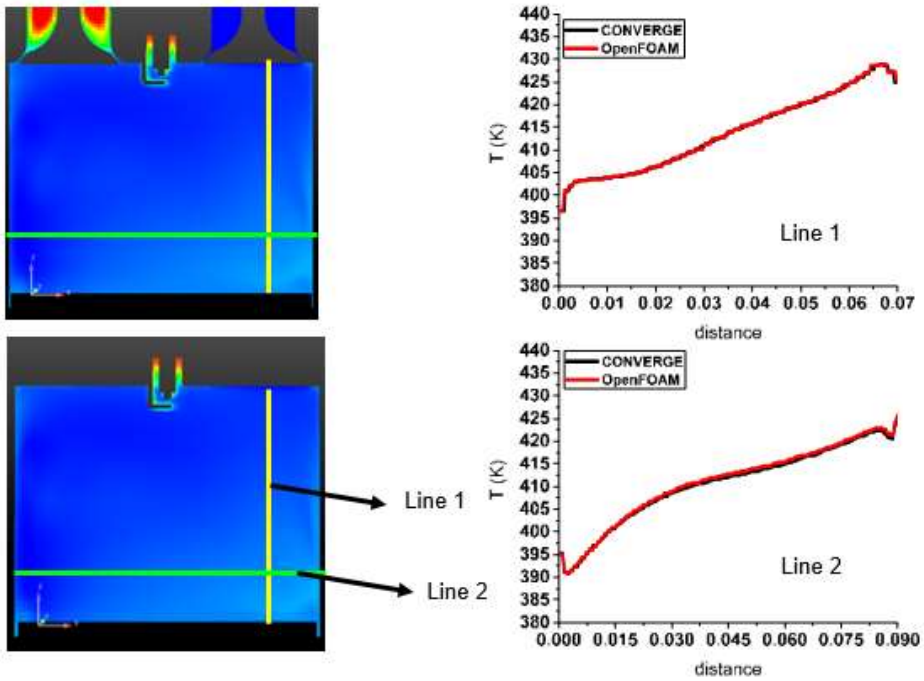

Figure C-4 Extracted temperature comparison on two lines between original CONVERGE data and mapped data in OpenFOAM

References

[1] F. Perini *et al.*, “An efficient level-set flame propagation model for hybrid unstructured grids using the G-equation,” *SAE Int. J. Engines*, vol. 9, no. 3, pp. 1409–1424, 2016.

[2] W. C. Reynolds, “The element potential method for chemical equilibrium analysis: Implementation in the interactive program STANJAN, version 3,” *Tech. Rept.*, 1986.

[3] G. Russo and P. Smereka, “A remark on computing distance functions,” *J. Comput. Phys.*, vol. 163, no. 1, pp. 51–67, 2000.

[4] TCC-III CFD Input Dataset, for dx.doi.org/10.1177/1468087417720558.

[5] H. Chen, M. Xu, and D. L. S. Hung, “Analyzing in-cylinder flow evolution and variations in a spark-ignition direct-injection engine using phase-invariant proper orthogonal decomposition technique,” 2014.

[6] B. Johansson, “Cycle to cycle variations in SI engines-the effects of fluid flow and gas composition in the vicinity of the spark plug on early combustion,” *SAE transactions*, 1996. .

[7] P. G. Aleiferis, Y. Hardalupas, A. Taylor, K. Ishii, and Y. Urata, “Flame chemiluminescence studies of cyclic combustion variations and air-to-fuel ratio of the reacting mixture in a lean-burn stratified-charge spark-ignition engine,” *Combust. Flame*, vol. 136, no. 1–2, pp. 72–90, 2004.

[8] J. B. Heywood and others, “Internal combustion engine fundamentals,” 1988.

[9] O. Vermorel, S. Richard, O. Colin, C. Angelberger, A. Benkenida, and D. Veynante, “Towards the understanding of cyclic variability in a spark ignited engine using multi-cycle LES,” *Combust. Flame*, vol. 156, no. 8, pp. 1525–1541, 2009.

[10] C. Pera, S. Chevillard, and J. Reveillon, “Effects of residual burnt gas heterogeneity on early flame propagation and on cyclic variability in spark-ignited engines,” *Combust. Flame*, vol.

160, no. 6, pp. 1020–1032, 2013.

[11] V. I. Golovitchev, N. Nordin, R. Jarnicki, and J. Chomiak, “3-D diesel spray simulations using a new detailed chemistry turbulent combustion model,” 2000.

[12] E. Pomraning, K. Richards, and P. K. Senecal, “Modeling turbulent combustion using a RANS model, detailed chemistry, and adaptive mesh refinement,” 2014.

[13] R. Herweg, P. Begleris, A. Zettlitz, and G. F. W. Ziegler, “Flow field effects on flame kernel formation in a spark-ignition engine,” *SAE Trans.*, pp. 826–846, 1988.

[14] K. Yun, S. Lee, and N. Sung, “A study of the propagation of turbulent premixed flame using the flame surface density model in a constant volume combustion chamber,” *KSME Int. J.*, vol. 16, no. 4, pp. 564–571, 2002.

[15] G. D’Errico, T. Lucchini, S. Merola, and C. Tornatore, “Application of a thermodynamic model with a complex chemistry to a cycle resolved knock prediction on a spark ignition optical engine,” *Int. J. Automot. Technol.*, vol. 13, no. 3, pp. 389–399, 2012.

[16] Y. S. Shekhawat, “Large-eddy simulations of motored flow and combustion in a homogeneous-charge spark-ignition engine,” 2016.

[17] R. N. Dahms, M. C. Drake, T. D. Fansler, T.-W. Kuo, and N. Peters, “Understanding ignition processes in spray-guided gasoline engines using high-speed imaging and the extended spark-ignition model SparkCIMM. Part A: Spark channel processes and the turbulent flame front propagation,” *Combust. Flame*, vol. 158, no. 11, pp. 2229–2244, 2011.

[18] R. N. Dahms, M. C. Drake, T. D. Fansler, T.-W. Kuo, and N. Peters, “Understanding ignition processes in spray-guided gasoline engines using high-speed imaging and the extended spark-ignition model SparkCIMM. Part B: Importance of molecular fuel properties in earlyflame front propagation,” *Combust. Flame*, vol. 158, no. 11, pp. 2245–

2260, Nov. 2011.

[19] R. Herweg and R. R. Maly, “A fundamental model for flame kernel formation in SI engines,” *SAE Trans.*, pp. 1947–1976, 1992.

[20] P. Boudier, S. Henriot, T. Poinsot, and T. Baritaud, “A model for turbulent flame ignition and propagation in spark ignition engines,” in *Symposium (International) on Combustion*, 1992, vol. 24, no. 1, pp. 503–510.

[21] K. N. C. Bray and J. B. Moss, “A unified statistical model of the premixed turbulent flame,” *Acta Astronaut.*, vol. 4, no. 3–4, pp. 291–319, 1977.

[22] Z. Tan and R. D. Reitz, “Modeling ignition and combustion in spark-ignition engines using a level set method,” 2003.

[23] R. N. Dahms, M. C. Drake, R. O. Grover Jr, A. S. Solomon, and T. D. Fansler, “Detailed simulations of stratified ignition and combustion processes in a spray-guided gasoline engine using the SparkCIMM/G-equation modeling framework,” *SAE Int. J. Engines*, vol. 5, no. 2, pp. 141–161, 2012.

[24] T. Lucchini *et al.*, “A comprehensive model to predict the initial stage of combustion in SI engines,” 2013.

[25] N. Peters, “Turbulent Combustion. Cambridge University Press, 2000.”

[26] C. K. Law, “A compilation of recent experimental data of premixed laminar flames,” *Reduc. Kinet. Mech. Appl. Combust. Syst. Lect. Notes Phys.*, vol. 15, pp. 19–30, 1993.

[27] H. Pitsch and H. Steiner, “Scalar mixing and dissipation rate in large-eddy simulations of non-premixed turbulent combustion,” *Proc. Combust. Inst.*, vol. 28, no. 1, pp. 41–49, 2000.

[28] N. Peters, “Laminar diffusion flamelet models in non-premixed turbulent combustion,” *Prog. energy Combust. Sci.*, vol. 10, no. 3, pp. 319–339, 1984.

[29] J. M. Donbar, J. F. Driscoll, and C. D. Carter, “Reaction zone structure in turbulent nonpremixed jet flames—from CH-OH PLIF images,” *Combust. Flame*, vol. 122, no. 1–2, pp. 1–19, 2000.

[30] R. S. Barlow and J.-Y. Chen, “On transient flamelets and their relationship to turbulent methane-air jet flames,” in *Symposium (International) on Combustion*, 1992, vol. 24, no. 1, pp. 231–237.

[31] H. Jasak, A. Jemcov, Z. Tukovic, and others, “OpenFOAM: A C++ library for complex physics simulations,” in *International workshop on coupled methods in numerical dynamics*, 2007, vol. 1000, pp. 1–20.

[32] E. Sher, J. Ben-Ya’ish, and T. Kravchik, “On the birth of spark channels,” *Combust. Flame*, vol. 89, no. 2, pp. 186–194, 1992.

[33] D. Go, “Gaseous Ionization and Ion Transport: An Introduction to Gas Discharges,” *Dep. Aerosp. Mech. Eng. Univ. Notre Dame,* vol. 46556, pp. 1–45, 2012.

[34] K. P, *Ignition Modeling for Spark Ignition Engines, Master Thesis*. University of Wisconsin--Madison, 2016.

[35] E. Nasser, *Fundamentals of gaseous ionization and plasma electronics*. Wiley-Interscience, 1971.

[36] Wikipedia contributors, “Streamer discharge -Wikipedia, The Free Encyclopedia.” 2018.

[37] S. Refael and E. Sher, “A theoretical study of the ignition of a reactive medium by means of an electrical discharge,” *Combust. Flame*, vol. 59, no. 1, pp. 17–30, 1985.

[38] M. Kono, K. Niu, T. Tsukamoto, and Y. Ujiie, “Mechanism of flame kernel formation produced by short duration sparks,” in *Symposium (International) on Combustion*, 1989, vol. 22, no. 1, pp. 1643–1649.

[39] G. Stiesch, *Modeling engine spray and combustion processes*. Springer Science & Business Media, 2013.

[40] N. Jeanvoine, R. Jonsson, and F. Muecklich, "Investigation of the arc and glow phase fractions of ignition discharges in air and nitrogen for Ag, Pt, Cu and Ni electrodes," *JCPIG. Prague*, pp. 15–20, 2007.

[41] E. Hantzsche, "Mysteries of the arc cathode spot: A retrospective glance," *IEEE Trans. plasma Sci.*, vol. 31, no. 5, pp. 799–808, 2003.

[42] Wikipedia contributors, "Electric discharge in gases -Wikipedia, The Free Encyclopedia." 2018.

[43] L. Fan, *Multi-dimensional Modeling of Mixing and Combustion of Direct Injection Spark Ignition Engines*. University of Wisconsin--Madison, 2000.

[44] X. Yang, T. Ohashi, T. Takabayashi, S. Kubota, H. Katsuyama, and Y. Urata, "Ignition and Combustion Modeling with G-Equation in Spark Ignition Engines," in *The 13th International Pacific Conference on Automotive Engineering*, 2006.

[45] L. Fan and R. D. Reitz, "Multi-dimensional modeling of mixing and combustion of a two-stroke direct-injection spark ignition engine," 2001.

[46] Z. Tan, "Multi-dimensional modeling of ignition and combustion in premixed and DIS/CI (direct injection spark/compression ignition) engines.," 2004.

[47] J. M. Duclos and O. Colin, "Arc and Kernel Tracking Ignition Model for 3D Spark Ignition Engine Calculations, 5th Int," in *Symp. on Diagnostics and Modeling of Combustion in Internal Combustion Engines, COMODIA*, 2001.

[48] S. Richard, O. Colin, O. Vermorel, A. Benkenida, C. Angelberger, and D. Veynante, "Towards large eddy simulation of combustion in spark ignition engines," *Proc. Combust.*

Inst., vol. 31, no. 2, pp. 3059–3066, 2007.

[49] O. Colin and K. Truffin, “A spark ignition model for large eddy simulation based on an FSD transport equation (ISSIM-LES),” *Proc. Combust. Inst.*, vol. 33, no. 2, pp. 3097–3104, 2011.

[50] K. Seshadri and N. Peters, “The inner structure of methane-air flames,” *Combust. Flame*, vol. 81, no. 2, pp. 96–118, 1990.

[51] N. Peters and F. A. Williams, “The asymptotic structure of stoichiometric methane□ air flames,” *Combust. Flame*, vol. 68, no. 2, pp. 185–207, 1987.

[52] J. Jarosinski, “Thickness of laminar flames,” *Combust. Flame;(United States)*, vol. 56, 1984.

[53] H. Wenzel, “Turbulent premixed combustion in the laminar amelet and the thin reaction zone regime,” 1997.

[54] Y. Chen and K. H. Luo, “Turbulent premixed hydrogen flames at high Karlovitz number: A DNS study.”

[55] N. Peters, “Fifteen lectures on laminar and turbulent combustion,” *Ercoftac Summer Sch.*, vol. 1428, 1992.

[56] J. Abraham, F. V Bracco, and R. D. Reitz, “Comparisons of computed and measured premixed charge engine combustion,” *Combust. Flame*, vol. 60, no. 3, pp. 309–322, 1985.

[57] D. B. Spalding, “Development of the eddy-break-up model of turbulent combustion,” in *Symposium (International) on Combustion*, 1977, vol. 16, no. 1, pp. 1657–1663.

[58] Z. Tan and R. D. Reitz, “An ignition and combustion model based on the level-set method for spark ignition engine multidimensional modeling,” *Combust. Flame*, vol. 145, no. 1–2, pp. 1–15, 2006.

[59] D. B. Spalding, “Mixing and chemical reaction in steady confined turbulent flames,” in

Symposium (International) on Combustion, 1971, vol. 13, no. 1, pp. 649–657.

[60] B. F. Magnussen and B. H. Hjertager, "On mathematical modeling of turbulent combustion with special emphasis on soot formation and combustion," in *Symposium (international) on Combustion*, 1977, vol. 16, no. 1, pp. 719–729.

[61] T. Poinsot and D. Veynante, *Theoretical and numerical combustion*. RT Edwards, Inc., 2005.

[62] N. Dinler and N. Yucel, "Numerical simulation of flow and combustion in an axisymmetric internal combustion engine," in *Proceedings of World Academy of Science, Engineering and Technology*, 2007, vol. 22.

[63] R. Mobasheri, Y. Fotrosy, and S. Jalalifar, "Modeling of a spark ignition engine combustion: A computational and experimental study of combustion process effects on NOX emissions," *Asian J. Appl. Sci*, vol. 2, pp. 318–330, 2009.

[64] D. Zhang and S. H. Frankel, "A numerical study of natural gas combustion in a lean burn engine," *Fuel*, vol. 77, no. 12, pp. 1339–1347, 1998.

[65] B. F. Magnussen, "The Eddy Dissipation Concept—A Bridge Between Science and Technology," in *ECCOMAS thematic conference on computational combustion*, 2005, pp. 21–24.

[66] A. Fluent and others, "Theory guide," *Ansys Inc*, 2015.

[67] L. Fan and R. D. Reitz, "Development of an ignition and combustion model for spark-ignition engines," *SAE Trans.*, pp. 1977–1989, 2000.

[68] P. Eckert, S.-C. Kong, and R. D. Reitz, "Modeling autoignition and engine knock under spark ignition conditions," 2003.

[69] L. Liang, *Multidimensional modeling of combustion and knock in spark-ignition engines*

with detailed chemical kinetics. ProQuest, 2006.

[70] C. M. Müller, H. Breitbach, and N. Peters, "Partially premixed turbulent flame propagation in jet flames," in *Symposium (International) on Combustion*, 1994, vol. 25, no. 1, pp. 1099–1106.

[71] N. Peters, "Four lectures on turbulent combustion," *ERCOFTAC Summer Sch.*, 1997.

[72] W. Malalasekera and C. P. Ranasinghe, "Simulation of premixed combustion and near wall flame quenching in spark ignition engines with an improved formulation of the bray-moss-libby model," 2012.

[73] G. M. Abu-Orf and R. S. Cant, "A turbulent reaction rate model for premixed turbulent combustion in spark-ignition engines," *Combust. Flame*, vol. 122, no. 3, pp. 233–252, 2000.

[74] M. P. Musculus and C. J. Rutland, "Coherent Flamelet Mlodeling of Diesel Engine Combustion," *Combust. Sci. Technol.*, vol. 104, no. 4–6, pp. 295–337, 1995.

[75] A. Gurupatham and A. Teraji, "A study of rich flame propagation in gasoline SI engine based on 3-D numerical simulations," 2011.

[76] A. Teraji, T. Tsuda, T. Noda, M. Kubo, and T. Itoh, "Development of a novel flame propagation model (UCFM: universal coherent flamelet model) for SI engines and its application to knocking prediction," 2005.

[77] J. Wen, A. Heidari, S. Ferraris, and V. Tam, "Predicting flame acceleration using a coherent flame model," 2011.

[78] T. Lucchini, L. Cornolti, G. Montenegro, and G. D'Errico, "DEVELOPMENT OF ADVANCED MODELS FOR COMBUSTION SIMULATIONS IN IC ENGINES."

[79] O. Colin and A. Benkenida, "The 3-zones extended coherent flame model (ECFM3Z) for computing premixed/diffusion combustion," *Oil Gas Sci. Technol.*, vol. 59, no. 6, pp. 593–

609, 2004.

[80] L. Liang and R. D. Reitz, “Spark ignition engine combustion modeling using a level set method with detailed chemistry,” 2006.

[81] D. Enright, R. Fedkiw, J. Ferziger, and I. Mitchell, “A hybrid particle level set method for improved interface capturing,” *J. Comput. Phys.*, vol. 183, no. 1, pp. 83–116, 2002.

[82] N. Peters, “The turbulent burning velocity for large-scale and small-scale turbulence,” *J. Fluid Mech.*, vol. 384, pp. 107–132, 1999.

[83] P. Pelce and P. Clavin, “Influence of hydrodynamics and diffusion upon the stability limits of laminar premixed flames,” *J. Fluid Mech.*, vol. 124, pp. 219–237, 1982.

[84] H. Pitsch, “A G-equation formulation for large-eddy simulation of premixed turbulent combustion,” *Cent. Turbul. Res. Annu. Res. Briefs*, vol. 4, 2002.

[85] N. Peters, P. Terhoeven, J. H. Chen, and T. Echekki, “Statistics of flame displacement speeds from computations of 2-D unsteady methane-air flames,” in *Symposium (International) on Combustion*, 1998, vol. 27, no. 1, pp. 833–839.

[86] J. O. Hirschfelder, C. F. Curtiss, and D. E. Campbell, “The theory of flame propagation. IV,” *J. Phys. Chem.*, vol. 57, no. 4, pp. 403–414, 1953.

[87] D. B. Spalding, “The theory of flame phenomena with a chain reaction,” *Phil. Trans. R. Soc. Lond. A*, vol. 249, no. 957, pp. 1–25, 1956.

[88] U. C. Müller, M. Bollig, and N. Peters, “Approximations for burning velocities and Markstein numbers for lean hydrocarbon and methanol flames,” *Combust. Flame*, vol. 108, no. 3, pp. 349–356, 1997.

[89] Ö. L. Gülder, “Correlations of laminar combustion data for alternative SI engine fuels,” 1984.

[90] M. Metghalchi and J. C. Keck, “Burning velocities of mixtures of air with methanol, isooctane, and indolene at high pressure and temperature,” *Combust. Flame*, vol. 48, pp. 191–210, 1982.

[91] E. Pomraning and C. J. Rutland, “Dynamic one-equation nonviscosity large-eddy simulation model,” *AIAA J.*, vol. 40, no. 4, pp. 689–701, 2002.

[92] M. Chen, M. Herrmann, and N. Peters, “Flamelet modeling of lifted turbulent methane/air and propane/air jet diffusion flames,” *Proc. Combust. Inst.*, vol. 28, no. 1, pp. 167–174, 2000.

[93] Z. Tan, S.-C. Kong, and R. D. Reitz, “Modeling premixed and direct injection SI engine combustion using the G-equation model,” 2003.

[94] S. Yang, “Modeling multi-component fuel evaporation, flame propagation, and chemical kinetics processes for GDI engines.” University of Wisconsin-Madison Madison, Wisconsin, USA, 2010.

[95] M. Cubes, “A high resolution 3d surface construction algorithm/william e,” *Lorensen, Harvey E. Cline--SIG*, vol. 87, p. 76, 1987.

[96] A. Guéziec and R. Hummel, “Exploiting triangulated surface extraction using tetrahedral decomposition,” *IEEE Trans. Vis. Comput. Graph.*, vol. 1, no. 4, pp. 328–342, 1995.

[97] Bourke, Paul. “Polygonising a scalar field. ” 1994.

[98] S. B. Pope, “CEQ: A Fortran library to compute equilibrium compositions using Gibbs function continuation.” Technical report, 2003. http://eccentric. mae. cornell. edu/pope/CEQ, 2003.

[99] S. I. Feldman, “A Fortran to C converter,” in *ACM SIGPLAN Fortran Forum*, 1990, vol. 9, no. 2, pp. 21–22.

[100] D. Goodwin, "Cantera: Object-oriented software for reacting flows," *Calif. Inst. Technol. (Caltech).< http//www. cantera. org>(accessed July, 2007)*, 2005.

[101] D. L. Chopp, "Computing minimal surfaces via level set curvature flow," 1991.

[102] M. Sussman, P. Smereka, and S. Osher, "A level set approach for computing solutions to incompressible two-phase flow," *J. Comput. Phys.*, vol. 114, no. 1, pp. 146–159, 1994.

[103] M. Sussman and P. Smereka, "Axisymmetric free boundary problems," *J. Fluid Mech.*, vol. 341, pp. 269–294, 1997.

[104] S. Chen, B. Merriman, S. Osher, and P. Smereka, "A simple level set method for solving Stefan problems," *J. Comput. Phys.*, vol. 135, no. 1, pp. 8–29, 1997.

[105] B. Merriman, J. K. Bence, and S. J. Osher, "Motion of multiple junctions: A level set approach," *J. Comput. Phys.*, vol. 112, no. 2, pp. 334–363, 1994.

[106] L. C. Ngo and H. G. Choi, "Efficient direct re-initialization approach of a level set method for unstructured meshes," *Comput. Fluids*, vol. 154, pp. 167–183, 2017.

[107] J. Kim and R. W. Anderson, "Spark anemometry of bulk gas velocity at the plug gap of a firing engine," *SAE Trans.*, pp. 2256–2266, 1995.

[108] P. Schiffmann, "Root causes of cycle-to-cycle combustion variations in spark ignited engines," 2016.

[109] O. Colin, F. Ducros, D. Veynante, and T. Poinsot, "A thickened flame model for large eddy simulations of turbulent premixed combustion," *Phys. fluids*, vol. 12, no. 7, pp. 1843–1863, 2000.

[110] Weisstein, Eric W. "Spherical cap." 2008.

[111] M. Fairweather, M. P. Ormsby, C. G. W. Sheppard, and R. Woolley, "Turbulent burning rates of methane and methane--hydrogen mixtures," *Combust. Flame*, vol. 156, no. 4, pp.

780–790, 2009.

[112] F. N. Egolfopoulos, H. Zhang, and Z. Zhang, “Wall effects on the propagation and extinction of steady, strained, laminar premixed flames,” *Combust. Flame*, vol. 109, no. 1–2, pp. 237–252, 1997.

[113] I. K. Nwagwe *et al.*, “Measurements and large eddy simulations of turbulent premixed flame kernel growth,” *Proc. Combust. Inst.*, vol. 28, no. 1, pp. 59–65, 2000.

[114] S. G. Chumakov and C. J. Rutland, “Dynamic structure subgrid-scale models for large eddy simulation,” *Int. J. Numer. methods fluids*, vol. 47, no. 8–9, pp. 911–923, 2005.

[115] R. Maly and M. Vogel, “Initiation and propagation of flame fronts in lean CH4-air mixtures by the three modes of the ignition spark,” in *Symposium (International) on Combustion*, 1979, vol. 17, no. 1, pp. 821–831.

[116] F. Piscaglia, A. Montorfano, and A. Onorati, “Development of Fully-Automatic Parallel Algorithms for Mesh Handling in the OpenFOAM®-2.2. x Technology,” 2013.

[117] Y. Ra and R. D. Reitz, “A combustion model for multi-component fuels using a physical surrogate group chemistry representation (PSGCR),” *Combust. Flame*, vol. 162, no. 10, pp. 3456–3481, 2015.

[118] C. S. M. EnSight, “CFD Post processing.” .

[119] W. Zeng, S. Keum, T.-W. Kuo, and V. Sick, “Role of large scale flow features on cycle-to-cycle variations of spark-ignited flame-initiation and its transition to turbulent combustion,” *Proc. Combust. Inst.*, 2018.

[120] “A C++ Chemical Equilibrium Program.” Retrived from http://web.mit.edu/2.62/cantera/doc/html/cxx-equildemo.html.